UNIVERSITAT DE BARCELONA

Experiments on perturbed Saffman-Taylor flows

Jordi Ignés i Mullol,

UNIVERSITAT DE BARCELONA

Departament d'Estructura i Constituents de la Matèria

EXPERIMENTS ON PERTURBED SAFFMAN-TAYLOR FLOWS

Experiments en fluxes de Saffman-Taylor modificats

per

Jordi Ignés i Mullol

Memòria de la Tesi presentada per optar al grau de
Doctor en Ciències Físiques.

UNIVERSITAT DE BARCELONA

Programa d'Estructura i Constituents de la Matèria

Bienni: 1992-94

EXPERIMENTS ON PERTURBED SAFFMAN-TAYLOR FLOWS

Experiments en fluxes de Saffman-Taylor modificats

Tesi presentada per l'obtenció del títol de

Doctor en Ciències Físiques

per

Jordi Ignés i Mullol

Director:
Dr. J.V. Maher
Professor of Physics
University of Pittsburgh

Ponent per la U.B.:
Dr. Jordi Ortín i Rull
Professor Titular de Física
Universitat de Barcelona

EXPERIMENTS ON PERTURBED SAFFMAN-TAYLOR FLOWS

Abstract

We have performed pattern formation experiments where a relatively well understood system (flow in a Hele-Shaw cell) is perturbed either by means of a lattice of grooves or by the use of viscoelastic fluids. We have extended the qualitative analysis found in the literature for anisotropic fingering patterns, presenting a more quantitative approach that may prove useful as a tool to attack more complex problems. We have analyzed the different morphological regimes and looked for signatures of the transition between phases, with partial success when we try to characterize a given morphology quantitatively.

In our studies of viscoelastic Hele-Shaw flow with associative polymer solutions, we have observed a transition from viscous fingering patterns into a regime where the growing patterns resemble the fracture in brittle solids. We have been able to rescale the threshold for these transitions, and we have observed interesting properties in a regime of fracturelike patterns where, under some circumstances, we have measured a characteristic oscillation frequency which shows interesting regularities. We have also studied the pressure in the viscoelastic flow, and found consistent results that may be used to implement a better theoretical model to fully understand the dynamics.

Foreword

Working towards a PhD. is certainly a very interesting period in someone's life. It has, for sure, been a very remarkable period in mine. In my case, living and getting to know a different country and way of life has added to the many experiences accumulated over these past few years. I have enjoyed a very active scientific environment, and I express my gratitude to Walter Goldburg, David Jasnow and Xiao-Lun Wu for many stimulating discussions. I would also like to thank my adviser, James Maher, because he has encouraged me to develop an independent attitude and has taught me to look for the *big picture* and not to get lost in the many details that experimental work involves.

I have also enjoyed working with my fellow graduate students Jignesh Gandhi, Levent Kurnaz, Kathy McCloud and Hong Zhao.

I would like to thank Aurora Hernández-Machado because her enthusiasm gave me the push to start all of this. I would also like to thank Jordi Ortín, who led me through the first steps in my work as an experimentalist.

I would like to acknowledge the financial support I enjoyed during the first two years through a fellowship from *Caixa d'Estalvis i Pensions de Barcelona*, whose excellent fellowship program and support were of great importance.

I dedicate this work to Noemi, whose smile is the best inspiration I can imagine.

Ho veus com tot és relatiu i complicat... Fem-ho fàcil!

Table of Contents

List of Figures

CHAPTER 1

Introduction

Pattern formation in soft condensed matter has been the object of extensive study for most of the past two decades [1–5]. The configuration we have used in the experiments described herein (Hele-Shaw cell, see Figure 1) is simple enough that the dynamical equations and the boundary conditions can be easily written down; yet, their non-linearity and non-locality generate a very rich variety of phenomena. The basic problem, where flat, smooth Hele-Shaw cells and Newtonian fluids are used, can be extended by introducing different kinds of perturbations, either by modifying the cell or by using a complex fluid system [6].

The patterns and phenomenology observed in our experiments with liquid dendrites (see chapter 3) have strong qualitative similarities with the dendritic patterns observed in crystal growth. In fact, the equations used to model both systems are so similar that the results we obtain in our simple experiments may well be applied in crystal growth. Additionally, experiments of crystal growth have typically much smaller length scales and time scales, which makes quantitative analysis more difficult. Our experiments with complex fluids exhibit a transition into patterns whose evolution shows strong qualitative similarities to that of experiments on fracture in brittle solids. In solid fracture, it is relevant to relate the onset of the fracture mechanism, and the subsequent dynamical development with the properties of the material. In our experiments of fluid fracture, we have information about the rheological properties of our polymeric fluids, and we try to relate these properties to the dynamical features we can measure. Moreover, the slower dynamics in our experiments allows for easier and more complete measurements than what is attainable in fracture of brittle materials.

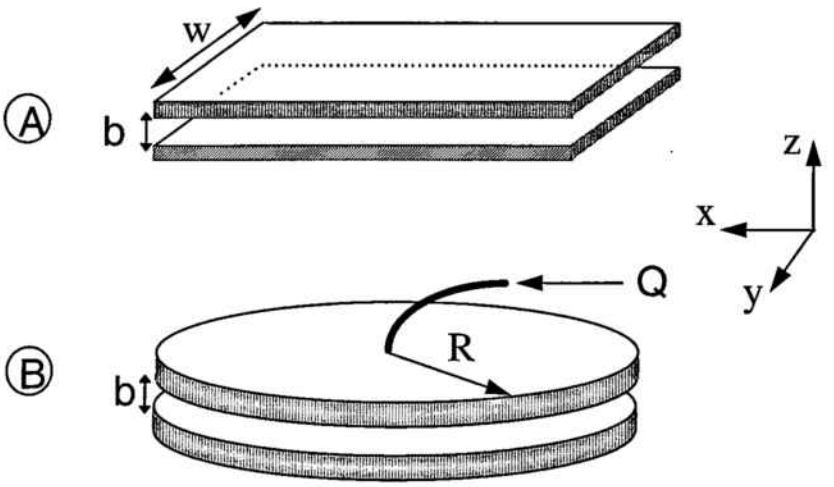

Figure 1: (A) Hele-Shaw cell in the channel geometry; (B) Hele-Shaw cell in the radial geometry.

1.1 Overview of the Viscous Fingering Instability

A Hele-Shaw cell is a system consisting of two rigid plates (usually made of glass or Plexiglas), placed parallel to each other with a small gap b between them (see Figure 1). The gap is filled with a viscous fluid. A second, less viscous fluid is forced to push the more viscous one. The most common case is that in which the viscosity of the invading fluid is negligible, when compared to that of the more viscous fluid.

Two geometries are commonly used: channel geometry, where the plates are rectangular and a pressure gradient is applied along the channel, with the less viscous fluid being injected from one end of the channel; and radial geometry, where the plates are circular, and a radial pressure gradient is applied by the less viscous fluid being injected through a hole at the center of the top plate. Interesting pattern formation happens when the moving interface between the fluids becomes unstable. The high impedance to the flow, due to the small cell gap, effectively constrains the fluids in a quasi two-dimensional motion. For this reason we can describe the flow and, particularly, the motion of the interface by the average fluid velocity across the gap. It can be shown (see Appendix A) that the same expression can be used to relate the average velocity field to the pressure gradient in the channel (equation A.8) and in

radial (equation A.17) geometry:

$$\vec{v} = \frac{b^2}{12\mu}\vec{\nabla}P, \tag{1.1}$$

where $\vec{v}$ is the flow velocity in the fluid, μ is the dynamic viscosity of the fluid, b is the cell gap and P is the pressure in the body of fluid.
The appearance of this equation is the same as that of the flow of a viscous fluid through a porous medium [7]:

$$\vec{v} = M\vec{\nabla}P, \tag{1.2}$$

and it is known as Darcy's law. M is the mobility of the medium. In the Hele-Shaw flow, the mobility is $M = b^2/(12\mu)$. In porous media, it is the ratio of the permeability of the medium to the viscosity of the invading fluid, $M = k/\mu$. Using Darcy's law to describe the flow in the cell effectively treats the flow as bi-dimensional, since the pressure gradient lies in the plane of the cell. This assumption will be valid as long as three dimensional effects are negligible. Examples of three dimensional effects are the presence of a three dimensional meniscus at the interface, or a Hele-Shaw cell where the gap b varies locally, $b = b(x, y)$.

Since we will be dealing with incompressible fluids,

$$\vec{\nabla} \cdot \vec{v} = 0. \tag{1.3}$$

Equation (1.1) and equation (1.3) lead to a pressure field that obeys the equation:

$$0 = \vec{\nabla} \cdot \vec{v} = \vec{\nabla} \cdot \frac{b^2}{12\mu}\vec{\nabla}P = \vec{\nabla}\left(\frac{b^2}{12\mu}\right) \cdot \vec{\nabla}P + \nabla^2 P = 0, \tag{1.4}$$

which leads to

$$\nabla^2 P = 0, \tag{1.5}$$

provided the term $b^2/12\mu$ is uniform over the cell.

1.1.1 Fluid-fluid interface

The situation relevant to the experiments in the present work is that where we have a moving interface between two fluids in a Hele-Shaw cell. Then, we will have a set

of bulk equations describing the flow in each fluid, with the two fluids viscosities μ_1, μ_2. At the interface, we will have to match the velocity fields in each constituent. Moreover, gravity may be relevant in the dynamics, unless the cell is perfectly horizontal. In what follows, we will neglect the viscosity of one of the fluids (we will have a very large viscosity contrast, $\mu_1/\mu_2 \sim 0$) and we will consider our cell to be horizontal (gravity plays no role). This approximation assumes implicitly that there is a negligible viscous dissipation in the lighter fluid, thus the pressure is uniform in this constituent. A treatment that includes both constituents and couples gravity with the flow can be found elsewhere [7] and the effect of the viscosity contrast is also addressed in the literature [8].

Our system is, then, the following: we have a moving interface that pushes a viscous fluid, of viscosity μ, and with a surface tension σ, being driven by a pressure gradient and constrained to move in a quasi two-dimensional system.

The pressure field satisfies Laplace's equation in the bulk (1.5). At the moving interface, there is a jump discontinuity in the pressure field, given by the Gibbs-Thomson equation [3],

$$P|_S = \sigma\left(\frac{2}{b} + \kappa\right) + P_0, \tag{1.6}$$

where $2/b$ is the curvature of the interface across the gap, assuming a $\theta = 0$ fluid-wall contact angle (true if the fluid wets the wall), in which case the profile is circular, with radius $b/2$ (with curvature $\kappa \sim 2/b$) as long as capillary effects are dominant. Gravity will start to deform the profile of the interface when b is *large*. With the fluids we commonly use, b should not be larger than 2 mm. κ is the two-dimensional curvature of the interface in the plane of the flow; and P_0 is the pressure in the less viscous constituent, whose viscous dissipation we neglect. Since P_0 and b are treated as constants, we rescale P to get, as a boundary condition,

$$P|_S = \sigma\kappa. \tag{1.7}$$

This, however, is only valid if the system can be treated as purely two-dimensional. It occurs that, if the fluid being displaced wets the walls, the interface leaves behind a layer of the fluid being displaced, whose thickness depends on the velocity. Park and Homsy [9] derived a corrected expression for the pressure jump, based on asymptotic

analysis:

$$P|_S = \frac{2\sigma}{b}\left[1 + 3.80\left(\frac{\mu v_n}{\sigma}\right)^{2/3}\right] + \frac{\pi}{4}\sigma\kappa + o\left(\frac{\mu v_n}{\sigma}\right)^{2/3}, \tag{1.8}$$

where v_n is the local normal velocity at the interface.

1.1.2 Radial Geometry

Consider the flow between two circular smooth plates, placed parallel to each other with a small gap b between them (radial Hele-Shaw cell, see Figure 1). The gap space is filled with a viscous fluid and a second, less viscous fluid is injected at a constant volumetric injection rate through a hole at the center of the top plate. Initially, a circular bubble will develop, but that regime is linearly unstable and *viscous fingers* grow until a size when a single finger is also unstable and tip splits [10].
As explained above, the system would be described by the following set of equations:

$$\vec{\nabla} \cdot \vec{v} = 0, \tag{1.9}$$

$$\vec{v} = \frac{b^2}{12\mu}\vec{\nabla}P, \tag{1.10}$$

$$\nabla^2 P = 0, \tag{1.11}$$

at the bulk (with $\vec{v}$ being the velocity in the displaced fluid, b the cell gap, μ the dynamic viscosity of the viscous fluid and P the pressure in the viscous fluid), and

$$P|_S = -\sigma\kappa, \tag{1.12}$$

$$\int \hat{n} \cdot \vec{v} ds = Q, \tag{1.13}$$

at the interface (with σ being the surface tension at the interface, κ the local curvature and Q the areal injection rate), where (1.13) constrains the flow to have constant (areal) injection rate. A growing bubble of the less viscous fluid, initially circular, becomes unstable, and it deforms by fingering into the more viscous fluid, with a characteristic wavelength that can be understood from this model (see appendix B).

The four dimensional parameters of the experiment – Q, b, μ and σ – can be combined to produce the dimensionless quantity $\mu Q/\sigma b$. Hence, if we try to render the above equations dimensionless, there will be freedom in the choice of units. A

customary choice is

$$L_0 = \frac{\sigma b^2}{6\mu Q}\ ,\quad T_0 = \frac{\pi^3\sigma^2 b^4}{18\mu^2 Q^3}\ ,\quad P_0 = \frac{6\mu Q}{\pi b^2}, \tag{1.14}$$

which gives the dimensionless set of equations:

$$\vec{\nabla}\cdot\vec{v} = 0, \tag{1.15}$$

$$\vec{v} = \vec{\nabla}P, \tag{1.16}$$

$$\nabla^2 P = 0, \tag{1.17}$$

$$P|_S = -\kappa, \tag{1.18}$$

$$\int \hat{n}\cdot\vec{v}ds = 2\pi. \tag{1.19}$$

If kinetic effects are taken into account, an extra term is added to eq. 1.12 and an extra parameter is introduced in the problem [9, 11, 12]:

$$P|_S = -\sigma\kappa + \beta v_n^{\gamma}. \tag{1.20}$$

The complexity of the problem increases when miscible fluids are used [13]; when spatial perturbations are added to the cell gap, in which case $b = b(x, y)$ is no longer uniform, or when non-Newtonian fluids are used, in which case $\mu = \mu(\vec{v})$. These modifications may cause the pressure field to cease to be Laplacian, so $\nabla^2 P \neq 0$.

1.1.3 Channel Geometry

Consider the flow between two rectangular smooth plates, placed parallel to each other with a small gap b between them (Hele-Shaw cell). The flow is restricted inside a channel by straight side walls (see Figure 1). Consider the gap space filled with two immiscible fluids, thus forming a flat interface. When a pressure gradient is applied along the channel, the interface advances. When the less viscous fluid is pushing the more viscous fluid, the flat interface becomes unstable [3, 7, 14].

After a transient, a steady state consisting of a finger of the less viscous fluid penetrating the more viscous one is formed. The shape of a finger which is growing from right to left can be expressed in terms of its width through a theoretically

expected relation [14]

$$x = \frac{W(\lambda - 1)}{\pi} \ln\left[\cos\left(\frac{\pi y}{\lambda W}\right)\right], \tag{1.21}$$

where λ is the ratio of the finger width to the channel width. This is the shape of the so-called Saffman-Taylor fingers [14]. This expression ignores surface tension, and should be useful for small surface tension interfaces, such as in the case of miscible fluids. The finger tip is supposed to be at (0,0), and the cell walls to be at $y = \pm W/2$. If we expand (1.21) around the tip we get

$$x = \frac{\pi W(1 - \lambda)}{2(\lambda W)^2} y^2 + \cdots, \tag{1.22}$$

which is the well known parabolic tip profile of the Saffman-Taylor fingers. A relationship that includes surface tension, and that fits slightly better the shape of wide fingers was found by Pitts [15].

The width of the finger is unique if there is a non-zero surface tension at the interface [16]. The relationship between λ and the surface tension has been measured experimentally [17]. It is convenient to define a surface tension parameter [18] as

$$\frac{1}{B} = \frac{12\mu V W^2}{\sigma b^2}, \tag{1.23}$$

where μ is the viscosity of the fluid being displaced (much higher than that of the displacing fluid), V is the finger tip velocity, W is the channel width, and σ is the interfacial surface tension).

Tabeling and Libchaber [17] included in the analysis of their measurements a wetting correction by using an effective surface tension

$$\sigma^* = \sigma\left[\frac{\pi}{4} + \alpha\lambda\left(\frac{W}{b}\right)\left(\frac{\mu V}{\sigma}\right)^{2/3}\right], \tag{1.24}$$

where α is a number related to the interface shape and is adjusted experimentally to rescale eq. (1.23). This correction accounts for the draining film left behind by the fluid that wets the walls, and was required to account for discrepancies between experiments and theoretical predictions. It is a first approximation to take into account the correction introduced in eq. (1.8). A more complete analysis of the inclusion of this wetting correction in the fingering equations has been given by Sarkar and Jasnow [19].

1.2 Perturbations to Radial Hele-Shaw Flow

The presence of anisotropy in the radial (isotropic) Hele-Shaw flow changes the nature of the problem in that new morphologies (such as dendrites) are possible. Ben Jacob *et al.* [20] proposed a phenomenological local model (Boundary Layer Model) to describe the dynamics of the advancing interface, which is applicable in solidification, Hele-Shaw flow, and other growth phenomena in chemistry and biology. They showed that the appearance of dendrites is a signature of the presence of anisotropy, even though it has been observed that even the presence of anisotropy is not enough to guarantee the appearance of dendritic patterns (it has been shown before [21], and we will give some examples from our own experiments, that tip splitting morphologies are found, under some dynamical conditions, in the presence of anisotropy).

The experimental details of the perturbation that adds anisotropy to the flow have many possible realizations. In the literature we find how a bubble at the tip of a growing viscous finger in smooth (isotropic) Hele-Shaw cells generates dendritic branches [22, 23]. We also find experiments where the anisotropy is provided by the fluid being displaced, such as experiments with liquid crystals [5, 24, 25], where dendritic phases are observed. The experiments that offer a better control of the perturbation, however, are those where the anisotropy is introduced by means of a lattice of grooves etched on one of the plates of the cell. We find in the literature systematic qualitative descriptions of the morphologies observed with a single groove [26], with series of parallel grooves [27], and with a regular array of grooves [21]. The qualitative effect of different control parameters is described in these works, particularly the effect of the driving force (a pressure gradient) and the ratio of the depth of the grooves to the cell gap. However, a quantitative study of the experimental observations is not found in the literature, and it is not clear how to quantitatively relate the experimental control parameters to the parameter that introduces the anisotropy in the theoretical analysis. The use of an etched array of grooves offers the best control over the experimental parameters and, since the lattice is unaltered in the experiments, it offers very reproducible results.

1.3 Hele-Shaw flow with viscoelastic fluids

The use of viscoelastic fluids in Hele-Shaw flow should have important effects as long as the flow enters a dynamical regime where the possible non-Newtonian features of the fluid (non-zero normal stresses, shear thinning/shear thickening, yield stress, stress relaxation, etc.) become important. As we will explain in chapter 2, perturbations to the flow of Newtonian fluids have an effect mostly in the interfacial region. When the flow becomes non-Newtonian, with a velocity dependent shear viscosity (see eq. 1.1), the perturbations should be relevant, not only in the interfacial region, but also in the bulk of the fluid. The effects of viscoelastic fluids in Hele-Shaw flow were first studied in experiments by Nittman, Dacord and Stanley [28, 29], showing interesting qualitative effects. Further experimental work was performed by van Damme *et al.* [30–33]. The effects of viscoelastic fluids in Hele-Shaw flow have also been studied by de Gennes [34]. Viscoelastic effects in patterns between miscible fluids have been recently studied in experiments [35, 36] showing drastic changes in the morphology of the patterns that can be obtained by changing the rheology of the polymeric solutions. The fact that the rheological properties of viscoelastic materials depend on the dynamical regime in which the flow is taking place allows for a very rich variety of phenomena. It is particularly interesting that, under some high flow conditions, viscoelastic fluids can be made to generate fracturelike patterns, whose morphologies resemble more the fracture in brittle materials than the flow of a Newtonian viscous fluid in a Hele-Shaw cell. Such observations have been made in clay suspensions [31–33, 37] and in associative polymer solutions [38]. The resemblance between these systems and the fracture in brittle materials suggests several possible approaches to study the dynamics governing the observed behavior.

1.4 Overview of the following chapters

In the following chapters we will describe experiments where perturbations have been added to the basic Hele-Shaw flow. In chapters two through four we present radial fingering experiments with Newtonian fluids, where the cell gap is non-uniform, and it changes periodically over the cell. This generates a rich variety of anisotropic fingering patterns, particularly dendritic regimes, which we present both qualitatively and with

a quantitative analysis. Our quantitative analysis is based on a time scaling of the tip position of the growing dendrites, only found in the presence of anisotropy. The shape of the dendrite is also well described by the model, which we find to be strongly self consistent. Even though this model proves to be a promising tool to quantitatively analyze the effect of the periodic gap perturbations on the Hele-Shaw flow, we have been only partially successful at characterizing quantitatively the morphology of the patterns resulting from a given flow realization [39].

The second half of this thesis describes our experiments with viscoelastic fluids (associative polymer solutions) which exhibit a transition from fluidlike into solidlike behavior. Chapters five through seven describe our viscous flow experiments in a Hele-Shaw channel using viscoelastic fluids, so $\mu = \mu(\vec{v})$ is no longer a constant. We have observed a transition from viscous fingering into fracturelike behavior, where the evolving patterns resemble, both because of their morphology and because of their dynamics, the fracture of brittle materials. We describe our successful (although limited) rescaling of the onset of the fracturelike instability, and the consistent trends found in the evolution of the characteristic frequency of the oscillating regimes when we study its changes with the different control parameters [40]. We also explain our attempts at obtaining a more complete understanding of the observed phenomena by studying the shear stress in the viscoelastic medium, even though it is a quantity we cannot measure directly.

CHAPTER 2

Introduction of a regular perturbation in the radial cell. Qualitative aspects.

[Regular perturbation in a radial cell. Qualitative.] Anisotropy, frequently introduced experimentally in the Hele-Shaw flow as a perturbation in the uniformity of the gap, generates a rich variety of morphologies not present in the isotropic flow [10] (that is, in the flow of an isotropic material in a homogeneous Hele-Shaw cell. See appendix B). Before this work, however, the distinctions between the different morphologies were mainly qualitative. In the following two chapters, we describe a set of experiments designed to find a quantitative signature of the anisotropy that would allow us to characterize a given morphology, and to study the transitions among different morphologies from a more quantitative point of view.

We have designed an experiment where the anisotropy is introduced in a very controlled fashion, by adding a regular array of grooves inside the Hele-Shaw cell. In this chapter we give an overview of the different morphologies that we have observed, and we discuss the effect of the different control parameters in our experiment, from a mainly qualitative point of view. We explain how the qualitative effects we observe are consistent with what has been described in the literature. We notice, in particular, that the relative strength of the gap modulations has a dramatic effect on the morphology. We also give a brief overview of the standard mathematical description of the anisotropy and note that we lack a clear (quantitative) relation between the anisotropy parameter found in such models and our experimental control parameters.

In the next chapter, we discuss a recent model that allows a quantitative analysis of the effect of the anisotropy on the fingering patterns, based on asymptotic scaling in the evolution of the fluid dendrites. We describe the predictions of the model, including the expected asymptotic shape of the dendrites, and describe how it has proven a useful tool in our experiments, even though we have achieved only partial

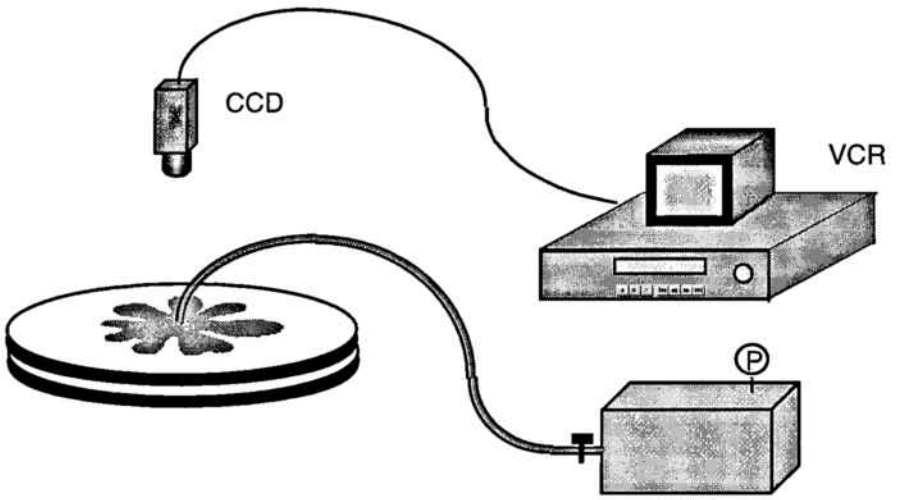

Figure 2: Experimental design and data acquisition procedure in the radial fingering experiments.

success when we try to quantitatively characterize a given morphology.

2.1 Experimental design and measurement procedure. Etched lattice.

We have performed viscous fingering experiments on a radial Hele-Shaw cell with glass plates. The top plate was 1 inch thick (to minimize plate flexing [18]) and 23 inches in diameter (1 inch $\simeq$ 2.54 cm). We measured plate flexing at the center of the plate on a high pressure situation using a strain gauge and found a flexion of 50.8 μm over a radius of 15.5 in. Heavy paraffin oil, with $\mu = 1.6$ P (1 Poise = 1 g cm^{-1} s^{-1}) and oil-air surface tension $\sigma = 35$ dyn cm^{-1} at 22°C, acted as the more viscous fluid. Dry nitrogen was injected at a constant volumetric injection rate, which translates into a constant areal injection rate Q if the bubble has a uniform gap thickness (close to the cell gap). The constancy of the injection rate was achieved by preparing a large reservoir with nitrogen at an intermediate pressure P (see Figure 2) and setting a large impedance to the flow at the output from this reservoir with the help of a throttle valve. This way, the flow rate was dictated by this fixed large impedance, rather than by the impedance due to the evolution of the pressure field inside of the cell. The developing fingering patterns were observed with a CCD [41] video camera

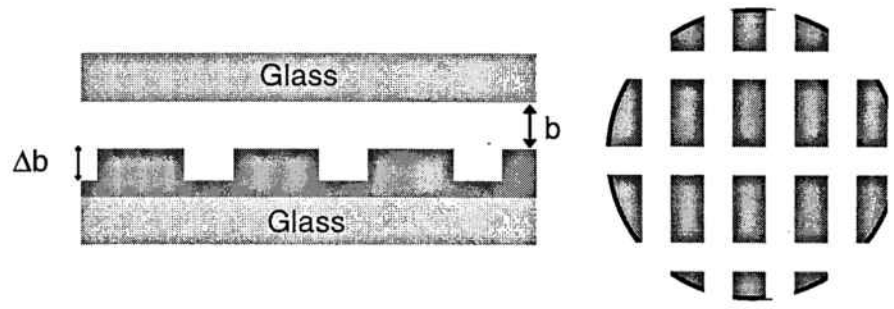

Figure 3: Left: Profile of the etched plate inside of the cell gap. Right: Top view of the etching.

and taped on an Enhanced S-VHS recorder [42]. The images were then digitized and analyzed with the assistance of image analysis software [43].

To introduce the anisotropy, a plate was superimposed on the bottom glass plate of the cell (see Figure 3). The new plate was a large circuit board (25 x 50 cm^2) with its copper layer photochemically etched to produce a rectangular lattice pattern. The grooves were 0.2 mm wide, 0.4 mm center to center in one direction and 0.8 mm center to center in the other direction, with a depth of 0.07 mm, thus forming rectangular islands of copper, 0.2 x 0.6 mm^2 in size, 0.07 mm in height and 0.2 mm of spacing between neighboring edges.

The plates were designed with the software package AUTOCAD [44]. The pattern was easy to encode since it is a regular array of grooves. The design was transferred to DXF image file format to be used by the circuit board manufacturing company, which was responsible for the photochemical etching process of the design on a bare copper layer of 2 oz./$ft.^2$ (0.07 mm thick).

Spacers were used to keep the top and bottom plates at a uniform distance b, thus setting the cell gap. Measurements were made with gaps ranging from 0.11 to 1.0 mm.

2.2 Anisotropy and dendritic growth. Different morphologies

It is known [20, 45] that the presence of anisotropy is required in order to get dendritic patterns, both in directional solidification and in viscous fingering. The effect of the anisotropy on the flow, however, depends on several control parameters such as the cell gap, the driving force, the length scale of the etching, etc., and, as a result, different morphologies can be obtained, and morphology phase transitions between them can be observed [46]. For instance, as the driving force increases, the morphology progresses through a faceted regime, to a regime of surface tension dendrites, to a tip-splitting regime and finally to a regime of kinetic dendrites (see below for a description of each regime and for the origin of the nomenclature, based on what is found in the literature [46]). An example is given in Figure 4 where, for a gap $b = 0.11$ mm, very different morphologies can be obtained in our experiments of viscous flow over a rectangular lattice, by changing Q: $Q = 1.3$ cm^2/s generates surface-tension-controlled dendrites; $Q = 1.8$ cm^2/s generates a tip-splitting regime; $Q = 5.5$ cm^2/s generates a 2-fold symmetric pattern with kinetic dendrites along one direction, but with tip splitting along the perpendicular direction (*2-way kinetic dendrites*); and $Q = 48$ cm^2/s generates a 2-fold symmetric pattern with kinetic dendrites along perpendicular directions (*4-way kinetic dendrites*). It is a remarkable fact that the effect of the anisotropy, which is introduced at very small length scales, is reflected at macroscopic length scales. The characteristic length scale of the etching is of the order of a few tenths of a millimeter, yet the observed fingering patterns have a size of tens of centimeters, and the symmetry of the etching (twofold, fourfold, etc.) generates patterns with the same symmetry, but at much larger length scales.

In our experiments, we have focused, mainly, on the two dendritic morphologies (see Figure 4):

- at *low velocities*, dendrites grow away from the etched grooves, presumably because of surface tension effects, since minimization of the surface energy of the growing patterns requires the cross sectional area to be a minimum, and that occurs away from the grooves;
- at *high velocities*, dendrites grow along grooves, presumably because of kinetic

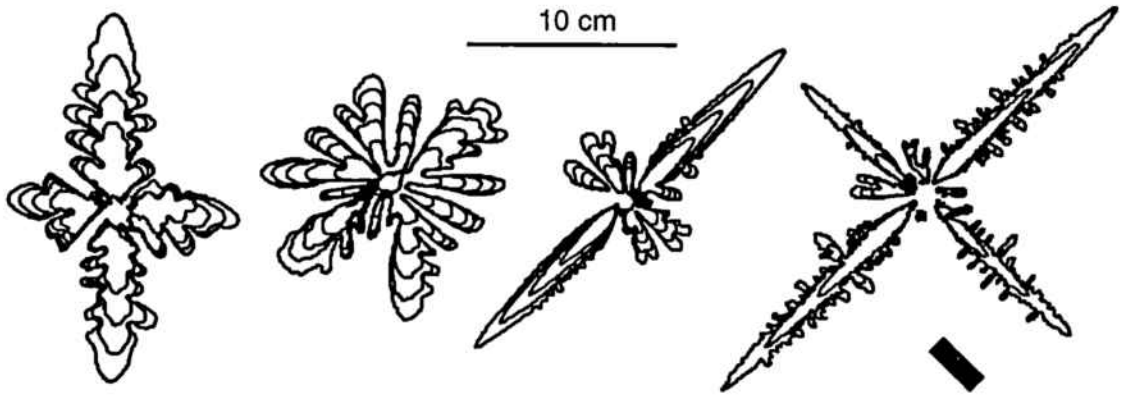

Figure 4: Anisotropic fingering morphologies for $b = 0.11$ mm. The rectangle shows the orientation of the etching. From left to right: $Q = 1.3$ cm^2/s, $Q = 1.8$ cm^2/s, $Q = 5.5$ cm^2/s, and $Q = 48$ cm^2/s.

effects, since the most favorable configuration is the one that minimizes the impedance to the flow, and that occurs along the grooves.

2.3 Mathematical description of the Anisotropy

Even though anisotropy acts as a singular perturbation when introduced in these flow situations [4], its effects on the patterns depend on the strength of that anisotropy. If the strength is very low, the anisotropic effects will become negligible, and regular growth based on tip splitting will dominate [47].

In a theoretical analysis, the effect of the anisotropy appears in the pressure boundary condition (1.20) as:

$$P|_S = \sigma f(\theta)\kappa + \beta g(\theta) v_n^\gamma, \tag{2.1}$$

where σ is the surface tension, β is a kinetic coefficient, θ is the local angle between the normal to the interface and the lattice, v_n is the local normal velocity and κ is the local curvature. The term proportional to v_n should dominate at high speeds (kinetic dendrites) while the term proportional to the curvature should dominate at low velocities (surface tension dendrites). Given that $f(\theta)$ and $g(\theta)$ should reflect the

symmetry of the lattice, it is customary to use expressions of the kind

$$f(\theta) = 1 - \epsilon \cos(m\theta), \tag{2.2}$$

$$g(\theta) = 1 - \chi \cos(m\theta + \delta), \tag{2.3}$$

where ϵ and χ are the anisotropy parameters, and they should quantify the effect of the lattice on the patterns, i.e., they should quantify the strength of the anisotropy. m gives the symmetry of the anisotropy (2-fold, 4-fold, etc.). The phase shift δ allows for some competition between kinetic and static terms in the selection of the direction of growth (for instance, $\delta \sim 45°$ seems to be what we would infer from our experimental observations, since growth in directions 45° apart occurs when surface tension effects dominate and when kinetic effects dominate (see Figure 4)).

Sarkar and Jasnow [47] studied the effect that a regular perturbation on b would have on the fingering patterns, by analyzing first its effect on the equations. They first note that, if b is not uniform, then the pressure field ceases, in general, to be Laplacian. They argue that the two-dimensional mobility (which, for the smooth plates case is the scalar $b^2/(12\mu)$) can be expressed as a tensor. This tensor could be diagonalized and, in the case of four fold symmetric perturbations, the eigenvalues would be equal. Then, they argue, if the length scale of the etching is small enough, we could coarse grain the pressure field, so that the coarse grained mobility would have space independent elements. In our case, we have a two fold symmetric etching, so the coarse grained mobility will have different (constant) eigenvalues. Thus, according to that analysis, a rectangular etching could modify the bulk equations for the flow.

We have observed, however, that simulations by Almgren [48] assuming two-fold symmetry generate patterns which are in at least qualitative agreement with our experiments, even though the equations he uses include the anisotropy in the boundary conditions only (the bulk pressure field is considered to be Laplacian).

2.4 Experimental control parameters

In our experiments, we have observed that the morphology of the viscous fingering patterns can be altered by three control parameters: $a = \Delta b/b$, the ratio between the depth of the grooves to the average cell gap; Q, the areal injection rate; and the

length scale of the gap modulations, that is, the length scale of the etched lattice. Since our plate has a rectangular etching, we will have two such length scales (see Figure 3).

We are still not confident of how to write down an expression for an anisotropy parameter of the kind present in equation (2.2), but such a parameter should depend on the experimental control parameters, and that dependence should take into account their experimentally observed effects on the patterns:

- An increase in a dramatically increases the effect of the anisotropy on the patterns. For instance, we cannot observe any clear effect of the etching on the fingering patterns for $b > 1.0$ mm, that is, for $a < 0.07$.
- An increase in Q seems to increase the effect of the anisotropy on the patterns. For a large value of a, such as $a = 0.64$ (see Figure 4), increasing Q makes the morphology change from surface tension dendrites to tip-splitting to kinetic dendrites. But within a given dendritic morphology, increasing Q increases the effect of the anisotropy since, for instance, kinetic dendrites become sharper when we increase Q.
- An increase in the length scale of the anisotropy also increases its effect on the patterns. We can see an influence of this length scale on the third pattern from the left on Figure 4, which exhibits sharp kinetic dendrites along one side of the rectangles, while along the other side, we are still in a tip-splitting dominated regime. Also, on experiments with a square etching with a length scale equal to the short side of the rectangles here, one observes that, with the same value of a and Q, the effect of the anisotropy is smaller than in the rectangular case, presumably because of the longer length scale in the rectangular lattice.

The effect of the anisotropy on a given flow realization is given by a combination of all these parameters. The examples on Figure 4 are for flows on the same lattice, for a fixed gap $b = 0.11$ mm, and for different values of Q. We have been able to observe similar morphologies after changing the gap. However, in order to generate the same qualitative morphology with different gaps, very different values for the injection rate are required. For instance, obtaining the *two-way kinetic* dendritic morphology in Figure 4, with a gap $b = 0.11$ mm, requires Q =5.5 cm^2/s, but with a gap $b = 0.22$ mm, it requires $Q \sim 32$ cm^2/s to obtain a qualitatively similar pattern. The effect of

the anisotropy, thus, depends more dramatically on a, since small changes in a have a strong effect on the morphology.

Sarkar and Jasnow [47] found that if the magnitude of their anisotropy parameter (see eq. 2.2) was less that 0.07, the effect of the anisotropy started to vanish. We are not confident on how to relate this anisotropy parameter with our experimental control parameters, even though, as explained above, we cannot observe any effect of the etching on the fingering patterns for $a < 0.07$.

CHAPTER 3

Introduction of a regular perturbation in the radial cell. Quantitative analysis.

We have seen, in the previous chapter, the dramatic effect anisotropy has on the morphology of the viscous fingering patterns. In particular, it can originate dendritic branches, which grow with a very stable tip, unlike the tip splitting growth dynamics typical of isotropic Hele-shaw flow. The description of these effects, however, has been mainly qualitative. A good model to quantitatively analyze this pattern formation system was lacking. In this chapter, we explore a model that yields very consistent results in the quantitative description of liquid dendrites.

3.1 Theoretical model

Almgren *et al.* [49] studied the growth of fingering patterns in the presence of anisotropy by introducing an anisotropy term in the pressure boundary condition:

$$P|_S \sim \kappa(1 - \epsilon\cos(m\theta)). \tag{3.1}$$

Their work neglected kinetic effects completely. This is a simplification of the problem, but might appropriately be matched with the experiments at low driving force (assuming kinetic effects become small and possibly negligible). Their analysis presents asymptotic effects in the dynamics that are only possible in the presence of anisotropy.

3.1.1 Asymptotic Scaling

Almgren *et al.* [49] predicted that, in the presence of anisotropy in the surface tension, the distance from the tip of a growing (surface-tension) dendrite to the injection point should scale with time as

$$x_{tip} = At^{\alpha}, \tag{3.2}$$

with $\alpha = 3/5$. If x is the coordinate along the axis of a growing dendrite, and y is perpendicular to that axis then, using simulation, they encounter a scaling behavior

$$x \sim t^{\alpha}, \tag{3.3}$$

$$y \sim t^{1-\alpha}, \tag{3.4}$$

where the fact that the exponents add up to one is a result of the constraint that the flow has constant injection rate (either areal or volumetric), so that the area of the pattern should grow linearly with time,

$$xy \sim t, \tag{3.5}$$

for any point inside a growing dendrite. This would be true if the flow is equally distributed among all dendrites (so that the individual area grows linearly with time, and not only the total area of the multi-branched bubble). This is automatically satisfied in the simulations but is not always satisfied experimentally. The predicted scaling behavior is asymptotic and experiments should observe it only after transients have relaxed. At each instant, the dendrite tip has the speed predicted by steady-state theory [4]. Then, nondimensionalization yields the result that the steady-state tip should have a value for $\rho^2 V/d_0$ independent of time (it would be some function of the anisotropy parameter), where ρ is the tip radius of curvature, V is the tip velocity and d_0 is the surface tension parameter. Considering the scaling assumption $x \sim t^{\alpha}$, $y \sim t^{1-\alpha}$, we have

$$V = \frac{dx}{dt} \sim t^{\alpha-1},$$

and

$$\rho \sim \frac{d^2x}{dy^2} \sim \frac{t^{2\alpha}}{t^{2-2\alpha}} = t^{4\alpha-2}.$$

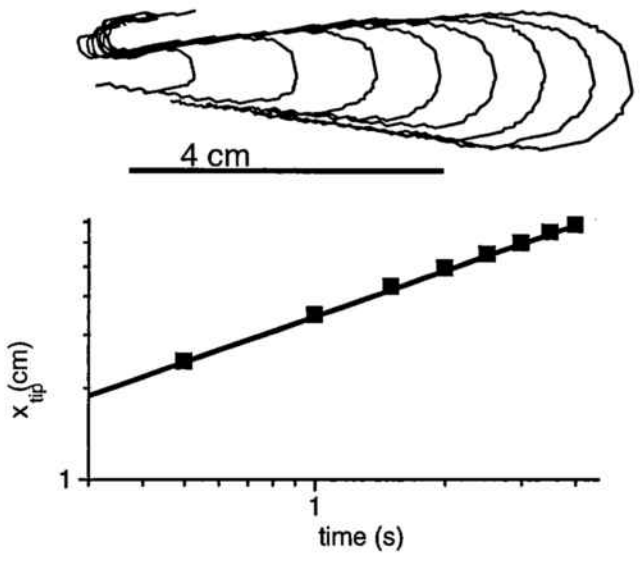

Figure 5: Scaling in isotropic fingering (smooth plates). A perfect $x_{tip} \sim t^{0.5}$ is found.

Then, if $\rho^2 V$ is independent of time,

$$\rho^2 V \sim t^{4\alpha-2} t^{\alpha-1} = t^{5\alpha-3} = cnt. \tag{3.6}$$

From here, $\alpha = 3/5$ $(= 0.6)$. Following the same arguments, it is easy to see that in the isotropic case (smooth plates), the only scaling should be $\alpha = 0.5$ (the same for x and y axes) [18, 50]. Moreover, one would need to obtain a finger that does not change topology (no tip splitting) and that does not feel a strong competition with the other fingers (its area should grow linearly with time) in order to observe such scaling. In Figure 5 we have an example of that. A finger, growing in a smooth Hele-Shaw cell, which seems to suffer no competition effects, and before tip-splitting, displays a perfect $x_{tip} = At^{\alpha}$ scaling with $\alpha = 0.5$.

3.1.2 Asymptotic Shape

Almgren *et al.* were also able to find the asymptotic shape to which the time-rescaled dendrites should converge. This curve has a dependence on the symmetry of the etching and is based on the finger being isolated (growing unperturbed by the other fingers). The exponent α, however, will be universal: the same for all kinds of surface-tension-anisotropy, regardless of the details of that anisotropy. Almgren

gives the following expression for the shape of the asymptotic branch, with x being along the symmetry axis of the dendrite and y perpendicular to x:

$$y(x,t) = \frac{Q}{2\pi}\frac{1}{\alpha A}t^{2/5}Y_m\left(\frac{x}{At^\alpha}\right), \tag{3.7}$$

where

$$Y_m(\rho) = \rho^{2/3}\int_\rho^1 \frac{ds}{s^\gamma\sqrt{1-s^m}}, \quad \gamma = \frac{5}{2} - \left(\frac{m}{2}-1\right), \tag{3.8}$$

with A and α obtained from the scaling behavior of the tip position (eq. 3.2). In the above equations, the anisotropy (and, thus, the resulting patterns) has m-fold symmetry. These expressions are derived after considering an anisotropic flow with constant Q and assuming the tip scaling hypothesis. Then the shape is derived by replacing the fingers by a cross of m arms (m even) in the complex plane, and considering the potential field around the cross to satisfy

$$w(z) = \frac{2}{m}\cosh^{-1}\left(\frac{z}{R}\right)^{m/2}. \tag{3.9}$$

3.1.3 Expected evolution of A

As we will see in section (3.2.4), A presents an interesting regularity in its evolution with Q. Karma has pointed out to us that the dependence of A on Q at fixed b can be easily understood with some dimensional analysis [51] as follows: The equations of viscous flow in a radial Hele-Shaw cell can be made dimensionless by the customary choice of units showed in eq. 1.14. Since μ (viscosity) and σ (surface tension) remain unchanged in our experiments, we just need to focus on the dependence on Q and b. The above mentioned choice of units, namely, $P_0 \sim Q$, $L_0 \sim Q^{-1}$ and $T_0 \sim Q^{-3}$, effectively removes all dependence on Q from the equations. With this, the dimensionless pressure (p'), time (t') and tip position (x') are expressed: $x \sim x'/Q$, $t \sim t'/Q^3$ and $p \sim Qp'$. Then, if we assume a scaling behavior $x' \sim A't'^\alpha$ (now A' is independent of Q, since Q is no longer present in the equations), the dimensional variables will verify:

$$x \sim x'/Q \sim A't'^\alpha/Q \sim A'(tQ^3)^\alpha/Q = A'Q^{3\alpha-1}t^\alpha. \tag{3.10}$$

If $\alpha = 0.6$, then $\beta = 3\alpha - 1 = 0.8$ is expected. We can also explore what dependence would A have on b by including b in the former analysis.

If we include b, then the characteristic units of the problem go as $P_0 \sim Q/b^2$, $L_0 \sim b^2/Q$ and $T_0 \sim b^4/Q^3$ (see eq. 1.14). Once more, assuming $x' \sim A' t'^{\alpha}$ we will have

$$x = x' L_0 \sim L_0 A' \left(\frac{tQ^3}{b^4}\right)^{\alpha} \sim A' \frac{b^2}{Q} t^{\alpha} Q^{3\alpha} b^{-4\alpha} = A' Q^{3\alpha-1} b^{2(1-2\alpha)} t^{\alpha}. \tag{3.11}$$

So the expected behavior is $A \sim A' Q^{3\alpha-1} b^{2(1-2\alpha)}$. If $\alpha \sim 0.6$ this becomes $A \sim A' Q^{0.8} b^{-0.4}$ or, in a more compact way

$$A \sim A' \left(\frac{Q}{\sqrt{b}}\right)^{0.8}. \tag{3.12}$$

3.2 Experimental procedure and observations

To investigate the scaling behavior, we must obtain dendritic branches whose area grows linearly with time, that is, dendritic pieces of a larger pattern that are fed by a constant injection rate. Even though the analysis in [49] is restricted to surface tension controlled dendrites, we extend the analysis to kinetic controlled dendrites as well. We have observed power-law behavior of the tip position in both regimes.

3.2.1 Experimental Procedure

As described in section 2.1, a typical flow realization consists on injection of dry nitrogen, at a constant injection rate, into a radial Hele-Shaw cell whose gap is filled with heavy paraffin oil, and with a bottom plate that has a rectangular lattice of grooves etched on it. We record the growth of the fingering pattern and digitize each frame into the computer. Our analysis proceeds as follows:

1.- For a dendrite in a given run, we examine successive frames (up to 30 frames/sec), and for each frame we obtain its contour shape, from which we can measure the area and the tip position. This yields a time series for the area and the tip position.

2.- From the time series of the tip position, we obtain the time series for the distance from the tip to the injection point, x_{tip}, and try to fit to $x_{tip} = At^{\alpha}$. Sometimes, it is required to allow a small time shift t_0 to be fitted, due to a small uncertainty on the starting time for the flow, possibly including a transient time for the asymptotic flow to set up. We always require this time shift to be small, as compared to the time it takes the pattern to evolve. Also, we usually discard some of the first few frames, wherein shapes might be dominated by the transient.

For each run, the pattern evolution of each of the dendrite branches obtained (up to four branches for high Q) was analyzed independently. The flow was not in general distributed uniformly among the different growing branches so the area of each branch within the same run would grow at a different rate. For this reason, we used the rate of growth of the area for each branch, $\tilde{Q}$, as the relevant parameter instead of the global injection rate for the run. Doing this allowed us to obtain one independent value for A and one for α for each of the branches, up to 4 independent values for each flow realization. With this, we obtain a series of pairs (α, A) as a function of our control parameters $(b, \tilde{Q})$.

3.2.2 Dependence of α on morphology

In general, there is a dispersion in the values of α, so patterns corresponding to the same morphology generate values of α that can be quite different:

- In the surface-tension-controlled regime, the analysis of 45 branches for several different gaps yields an average $\bar{\alpha} = 0.64$ with a large standard deviation $\sigma_{\alpha} = 0.098$.
- The analysis of 29 kinetic-controlled branches yields an average $\bar{\alpha} = 0.66$ with a standard deviation $\sigma_{\alpha} = 0.096$.

Therefore, we can see no significant difference between the values of α in both regimes. A generalized trend is for the value of α to be larger than 0.5 (the one expected in the absence of anisotropy) and consistent with the value of 0.6 predicted in the

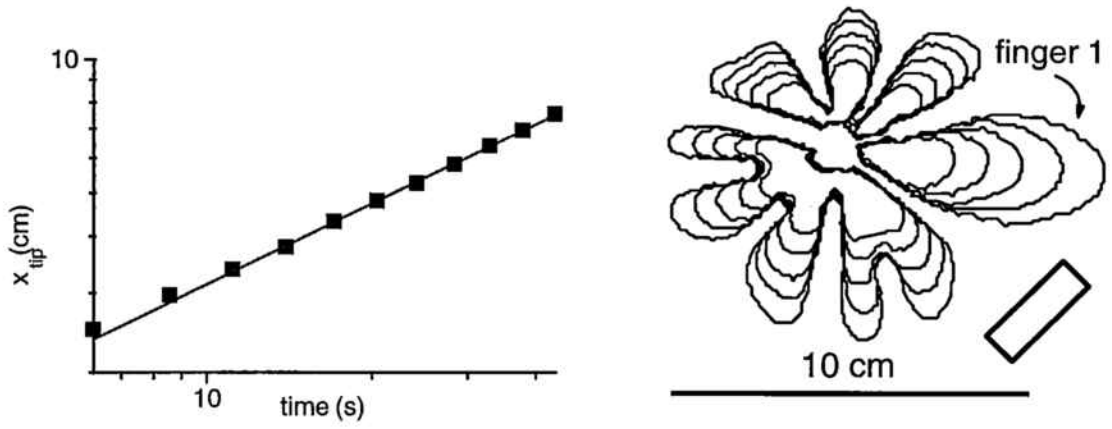

Figure 6: Digitized patterns (right) and fit of tip position to t^{α} for the fastest growing branch (left) corresponding to a surface tension dendrite. A value $\alpha = 0.6$ is found. The rectangle shows the orientation of the etching.

case of surface tension controlled flow. In Figure 6 a run that generates a surface-tension dendrite is shown, and the scaling exponent has a value in agreement with the expected 0.6. The rectangle in the graph represents the orientation of the pattern. Figure 7 shows a run in the kinetic controlled regime, where dendritic branches follow the grooves. The rectangle in the graph represents the orientation of the pattern. The dominant branch is analyzed, and yields a value for α larger than 0.6 ($\alpha = 0.64$).

Some preliminary arguments by Almgren [48] lead to the conclusion that a value $\alpha = 2/3$ is what should be found in the kinetic controlled regime, regardless of the symmetry of the anisotropy.

3.2.3 Observation of the Asymptotic Shape

In Figure 6 a run that generates a surface-tension dendrite is shown. For this particular run, the rescaled shape does not conform with the asymptotic shapes found in [49], probably because of some interaction with the rest of the bubble, far behind the tip. The fact that the scaling of the tip position is so clear, however, can be interpreted as a sign that the selected velocity is only affected by what happens in the neighborhood of the tip, and not on the full shape. For the run shown in Figure 7, corresponding to kinetic controlled dendrites, using the value of Q for the whole bub-

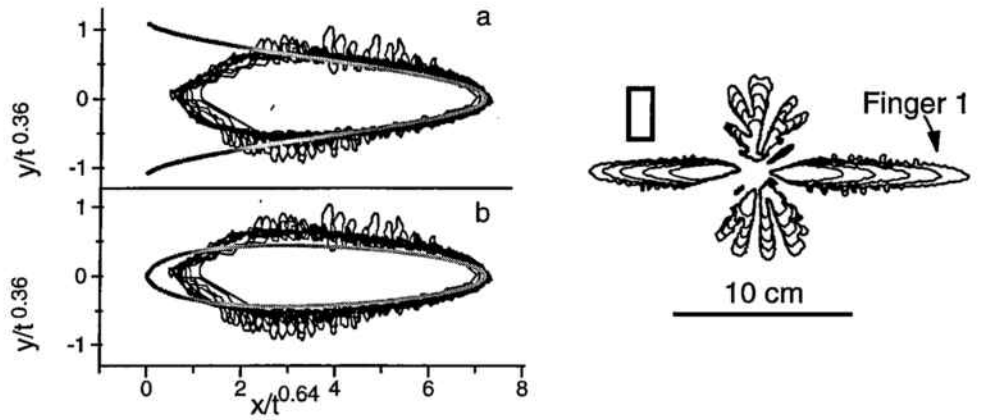

Figure 7: Observation of the predicted asymptotic shape for kinetic dendrites: (a) 2-fold symmetry, (b) 4-fold symmetry. The 2-fold shape adjusts better to our data. The evolving kinetic dendrite (right) has been rescaled, using $\alpha = 0.64$. The rectangle shows the orientation of the etching.

ble, and the fitted value $\alpha = 0.64$, we compare the rescaled data with the predicted asymptotic shape in the case of 2-fold (a) and 4-fold (b) symmetry (see equation 3.7). We notice that the 2-fold shape adjusts better to our data (see Figure 7) which is what we would expect from having rectangular symmetry in the etching. Since the analysis that yields the theoretical expression for the asymptotic shapes relies on the symmetry of the problem, it may be reasonable that the same expressions could be used for surface-tension-controlled and for kinetic-controlled dendrites.

3.2.4 Regularity in A vs. $\tilde{Q}$. Confirmation of the scaling assumption

For 4-fold symmetry (the case studied in [49]) the value of A as a function of ϵ has been computed analytically [52]. In our case, with 2-fold symmetry and no reliable procedure to relate our experimental parameters with the anisotropy parameter ϵ that the theoretical treatment deals with, we must look for empirical regularity. Most of the values for α we obtain are scattered around $\alpha = 0.6$ (the value expected for surface tension dendrites in [49]). Our analysis concentrates on the dendrites that scale with $\alpha = 0.6$ (within experimental uncertainty).

When we plot A vs. $\tilde{Q}$, keeping the gap b fixed we see the data align in a simple pattern which we can roughly describe with a power law: $A \sim \tilde{Q}^{\beta}$ (see Figure 8). In

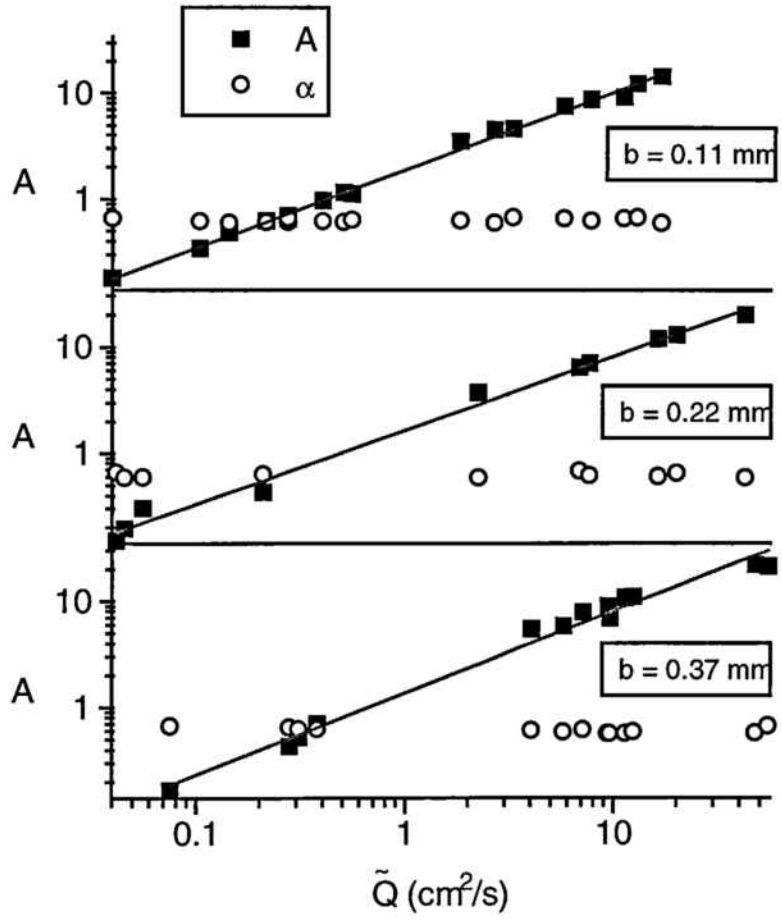

Figure 8: Anisotropic fingering. Dependence of A (solid squares) on $\tilde{Q}$ for $\alpha \sim 0.6$ at three different values of the gap b.

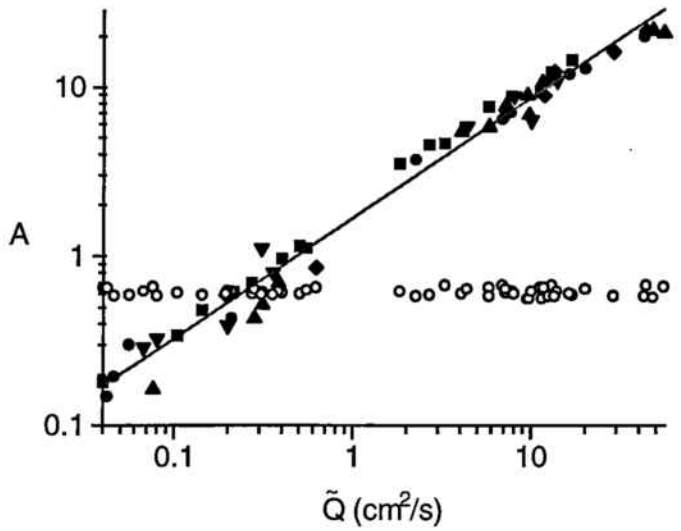

Figure 9: Anisotropic fingering. A (solid symbols) vs $\tilde{Q}$ with $\alpha \sim 0.6$ (o) combining gaps that range from $b = 0.11$ mm up to $b = 0.37$ mm. Different symbols correspond to different gaps.

Figure 8 no distinction has been made between surface tension and kinetic dendrites, so branches from both regimes are present on the same graph. Note a regime of $\tilde{Q}$ values where there are no data. That regime connects surface tension dendrites (low $\tilde{Q}$) with kinetic dendrites (high $\tilde{Q}$) and there, tip-splitting dominates the dynamics. The exponent of the power law is: top, $\beta = 0.74 \pm 0.01$ for $b = 0.11$ mm; middle, $\beta = 0.70 \pm 0.02$ for $b = 0.22$ mm; bottom, $\beta = 0.77 \pm 0.03$ for $b = 0.37$ mm; open circles are the values of α for each case. The analysis presented in section (3.1.3) predicts a value $\beta = 0.8$.

An even more striking result is that, if we put together in the same graph the data obtained from different gaps, they superimpose, showing an apparent lack of dependence on the gap, as we can see in Figure 9. The two groups of data points we can see in that graph, with a range of injection rate in between where no dendrites are found, correspond to surface tension dendrites (low $\tilde{Q}$) and kinetic dendrites (high $\tilde{Q}$). Gaps range from $b = 0.011$ cm up to $b = 0.037$ cm. In the surface tension regime, $\bar{\alpha} = 0.62 \pm 0.02$ (24 points) and in the kinetic regime, $\bar{\alpha} = 0.61 \pm 0.04$ (32 points). The combined statistics are $\bar{\alpha} = 0.61 \pm 0.03$ (56 points). The fit to a power law yields an exponent $\beta = 0.71 \pm 0.01$.

If we use the result presented in Eq. 3.12 where b is included in the dimensional

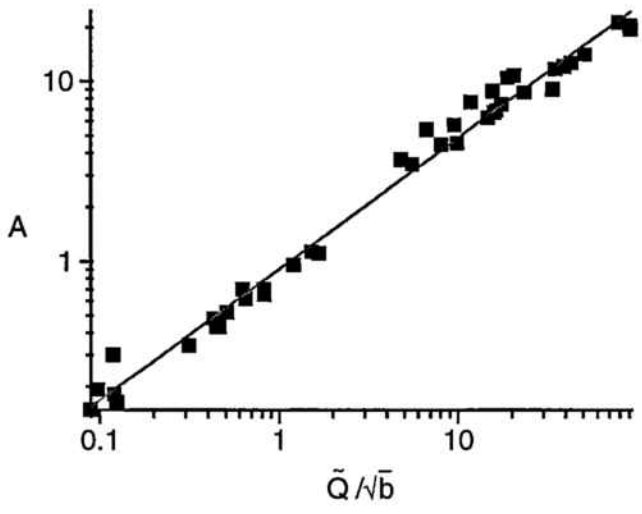

Figure 10: Anisotropic fingering. A vs $\tilde{Q}/\sqrt{b}$ for $b = 0.11$ mm, $b = 0.22$ mm and $b = 0.37$ mm combined.

analysis we see (Figure 10) how in the range of b we used (from 0.11 mm up to 0.37 mm) the final result is not very different from that in Figure 9, even though we believe this last expression allows us to more confidently compare results obtained with different cell gaps.

3.3 Summary and future work

We have performed radial viscous fingering experiments in the presence of anisotropy introduced in the form of geometrical perturbations of the cell gap. We have observed the different morphologies that can be obtained in the presence of anisotropy and have seen the basic qualitative features of these morphologies to be consistent with results from other experiments in the literature. The main objective of our work, however, has been to look for quantitative signatures of the effects of the anisotropy on the fingering patterns. Our experiments exhibit an asymptotic scaling of the tip position of a growing dendrite in viscous fingering in the presence of anisotropy, which has been modeled in the literature [49]. We have observed this scaling in both surface-tension-controlled and kinetic-controlled-dendrites. Our analysis has independently extracted three parameters from our experimental data: A, the prefactor in the scaling of the tip position; $\tilde{Q}$, the rate of growth of the area of the dendrite branch; and α, the time

exponent of the dendrite tip growth. While the theoretical results predict a single value of $\alpha = 0.6$ for surface tension controlled dendrites, in the presence of static anisotropy, and our individual measurements are frequently compatible with this value, we observe significant dispersion among the exponents observed in repeated flow realizations, yielding an averaged value of $\bar{\alpha} = 0.64 \pm 0.09$. For kinetic dendrites, $\bar{\alpha} = 0.66 \pm 0.09$. When we restrict our analysis to the flow realizations where $\alpha = 0.6$ ($\bar{\alpha} = 0.61 \pm 0.03$), we experimentally recover the relationship between A and $\tilde{Q}$ that the scaling of the tip position would impose (equations 3.10, 3.11). Since A and $\tilde{Q}$ are two experimentally independent parameters, verifying those relationships experimentally is a strong self consistency test for the tip-scaling assumptions [49]. Thus far, the relatively large dispersion of α under conditions where the pattern was of unambiguous morphology has prevented us from meaningful comment on the quantification of the data in the morphology transition zones. However, the analysis described in this chapter indicates a way of analyzing quantitatively the effect of anisotropy on viscous fingering patterns, thus extending the mostly qualitative analysis found in the literature.

The observations made in these experiments suggest a way of studying the effect of noise in pattern formation, from a quantitative viewpoint. Earlier attemps at studying the effect of static multiplicative noise in viscous fingering experiments using a radial cell [53] showed a dramatic effect of noisy perturbations on the flow. In those experiments, we forced the radial flow over a lattice etched in a pseudorandom fashion. Even with modests amounts of noise, the effects on the patterns were dramatic, and it was not possible to find meaningful trends.

By means of the analysis we have developed here, one would like to study how static noise destroys the effect of the regular anisotropy. Superimposing random spatial noise at the top of a regular etched plate might present a transition from the observations reported here (perfect anisotropic flow), when no noise is present, to the high noise situation when viscous fingering patterns have been reported to have DLA-like morphologies [45].

Preliminary results show that even modests amounts of noise have strong effects on the patterns. On Figure 11 we compare two dendritic branches obtained under the same conditions, and which have the same rate of growth, $\tilde{Q} = 6.4$ cm^2/s. The only difference is that, while the branch at the top has been generated in flow over

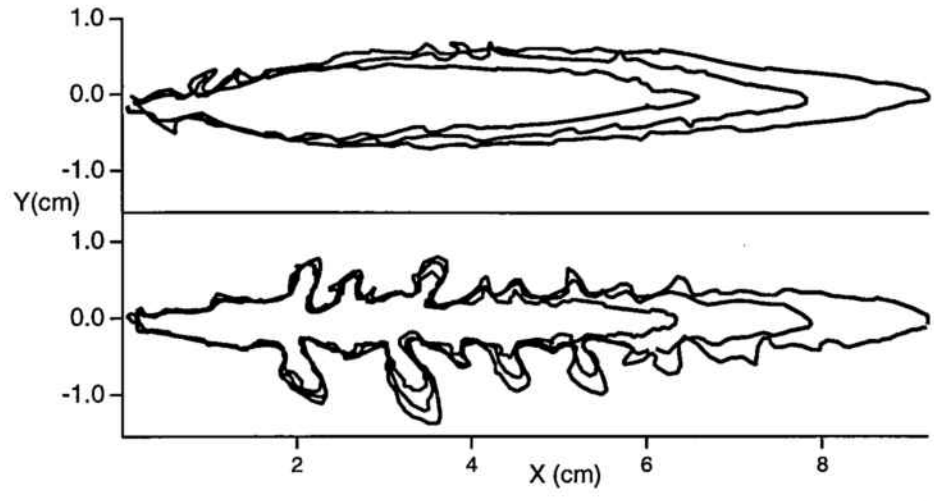

Figure 11: Effect of static noise on the regular lattice. Top: dendrite obtained on a noise-free lattice. Bottom: dendrite obtained on a lattice with 5% noise.

a perfectly regular rectangular lattice of grooves, the one below has been generated in flow over a rectangular lattice whose channels have been randomly blocked on 5% of their surface. The flow has been performed using the same experimental setup described in the previous sections, with a cell gap of $b = 0.22$ mm. We can see how this amount of noise deforms the otherwise sharp needle dendrite, favoring the growth of sidebranches. If we try to look for the validity of the tip scaling assumption discussed in this chapter, we see that the presence of noise gradually destroys that scaling. It would be interesting to perform an analysis similar to the one reported in this work, using lattices with an increasingly high amount of noise, and study the effect this has on the dendritic morphologies.

CHAPTER 4

Fracture of Soft Condensed Matter

The use of non-Newtonian fluids in pattern formation experiments generates a broad variety of morphologies not present in flow with Newtonian fluids. In particular, the rheological properties of some materials lead to a dynamic regime where we can see the fluid behave in a way not unlike a brittle solid. We have studied the behavior of these fluids by performing viscous fingering experiments in a Hele-Shaw channel where the typical time scales (of the order of a few tenths of a second) present simpler experimental conditions that in the study of solid fracture.

In a previous study of radial viscous fingering patterns in Hele-Shaw cells filled with viscoelastic aqueous solutions of end-capped associative polymer, we observed a transition from viscous fingering to fracturelike behavior [38] (see Figure 12, where Figure 12.A corresponds to a run with linear end-capped associative polymers with $M_w = 50\,700$, $c = 2.5\%$, $b = 0.4$ mm, $Q = 5.0$ ml/min; and Figure 12.B corresponds to a run with the same polymer solution, $b = 0.4$ mm, $Q = 1.0$ ml/min. See below for more details on these polymers). The fracturelike behavior was easy to distinguish from viscous fingering when the full time series of patterns was observed because the large angle branches, which were obvious in any one stage of development of the pattern, could be observed to grow from a main branch at very large distances behind the propagating crack tip, a clear departure from viscous fingering where the side-branches, which have generally much smaller angles, always result from tip-splitting. Similar results are observed in experiments of flow in clay suspensions [31–33, 37]. Radial flow in Newtonian fluids is characterized by asymptotic behavior with continuous tip-splitting with a decreasing tip velocity. We come back to the channel geometry to study viscoelastic materials because, in this system, the basic flow (Newtonian fluids) has a steady state characterized by a constant tip velocity. Departures from this simple behavior will be the signature of the effect of the non-

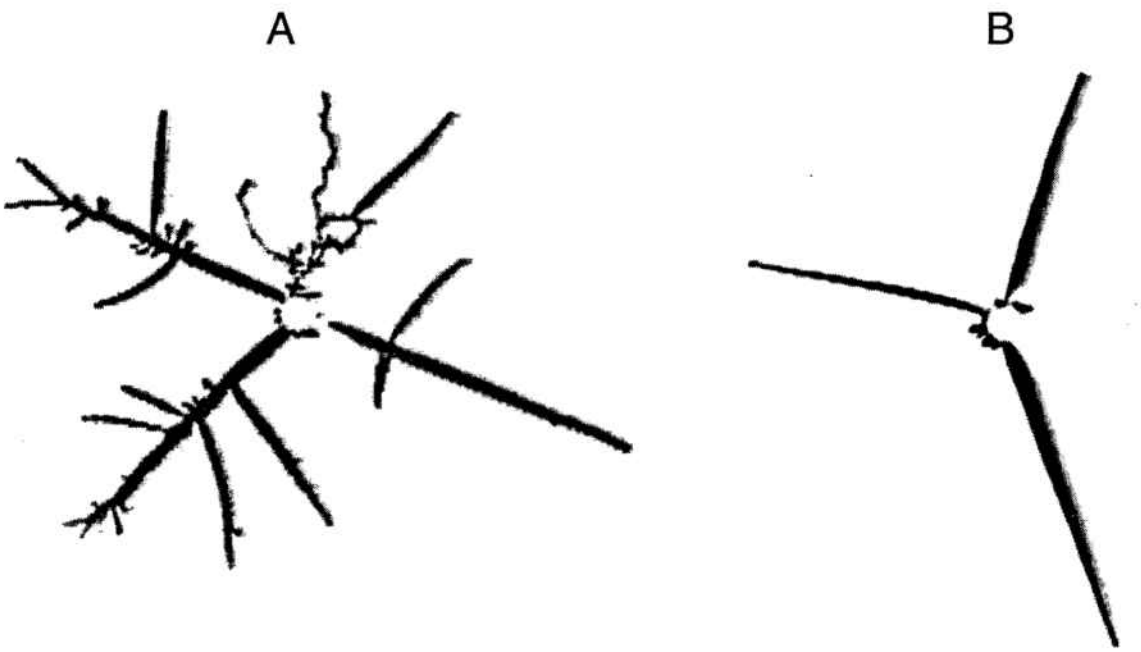

Figure 12: Examples of fracturelike patterns in radial viscous fingering.

Newtonian fluid.

In analogy to the measurements of Fineberg *et al.* for fracture in brittle solids [54, 55], the study of the tip velocity evolution and, particularly, its departure from the constant velocity in the fingering regime should give us some insight into the dynamics of this transition into fracturelike behavior.

In the remainder of this chapter, we give a brief description of the experimental apparatus and present the relevant rheological properties of the associative polymers we have used in the current work. The different morphologies and dynamical regimes we have been able to observe are presented, from a qualitative point of view. In chapter 5, we present the results of our attempts at rescaling the onset of the fracturelike instability in the viscoelastic flow. In chapter 6, we describe our analysis of the dynamics after the fracturelike instability, and present a very interesting oscillating regime with a frequency that changes very consistently with the different control parameters. We also discuss the resemblance of some flow realizations to fracture in brittle materials and compare the dynamics in the oscillating regime with systems governed by stick-slip dynamics. Finally, chapter 7 addresses some unresolved issues from the previous chapters by analyzing the stress in the viscoelastic flow. We show how, despite not being able to directly monitor that stress, we obtain very consistent results that may lead to a better understanding of these phenomena.

4.1 Associative Polymer Networks.

The model associative polymers we use in this work (see Figure 13) are amphiphilic molecules consisting of a linear hydrophilic backbone (based on Poly Ethylene Glycol (*PEG*) with *DI* being isophorone diisocyanate) with hydrophobic groups placed at different locations in the molecule [56, 57]. We have used two basic architectures (see Figure 13): linear end-capped associative polymers, where the linear backbone is terminated at both ends by hydrophobic end groups (**R**); and comb associative polymers, where hydrophobic groups (**R**) stick out from the backbone at regular intervals, forming a comb-shaped molecule. Once in aqueous solution, the hydrophobic groups will try to minimize contact with the solvent by forming associative nodes with hydrophobic groups from different polymer strands, with multiple possible associations (see Figure 14), forming a so-called associative network.

The polymer solution is a non-Newtonian fluid, thus normal stress differences, yield stress, shear thinning, stress relaxation, etc., need to be taken into account in any description of the dynamics.

It turns out that no yield stress is measured for these fluids. This suggests that the network bonds are not rigid but, in fact, recombining dynamically. The associative network gives most interesting rheological properties to these materials [56] (some of these properties are absent in *PEG* homopolymers of similar molecular weight, which generate very different results under similar experimental conditions [38]). For instance, the zero shear viscosity of a given concentration of these polymers in water can be orders of magnitude larger than that of the corresponding hydrophilic homopolymers, where chain entanglement is the main mechanism responsible for the viscoelasticity. Measurements of the viscosity as it changes with shear rate show that these associative polymer solutions are shear-thinning beyond a characteristic shear-thinning shear-rate, $\dot{\gamma}_0$, which depends on polymer architecture and on concentration of the solution. Sometimes, the shear-thinning regime is preceded by a shear thickening regime (see Figure 15 for the shear viscosity measurements on the high molecular weight linear end-capped associative polymer, as reported in [56]). From the available rheology data, we can extract the zero-shear viscosity, μ_0, the shear-thinning shear-rate, $\dot{\gamma}_0$, and, from the oscillatory stress measurements on the solutions, the frequency at which the storage modulus and the loss modulus take on the same value, ω_0. The latter rheological parameter has a more clear definition

Linear Endcapped	R–O–[–DI—PEG–]$_Y$–DI–O–R
Comb	[[–DI–]$_W$–[–PEG—DI–]$_Y$]$_{Z-1}$ (R, R) –[–PEG—DI–]$_Y$

Figure 13: Structure of the model associative polymers. **R** are hydrophobic groups. **DI-PEG** form the hydrophilic backbone.

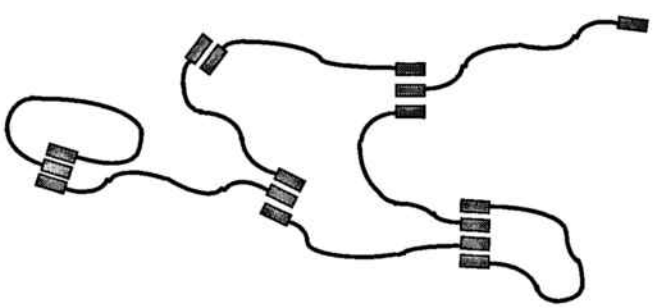

Figure 14: Formation of the Associative Network of polymers in the linear endcapped case. Hydrophobic groups try to minimize the contact with water.

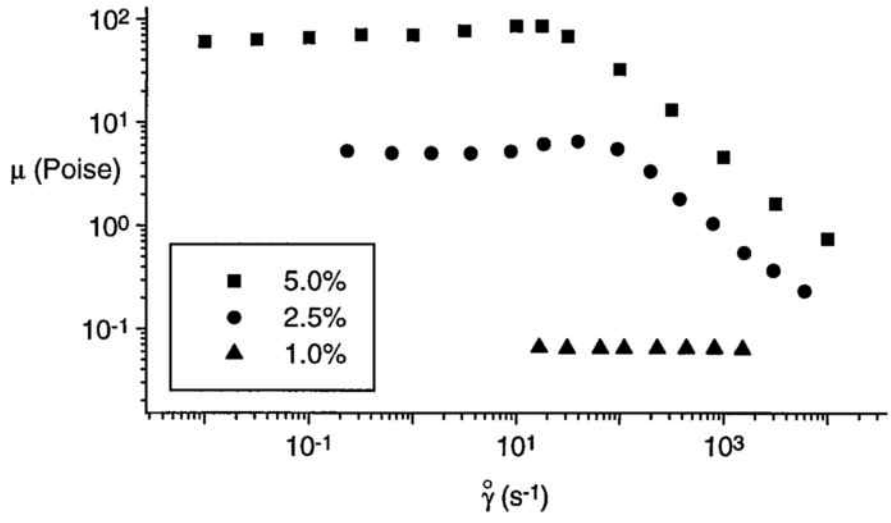

Figure 15: Shear viscosity vs. shear rate for the 100 400 molecular weight linear endcapped associative polymer at different concentrations in water as measured by R. D. Jenkins [53].

than the former. $\dot{\gamma}_0$ is somewhat arbitrarily chosen from the measured shear-rate dependence of the solution viscosities. The criterion we used was assigning $\dot{\gamma}_0$ to the shear rate where the shear viscosity goes below the zero shear value.

Since, when available, the rheological data are limited to a small number of concentrations, we have used extrapolation of the different parameters mentioned above assuming a power law dependence with concentration of the polymer in solution, which is a commonly found behavior in these materials. In Figure 16 we can see an illustration of this dependence. The points are the data, and the line is a power law fit to that data, that we have used to extrapolate the rheology parameters to other concentrations. The top of that figure corresponds to rheology data for the 100 400 molecular weight linear end-capped associative polymer, for which we find the empirical relations $\dot{\gamma}_0 \sim c^{-1.7}$, $\mu_0 \sim c^{4.3}$, and the bottom of the figure corresponds to the 53 300 molecular weight comb associative polymer, for which we find $\dot{\gamma}_0 \sim c^{-7}$, $\mu_0 \sim c^{6.2}$. The square symbols correspond to the shear thinning shear rate, and the circular symbols correspond to the zero-shear viscosity. The extrapolation certainly introduces extra uncertainty in the shear-thinning shear rates, but it is probably a good estimate of this rheological property, for a narrow range of concentrations.

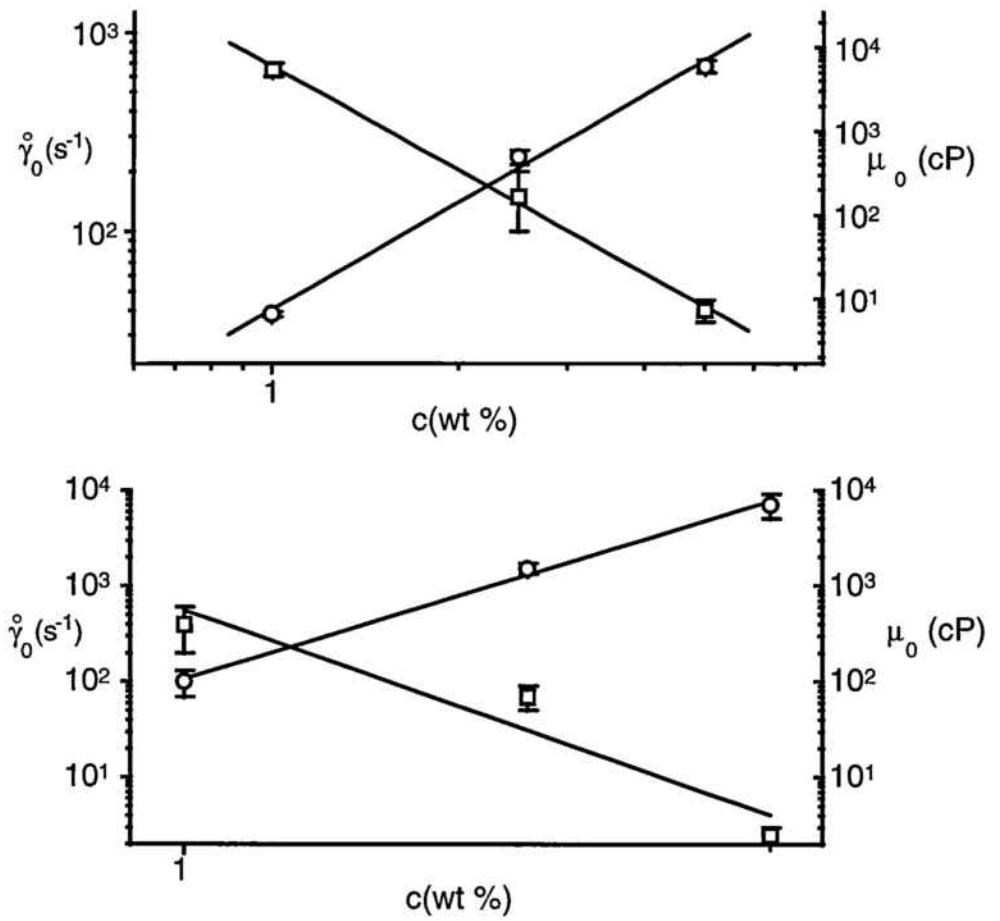

Figure 16: Shear thinning shear-rate (□) and zero-shear viscosity (○) for linear end-capped (top) and for comb (bottom) associative polymers. The symbols are the measured data [53, 58] and the solid lines are power law fits, that we use for the extrapolation at different concentrations.

4.2 Experimental procedure

We used a Hele-Shaw cell with a channel of length 22 cm with Teflon spacers which both set the side wall spacing at values between 1.0 and 2.0 cm and determined the gap between the cell plates (see Figure 1). Gaps were studied in the range 0.05 cm to 0.16 cm. The glass plates of the cell were 1/4 inch thick, and calculated maximum flexion [18] was in no case greater than 0.5% of the gap. We ran the flows at constant and controlled volumetric injection rate, Q, by injecting dyed water with a syringe pump [58] over a range from 0.5 ml/min to about 10 ml/min ($\pm 10\%$). Resulting patterns were observed with a CCD video camera [59] and recorded on an enhanced S-VHS video cassette recorder [42]. Subsequent digital analysis was performed with the assistance of image-processing software [43]. In addition to analyzing the shapes of patterns, the recorded time series could be digitized to give tip positions at 1/30 s intervals, as the tip of the pattern progressed through the cell. From the time series, velocities averaged over 1/30 s intervals could be constructed (electronic shutter speeds of 1/2000 s were used to sharpen images and define temporal averaging intervals).

We also used a modified apparatus where we monitored the pressure of the invading fluid (water) at the injection point, with the help of solid state pressure transducers [60] which convert pressure to a measurable voltage. We had three different transducers, with different full scale pressure: 1 Psi, 5 Psi and 15 Psi (1 Psi = 7.09 10^4 dyn cm^{-2}). Depending on the pressure range that we expected to reach in a given flow realization we used the transducer that optimized the reading. We were able to monitor this pressure at a rate of 15 readings per second (limited by the speed of the voltage meter). It was important that we synchronized the pressure readings with the video frames in the VCR. This way we could obtain a time series of the tip velocity, the area of the growing pattern and the injection pressure. Only with the measurements of comb associative polymers did we monitor the pressure.

As noted above, we have used aqueous solutions of two different architectures of model associative polymers: linear associative polymers and comb associative polymers. We used linear associative polymers with molecular weights 17 400, 50 700 and 100 400 (as calculated from reaction stoichiometry [56]). Different molecular weights differ only in the size of the backbone (index **Y** in Figure 13). The comb associative polymers had a number averaged molecular weight (also calculated from reaction

stoichiometry [61]) of 53 300, 106 800 and 160 300. Different molecular weights differ only in the index **Z** in Figure 13. We prepared solutions with concentrations in the range 0.1% up to 8.0% in weight. We had observed earlier that the associative process starts taking place at very low concentrations. In preparing the solutions, we were careful not to disturb the forming network. The dissolving polymer was not stirred, and it was stored at cold temperatures ($\sim 4°$C) to prevent degradation of the backbones. Also, we added a small amount (a few parts per million) of hydroquinone, which is an inhibitor of the chemical degradation of the PEG backbones. As a test, we monitored the shear viscosity of the solutions over the period of measurements. We discarded data when the shear viscosity had dropped noticeably. It is a generalized trend for these solutions to degrade over time. But keeping them at low temperatures and using the chemical inhibitor preserves them long enough (several days, or even weeks) without much degradation to allow the experiment to be performed.

4.3 Qualitative results. Different patterns and transitions

When we injected the dyed water at a low enough injection rate into any of our polymer solutions, we were able to obtain a steady-state Saffman-Taylor finger. This was true for all the linear end-capped polymers, but it was not true for the two larger molecular weights of the comb polymers. Even at the lowest possible concentrations, we were not able to observe viscous flow with those polymers (the water being injected was not able to penetrate the solution and was forming a very disordered pattern in the region adjacent to one of the glass plates).

As the injection rate increased, the viscous fingers became unstable, and regimes with different morphologies and different dynamical features were found. At early times, a viscous finger grew. The width and the tip curvature of this pattern always conformed to the relation expected for a Saffman-Taylor finger in the absence of surface tension (see eq. 1.21) even though there is no reason to believe that this solution (or the solution that includes surface tension effects) must survive the use of a viscoelastic material. In Figure 17, the solid lines are a fit to the parabolic shape of a Saffman-Taylor finger, and the circles are the digitized contour of a growing finger.

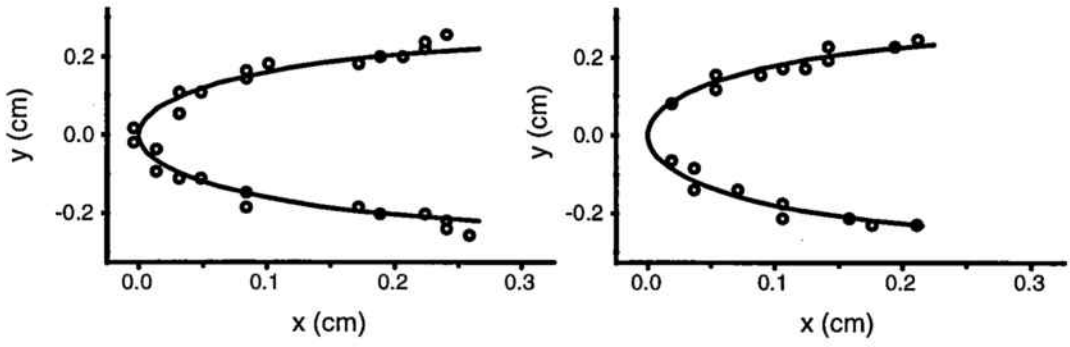

Figure 17: The shape of two viscous fingers obtained with flow in associative polymer solutions. Left: $\lambda = 0.54$. Right: $\lambda = 0.50$. The data (◯) are compared with the theoretical expectation (solid curves).

If we consider the shape of a finger, whose tip is at (0,0), to be

$$x = \frac{1}{a}y^2 \tag{4.1}$$

then, from eq. (1.21) we get, by approximating the exact tip-shape to a parabola,

$$\frac{2}{a} = \frac{\pi W(1-\lambda)}{(\lambda W)^2}. \tag{4.2}$$

From the fit of the tip shape to a parabola, we extracted a value for λ which matched the width of the finger, experimentally measured.

Even though the fluids are miscible, such systems are known to have an effective surface tension and, if this is large enough, it might be expected to make the finger width follow the Saffman-Taylor width as a function of the inverse capillary number [62]. However, our fingers always had a width very close to half the channel, suggesting a sufficiently small dynamic surface tension that our effective inverse capillary number was always large enough to give this width. We would need extremely low velocities to be able to see much wider fingers (i.e., to make $1/B$ small enough since, from eq. 1.23, $1/B$ increases with V and the measured relation between λ and $1/B$ [17] shows that λ decreases towards a plateau value when $1/B$ increases).

In Figure 18 we can see the three possible flow realizations we found in the experiments: The top series (labeled a1, a2) corresponds to a typical flow with the two lower molecular weights of the linear end-capped associative polymer, with Q above a threshold, Q_{th}. The flow starts with a viscous finger whose shape is that

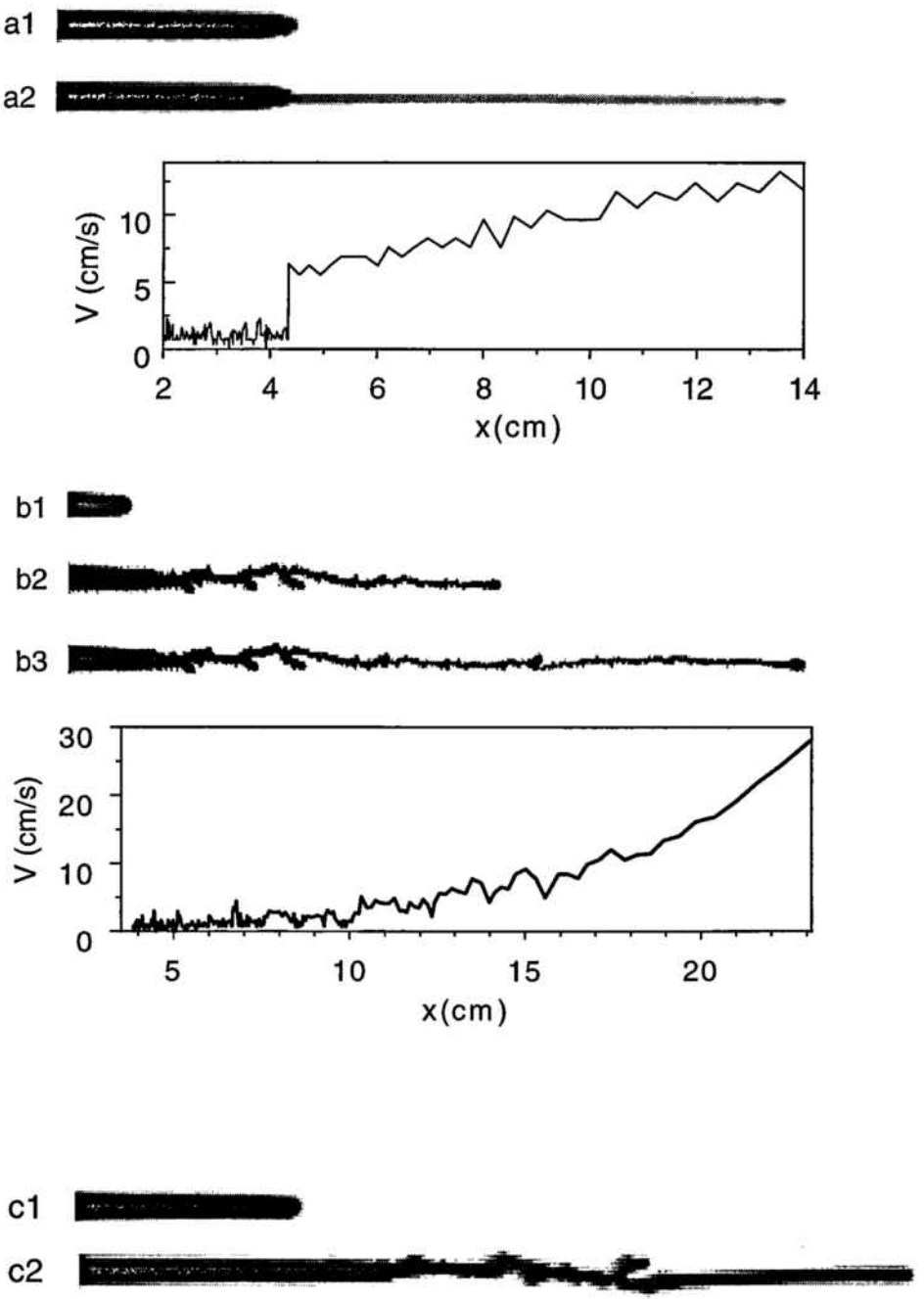

Figure 18: Different morphologies in the flow in associative polymer solutions. Top series: flow in lower Mw linear endcapped; middle series: flow in highest Mw linear endcapped; bottom series: flow in lowest Mw comb associative polymer solutions.

of a Saffman-Taylor finger (a1). This regime, however, becomes unstable, and the morphology and the dynamics of the growth change abruptly (a2), with a narrow, fracturelike pattern that grows along the center of the channel, near the center of the gap space and much thinner across the cell gap than the parent finger, which we can note because of the lighter color of the fracture. We have measured it (comparing the rate of growth of the area with the known volumetric injection rate, see section 6.1) to fill about one-sixth of the gap thickness occupied by the previous viscous finger. We can observe the evolution of the tip velocity in the graph below the pictures. We see how, in the fingering regime, the velocity fluctuates about a constant, small rms value. However, when the transition occurs, a sudden jump (faster than 1/30 s) occurs, and the velocity has a gentler, almost linear increase in its rms value during the subsequent regime, which resembles the dynamics of fracture in brittle materials [54, 55]. This fracturelike pattern typically progresses at sufficiently high speeds that not many independent measurements of velocity are possible before the tip reaches the end of the cell.

The middle series (labeled b1, b2, b3) corresponds to a typical flow with the highest molecular weight of the linear end-capped associative polymer, with $Q > Q_{th}$. Again, the flow starts with a viscous finger (b1) where the tip velocity oscillates around a small value, and its shape conforms with that of a Saffman-Taylor finger. This regime becomes unstable, and the pattern that emerges (b2) is characterized by its meandering along the channel, with an unsteady tip velocity (large amplitude oscillations). This regime becomes eventually unstable, and a third regime sets in (b3) characterized by a fast increase of the tip velocity, straight along the channel. Notice that all the interesting dynamics takes place in a small region around the tip of the growing patterns, as the pattern that is left behind shows no evolution with time (compare b2 with the later pattern b3). In fact, even though we talk about a fracturelike transition when we refer to the third regime (b3), its morphology is different from the observations in radial geometry, in that we do not see any sidebranching, but that is possibly an effect of the sidewalls in the channel.

Finally, the last series in that figure (c1, c2) corresponds to a flow using the low molecular weight comb associative polymer. The flow starts with a fingering regime (c1) which becomes unstable; a regime similar to the meandering regime described above follows (c2), displaying large oscillations in the tip velocity; and, finally, a regime similar to (a2) may develop as the oscillating regime becomes unstable at

later times. The velocity profile (not shown in the figure) exhibits a behavior similar to the middle series, except for the final fast fracture regime, where a straight branch appears, acompained by a sudden increase in the tip velocity, in much the same way as was observed in (a2).

CHAPTER 5

Fracturelike Instability of the Fingering Regime

As we saw in the previous chapter, different morphologies are observed when we perform viscous fingering using associative polymer solutions. In particular, (see Figure 18) a fingering regime can be made unstable by injecting water beyond a certain driving force, and a pattern that resembles the fracture of brittle materials develops. There is a transition, from the polymer solution flowing like a viscous fluid into a solid-like behavior. One might try to explain this as follows: for small injection rates, the energy introduced externally, at a slow rate, can be efficiently dissipated by the viscous flow. However, at high imposed flow rates, the polymeric liquid cannot dissipate energy at the required rate, and another, presumably more efficient, mechanism is chosen: fracture of the medium. Using these observations, in a previous experiment with associative polymers in radial Hele-Shaw flow [38], the transition from Viscous Fingering to fracturelike behavior was rescaled by a suitable definition of a Deborah number [63]. The Deborah number is defined as the ratio between a *time of relaxation* and an *inverse applied shear*. The time of relaxation is a characteristic time of the medium under study. The general idea behind the Deborah number in rheology is that its magnitude informs of how much will a medium behave as a solid or as a fluid. Large values of De correspond to the medium behaving in a solidlike fashion. Small values of De suggest a fluidlike behavior of the medium.

In the previous study of radial viscous fingering [38], a Deborah number was defined as the ratio of the polymer network relaxation time (taken to be the inverse shear-thinning shear rate) to the inverse external shear rate (or characteristic time related to the viscous flow), that is,

$$De = \frac{\tau_r}{\tau_f}, \quad \tau_f \sim \frac{b^2}{Q}, \quad \tau_r = \frac{1}{\dot{\gamma}_0}, \tag{5.1}$$

where τ_f would also contain a characteristic length of the radial cell, which is irrelevant if the same cell is used in all the experiments. It was observed that the transition to fracturelike behavior appeared at roughly the same Deborah number under variations in the rheological properties (polymer molecular weight or concentration in solution) or changes in the cell geometry (variations in the cell gap).

5.1 Scaling of the instability

From the Hele-Shaw channel experiments, we can extract, as a characteristic time for the externally imposed flow

$$\tau_f \sim \frac{Wb^2}{Q}, \tag{5.2}$$

which is the inverse of the characteristic shear rate due to that flow. (If the characteristic velocity is $U = Q/(bW)$, then the shear rate is $\dot{\gamma} = (dU)/(dz) \sim U/b$, since the velocity has a change of order U over a length of order b). Using

$$\tau_r \sim \frac{1}{\dot{\gamma}_0}, \tag{5.3}$$

we obtain a Deborah number

$$De = \frac{Q}{\dot{\gamma}_0 W b^2}. \tag{5.4}$$

Here, W should be the width of the Hele-Shaw channel, from the definition of τ_f. However, in the experimental computation of De presented below, we have found a better result if we use the actual width of the finger, w, rather than the full channel width. Even though $\lambda \sim 0.5$ in most flow realizations (see section 4.3), using w gives a better scale for τ_f and for De.

When we used the same polymers that were studied in the radial geometry (linear endcapped with molecular weights 17 400 and 50 700), the transition from viscous fingering to a propagating crack tip was successfully rescaled with the above defined Deborah number. That is, transitions occurred at roughly the same Deborah number for different rheological properties of the material and for changes in the cell dimensions. As we saw in section 4.3, the transition from viscous fingering into fracturelike behavior was very sharp in these two cases. We wanted to compare the results obtained in the current experiments with what was observed in the radial case. We

found that the transition Deborah numbers for each geometry could be brought into agreement by an arbitrary factor of 4.0, which is justifiable since different scale factors are omitted in the definitions of τ_f for each geometry.

Figure 19 presents the range of Deborah number within which the fracturelike instability appears for different combinations of polymer molecular weight, polymer concentration, cell-gap, and channel width. For a given cell geometry and using a given polymer solution, we perform a series of experiments, spanning the injection rate over a range that includes the transition point. We have observed that this transition point does not correspond to a very sharply defined injection rate (Q_{th}) but rather, all we can do is give an upper and lower bound to the region where we observe the transition to occur (the error bars in Figure 19 are, then, the meaningful information since they inform of the range where the transition occurs during many flow realizations).

The fact that this transition has a wide range of onset points may suggest it is related to a supercritical bifurcation that the system is undergoing, so that the flow may enter a regime where it is unstable to finite size perturbations. In a supercritical bifurcation, a critical value for the control parameter is reached where a previously stable dynamical regime becomes unstable, and new stable solutions exist when the control parameter is above that threshold. Even though the previously stable solution is now unstable, the old dynamical regime may still be dominating the system in a metastable fashion, maybe requiring a finite size perturbation to enter one of the new stable dynamical regimes.

Figure 19.a corresponds to experiments using the two lower molecular weight endcapped associative polymers. The triangles correspond to experiments in the channel geometry and the circles correspond to experiments in the radial geometry. As explained above, the error bars exhibit the range in which the transition appears after many flow realizations. The two sets of data have been brought into agreement by an arbitrary factor of 4.0, as explained above. We can see how all the transitions occur in overlapping ranges of De.

Figure 19.b corresponds to experiments using the 100 400 molecular weight endcapped associative polymer. Here the transition happens much earlier (at much lower De) than in the other case. We observe in our experiments (see Figure 18) that the instability of the fingering regime takes place in a different way for this molecular

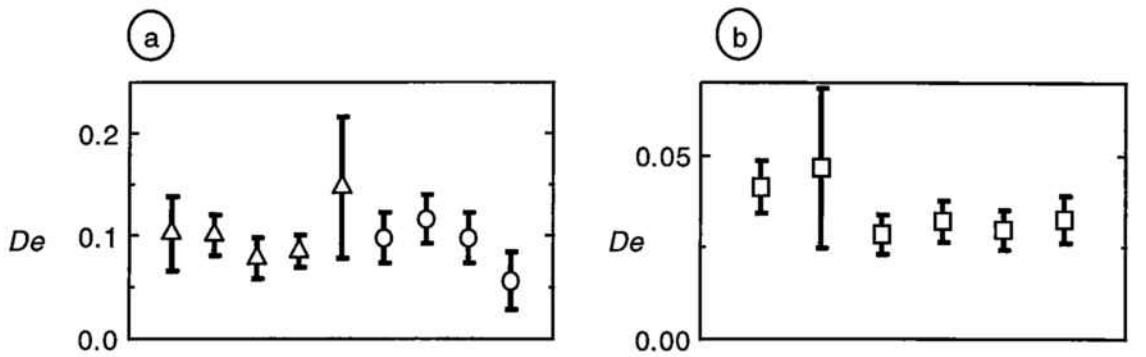

Figure 19: Range of Deborah number at which transitions are observed to occur for experiments with the lower (left) and the highest (right) molecular weights linear endcapped associative polymers. On the left, △ corresponds to channel experiments and ○ to radial experiments.

weight. There is a meandering regime that is not present in the two lower molecular weights. However, at high injection rates and at later times, this meandering phase can turn into a fracture pattern as defined for the two lower molecular weights. It is difficult to define the exact point of onset of the fracturelike behavior in the presence of this meandering phase, but it is always possible to find a point in the evolution within the meandering regime where the tip velocity has reached a value which gives a Deborah number in agreement with the one expected for the fracture transition from the lower molecular weights. Even though the transition between the meandering regime and the fast fracture regime is not clear at all, it is never far from this point at which the Deborah number expected from the low molecular weight results is reached.

We also explored the use of an alternative characteristic time scale for the polymer network, namely, the inverse of the excitation frequency at which the elastic moduli of the material (the Storage modulus and the Loss modulus) take on the same value, ω_T. This seemed a better approach given the nature of the dynamics we observed but, as it happened in earlier experiments [38], using $\dot{\gamma}_0$ gave consistently better results.

We can also observe a clear threshold injection rate, Q_{th}, for experiments using the lowest molecular weight comb associative polymers. We can see, in Figure 20, that the dependence of Q_{th} vs. concentration closely follows a power law. This a typical behavior for rheological properties of these materials. The solid line is a power law fit, giving $Q_{th} \sim c^{-2.9}$. The available rheological data for these polymer solutions

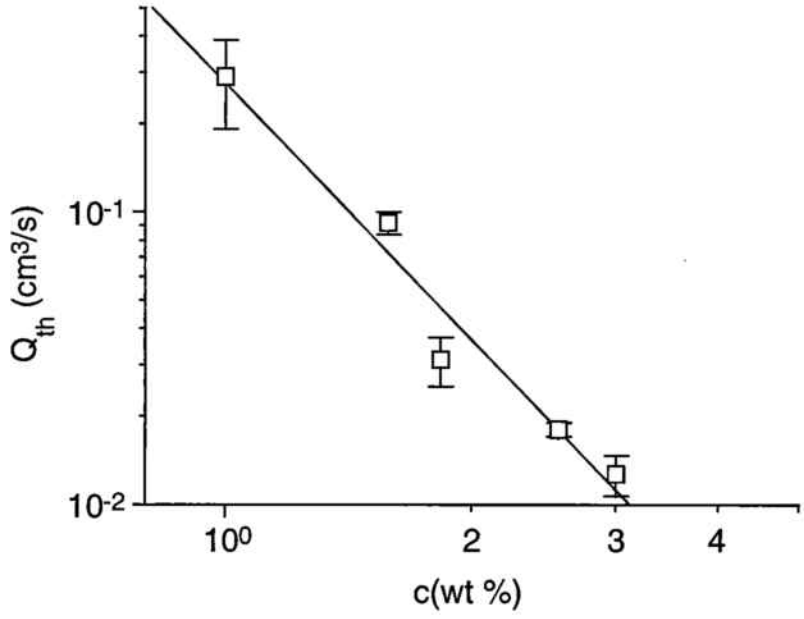

Figure 20: Threshold injection rate for comb associative polymer solutions. The threshold ranges seem to follow a power law dependence on concentration

(see Figure 16) show a shear thinning shear rate that can be reasonably described with a power law $\dot{\gamma}_0 \sim c^{-7}$. Earlier attempts with the comb associative polymers in the radial geometry [38] obtained values for the Deborah number at the transition that were more than one order of magnitude off what the other experiments (with linear endcapped associative polymers) were giving. In the current experiments, using the definition of De (eq. 5.1) would yield $De \sim c^{-4.1}$, which changes with the concentration and, thus, fails to rescale the onset of the instability (Q_{th}). The fact that $Q_{th} \sim c^{-2.9}$ suggests that there may well be a rheological parameter (perhaps related to $\dot{\gamma}_0$) that would allow us to rescale these threshold values, just as we did for the linear endcapped. However, given our current rheology data, $\dot{\gamma}_0$ is not a good choice, since the power law dependences of Q_{th} and $\dot{\gamma}_0$ on c have different exponents.

We have seen how analyzing the onset of the instability that leads to the fracture-like regime with the help of a single characteristic parameter of the fluid material, namely a characteristic time scale given by the shear thinning shear rate, is able to rescale the onset of that instability across changes in polymer concentration and across changes in polymer molecular weight, when we work with the linear endcapped associative polymers. This simple analysis, based on the definition of a Deborah number (5.1), fails to work when we change the polymer architecture. Our experiments

with comb associative polymers, however, show that there may well be a rheological property of the materials that could rescale the onset of these instabilities also in this second architecture (see Figure 20).

CHAPTER 6

Dynamics after the instability of the Viscous Fingering regime

In the previous two chapters we have described the interesting patterns that grow when Saffman-Taylor fingers, obtained with flow in associative polymer solutions, become unstable. Both the morphologies that result, very different from those obtained in viscous flow of Newtonian fluids, and the dynamics, where the tip velocity exhibits a clear acceleration and, in some cases, a clear unsteady evolution, suggested to us a comparison with fracture in brittle materials [54, 55] and with experiments of peeling of adhesive tapes [64], where stick-slip dynamics plays a major role. In analogy with what was done in those experiments, we measured the evolution of the tip velocity, and we tried to analyze there the signatures of the dynamics.

6.1 Acquisition of the Experimental Data

In a typical experiment, we observed with a CCD camera [59] the top view of the Hele-Shaw channel where the flow took place and taped it on an Enhanced S-VHS recorder [42]. The videotape recorded this way was analyzed with the help of image processing software [43]. We extracted, from each video frame, the position of the tip and the area of the growing pattern. A Video Controller [65] was used as an interface to both keep the time reference of the images and to remotely control the position of the tape in the VCR from the computer. Since the polymer solution was almost transparent, there was a very high contrast with the dark color of the injected dyed water (see Figure 18). We were able to automate the data acquisition process by digitally subtracting a background image from each frame, thus enhancing the contrast. This way, having previously selected a suitable luminance threshold, the

software was able to efficiently trace the contour of the pattern. From the digitized contour points, it was straightforward to find the tip position and the area of the pattern.

In the experiments with the comb associative polymers, we were able to monitor the pressure at the injection point as well. We used pressure transducers [60] which generated an output voltage that changed linearly with pressure. We calibrated these sensors by measuring with them the pressure under a column of water and we found that their accuracy was better that 10%. The output of the transducer was monitored by a computer at a rate of 15 readings per second. We synchronized the pressure readings with the video images simply by recording the image of a light being switched on and, simultaneously, registering the event on the computer that was monitoring the pressure.

We can see on Figure 21 an example of the information extracted from a run using the low molecular weight comb associative polymer (a similar set of data was extracted for the linear endcapped experiments, except from the pressure, which was not monitored in those cases). For this flow realization, the injection rate was $Q = 2.5$ ml/min, and the concentration $c = 2.52\%$. The channel was $W = 1.0$ cm wide and the gap was $b = 0.16$ cm. We recorded the time evolution for the X position (graph a), and for the Y position (graph b) of the tip of the growing pattern. From the time evolution of the tip position, we evaluate the time series for the evolution of the tip velocity, or rather, the tip speed

$$V_i = \sqrt{(\Delta x_i)^2 + (\Delta y_i)^2}/(\Delta t). \tag{6.1}$$

We also recorded the evolution of the area of the pattern (graph c) and the evolution of the pressure at the injection point (graph d). We can see the onset of the meandering regime in the large oscillations of the Y position at later times. In Figure 21, we have marked the onset of the meandering regime (instability of the viscous fingering regime), which takes place at about $t = 31$ s. Before that, the Saffman-Taylor finger had a tip centered along the channel (the channel width is $W = 1$ cm) and there are only fluctuations about that position. When the transition occurs, the tip starts to meander along the channel (we see large fluctuations of the Y component of the tip position). At about $t = 37.5$ s, the meandering regime becomes unstable, and we observe another jump in the tip velocity, with its position centered in the channel.

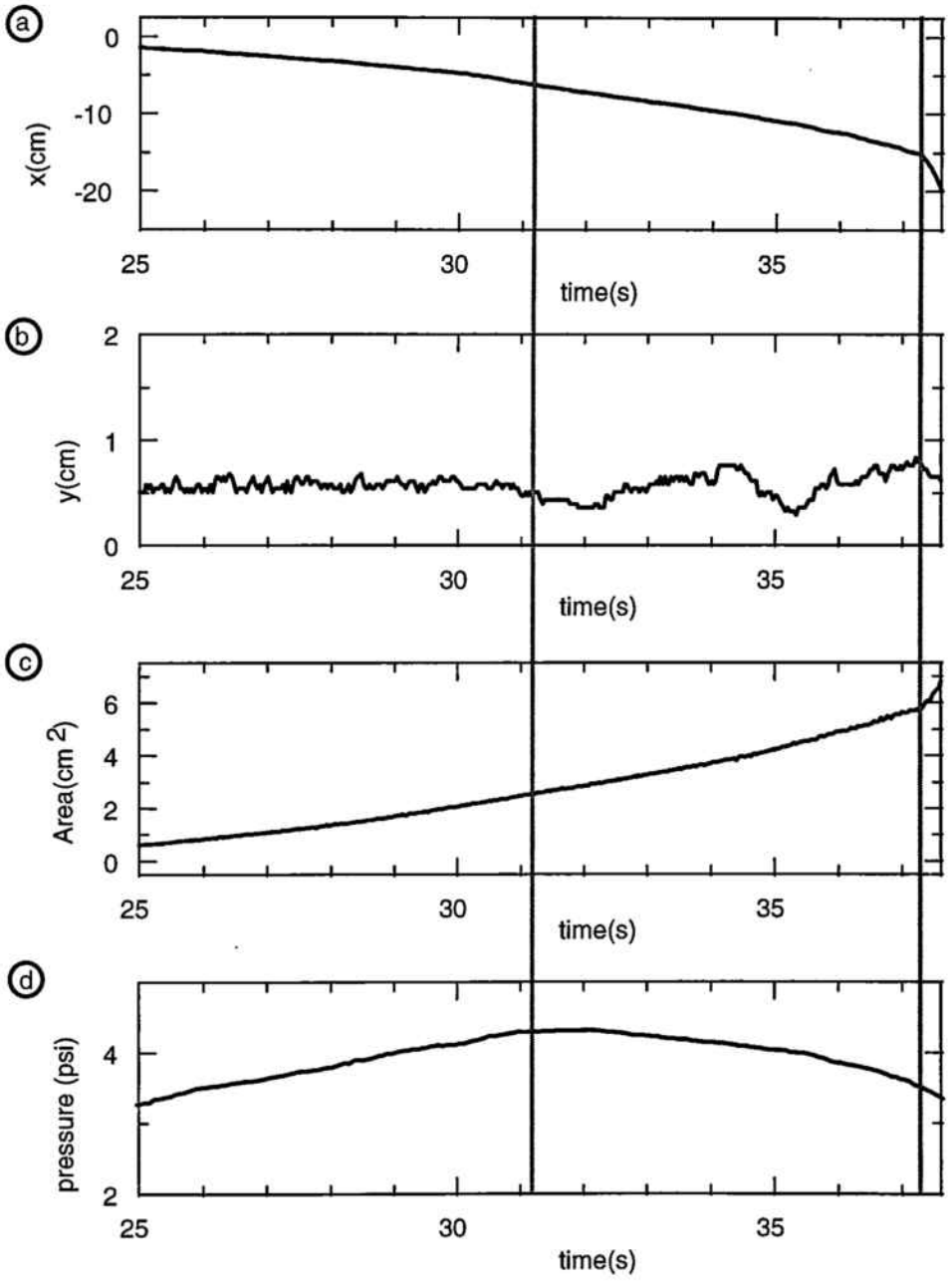

Figure 21: Data obtained from a channel flow realization with comb associative polymer solutions. The onset of the meandering regime ($t \sim 31$ s) and the onset of the fast fracture regime ($t \sim 37.5$ s) are marked.

We also see that the area of the growing pattern (graph c) does not grow linearly with time throughout the run, which would be the case if both the constraint $Q = constant$ held and the thickness of the pattern across the gap was constant. Since we are confident on both the constancy of the injection rate (given by the syringe pump) and on the accuracy of the measurement of the area of the pattern, the only conclusion is that the **thickness** of the pattern across the gap is, in fact, decreasing as the speed of the fracture tip increases. Thus, from these measurements, we can monitor the fraction of the gap space that is actually filled by the invading fluid, b_{eff}. Since the growth of the pattern is concentrated in the tip region, it is a good approximation assuming (see appendix C)

$$Q = b_{eff}\frac{dA}{dt}, \tag{6.2}$$

from where

$$b_{eff} = \frac{Q}{dA/dt}. \tag{6.3}$$

The evolution of the pressure of the invading fluid at the injection point shows an initial increase, possibly showing stress building up in the associative polymer network, up to a maximum value. In this example, we can see that this maximum is reached at about the same time the fingering regime is about to fracture. We looked for correlations of these two events in the different flow realizations, but we have not obtained any conclusive results.

From the evolution of the tip position, we extracted the evolution of the tip velocity, averaged over the 1/30 s interval between frames. Using a fast electronic shutter we were able to obtain very sharp images, with very good spatial resolution. Since, in some flow realizations, we observed interesting unsteady evolution of the tip velocity, we tried to detect characteristic oscillation frequencies in some dynamic regime. For this purpose, we performed Fourier Transforms of the time evolution of the tip velocity. It is usually the case, however, that there is a net acceleration to which an oscillating velocity is superimposed. This causes a jump discontinuity between the velocity in the first time value and the velocity at the last time value of a given time range. This will cause a spreading of the peaks in the power spectrum and will difficult the observation of characteristic frequencies. For this reason, we applied a numerical window to our data. In particular we chose the Hanning window

[66], which optimized the results. Given the time series of a measured quantity, V_i, we apply the numerical window H_i to obtain the filtered time series

$$W_i = V_i H_i, \tag{6.4}$$

for $i = 1 \cdots N$ sampling intervals. In particular the Hanning window has the expression

$$H_i = \frac{1}{2}\left[1 - \cos\left(\frac{2\pi i}{N}\right)\right]. \tag{6.5}$$

This procedure turns the original time series into another one where the jump discontinuity has been removed. It preserves the other interesting features of the original power spectrum, reducing the power spreading due to that jump discontinuity. This way, it sharpens the interesting frequencies in the original evolution. The only side effect is generating a broad peak that fills the first few channels of the power spectrum. Thus, we need a run that lasts long enough to give a power spectrum with a fine frequency resolution so that the artificial peak will not hide interesting low frequency features.

6.2 Analysis of the Experimental Data

We presented in chapter 4 the different morphologies we can observe in our experiments, together with the measured evolution of the tip velocity. Now, we will look at the results of the analysis of these time series.

Figure 22 is a typical example of what we can observe in the evolution of the tip velocity for runs using the lower molecular weight linear end-capped associative polymers (it corresponds to the same run shown on Figure 18.a). This case corresponds to the injection of water at a rate of $Q = 1.2$ ml/min into a $c = 2.6$ % solution of 17 400 molecular weight linear endcapped associative polymer, in a Hele-Shaw channel of gap $b = 0.12$ cm and width $W = 1.0$ cm. We see at the top in Figure 22 the time evolution of the tip velocity. In the fingering regime ($0 \text{ s} < t < 4 \text{ s}$), the velocity fluctuates about a constant, steady state value. We can see that these fluctuations are mostly high frequency noise. The inset in that figure corresponds to the same velocity evolution after a low-pass filter is applied. This filter removes the high frequency fluctuations and we have generated it by replacing each data point with the average

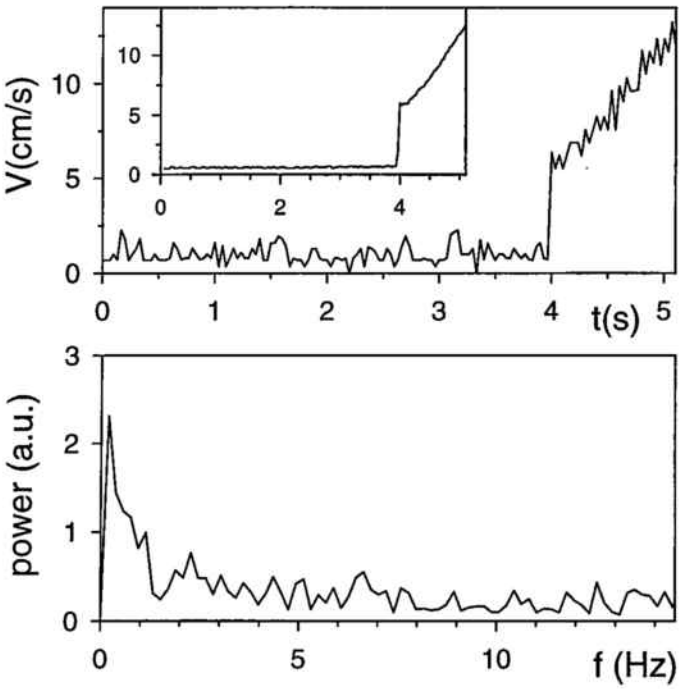

Figure 22: Time evolution and frequency spectrum of the velocity profile in a low molecular weight linear endcapped associative polymer fracture.

of its neighbors. Note the sharp transition in tip velocity from the viscous fingering regime into the fracturelike regime. This increase takes less that 1/30-s of duration (our time resolution). After the transition, there are small fluctuations superimposed on a dominant acceleration of the tip. At the bottom of that graph we have the frequency spectrum for the same velocity distribution. This Fourier spectrum shows no trend that is reproducible (not surprising considering the severe limitations in the finite range of data).

The behavior of these lower molecular weight associative polymer solutions is very reminiscent of the brittle-solid fracture results of Fineberg *et al.* [54, 55]. As in that work, we observe a sudden increase in velocity at the onset of fracture-like behavior, followed by small fluctuations superimposed on a rather constant value of $\Delta V/\Delta x$ at later stages of the crack propagation. Fineberg *et al.* have measured the jump of velocity at onset to be continuous in Δx, with a mean value of $\Delta V/\Delta x$ that we have determined (from their published data) to be about 30 times higher than $\Delta V/\Delta x$ in the subsequent regime. The jump we observe occurs in one time step. If we assume our observed jumps to occur linearly throughout the one averaging interval, Δx, we estimate, for the example shown in Figure 18.a, that $\Delta V/\Delta x$ at the onset of fracture is of the order of 30 times that of $\Delta V/\Delta x$ in the subsequent regime. This is very

consistent with the results of Fineberg *et al.*, but we cannot compare time scales directly since we cannot confidently define a dimensionless time. However, Fineberg *et al.* report a third crack propagation stage characterized by a still lower value of $\Delta V/\Delta x$, and this, we have not observed.

Figure 23 presents the tip speed as a function of time and its Fourier transform for the same experiment shown in Figure 18.b. It has been generated by the injection of water at a rate of $Q = 2.9$ ml/min into a $c = 8.0\%$ solution of 100 400 molecular weight linear endcapped associative polymer, in a Hele-Shaw channel of gap $b = 0.16$ cm and width $W = 1.0$ cm. This is typical of runs with $Q > Q_{th}$ using the 100 400 molecular weight linear endcapped associative polymer and is similar to a run with the lower molecular weight comb associative polymer (Figure 18.c).
In Figure 23.a we have marked the boundaries between the viscous finger regime (it becomes unstable at $t \sim 4.8$ s), the meandering regime (it becomes unstable at $t \sim 8.3$ s), and the fast fracture regime. The inset in that figure shows the same velocity evolution after a low-pass filter is applied (it is a simple averaging filter) where we can see the main velocity oscillations more easily.
Figure 23.b shows the frequency spectrum of the last 4 s of the velocity evolution. This spectrum has been computed by taking the FFT of the original data (Figure 23.a) after a Hanning window has been applied to it, in order to reduce the power leaking due to the jump discontinuity in the time series (see section 6.1). As we explained above, the numerical window generates a peak, which is an uninteresting artifact, spanning the first three frequency channels. Beyond the third channel, we can see a smaller peak P_1 at frequency f_1 and then a succession of still smaller peaks at higher frequencies. Of all the meaningful peaks in the Fourier spectrum from a given flow realization, P_1 is the largest and it is the only reproducible peak. All these properties are true whether we Fourier analyze the tip speed or the component of the tip velocity in the channel direction. In fact, we looked for characteristic frequencies in all the measured parameters, and we found that in the tip speed is where we could see the most consistent results.
Figure 23.c is the FFT of the time series in Figure 23.a, but without any numerical windowing. We can see how the jump discontinuity in the original data has coarsened the power spectrum to the level of hiding the relevant information that we can extract if we apply the windowing. The characteristic frequency f_1 can be detected in the time series of the meandering regime alone or in the combination of the meandering

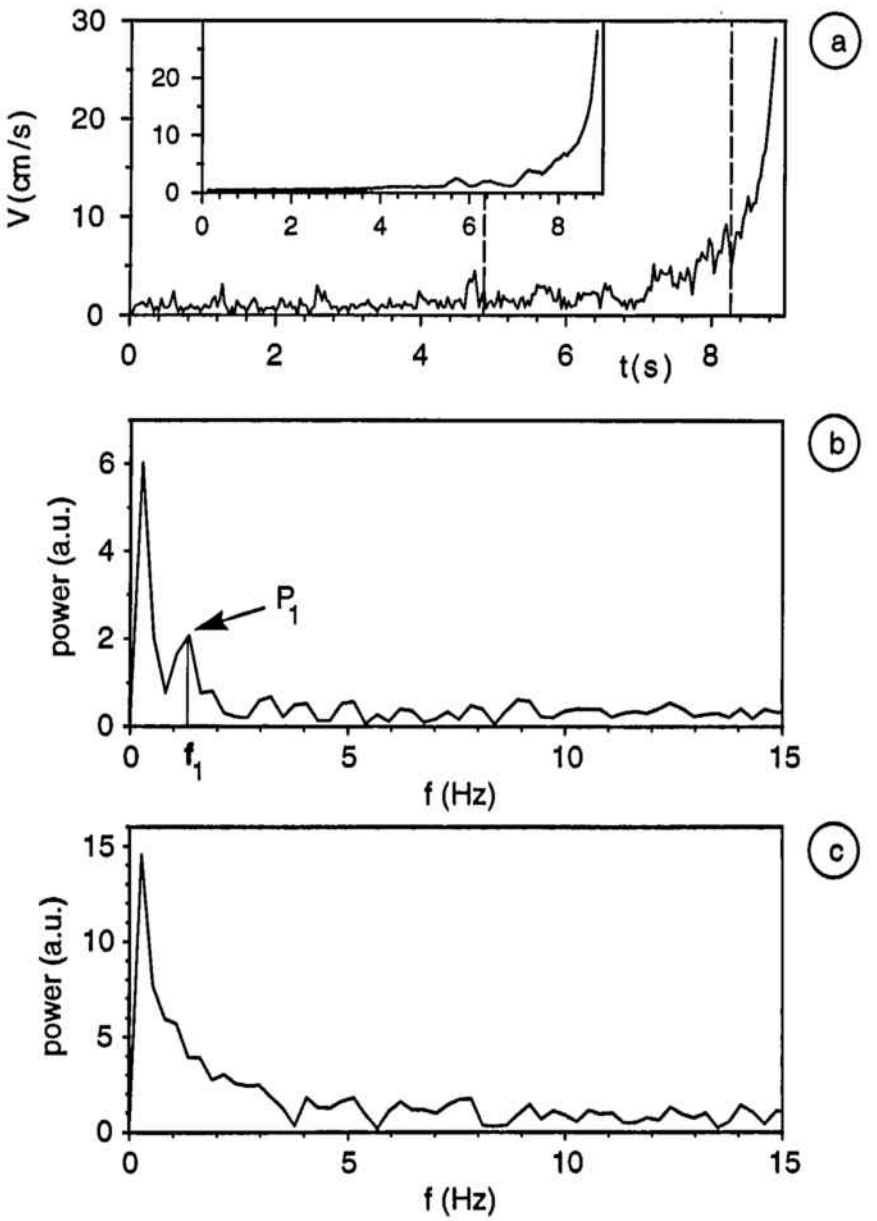

Figure 23: Time evolution and frequency spectrum of the velocity profile in a high molecular weight linear endcapped associative polymer fracture: (a) Evolution of the tip velocity, with the onset of the meandering regime, and the fast fracture regime marked. (b) Power spectrum of the meandering regime, obtained with a Hanning window. The high peak in the first three frequency channels is a numerical artifact. (c) The interesting features of the power spectrum are not visible without the Hanning window.

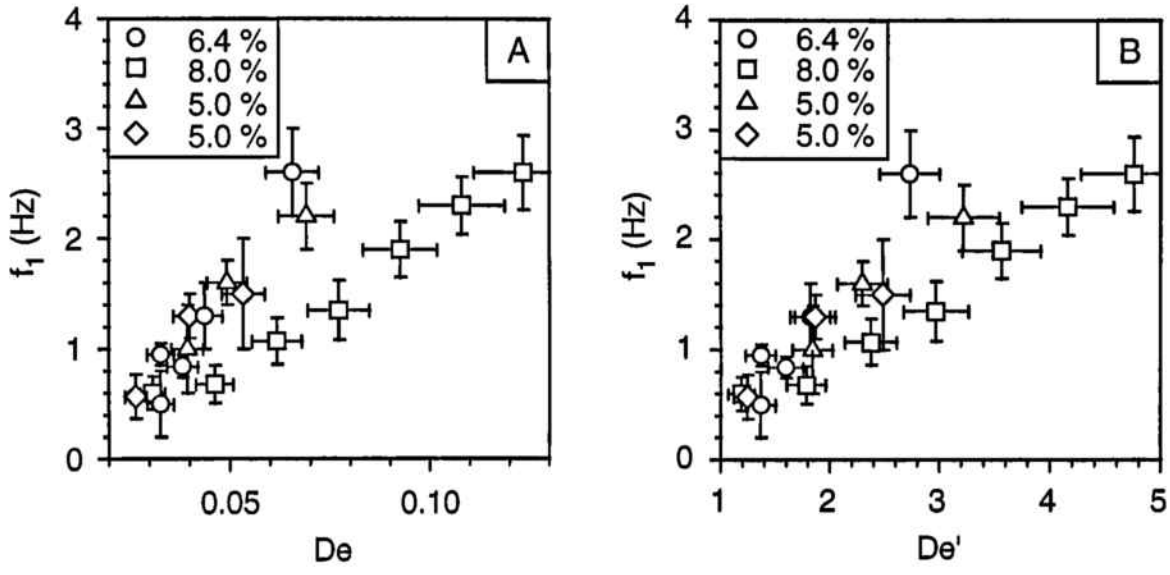

Figure 24: Dependency of characteristic meandering frequency on Deborah number, showing an approximately linear increase of f_1 with driving force. An alternate Deborah number is considered in (B), as discussed in the text.

and the fast-fracturing regime. However, it cannot be distinguished in the fast-fracturing regime alone, possibly because of a lack of experimental resolution. We have seen the frequency f_1 to depend on the rheological properties of the material, on the geometry of the channel and on the injection rate. It increases roughly linearly with injection rate (in the range of injection rates experimentally accessible). The slope of this increase depends on the geometry of the channel and on the rheology of the polymer solution.

Figure 24, left, shows f_1 as a function of Deborah number for flows at several different concentrations of the high molecular weight polymer and at different Hele-Shaw channel dimensions. The figure shows that, in the range of Deborah numbers attained, each polymer solution shows a linear dependence of the characteristic frequency on the Deborah number [or on the injection rate, since the Deborah number has been constructed as $De = Q/(Wb^2\dot{\gamma}_0)$]. We can also see that the geometric definition of the Deborah number successfully scales two experiments with the same polymer concentration (5.0%), but different channel dimensions. Similarly, data measured at concentrations of 5.0% and 6.4% are collapsed by the Deborah number scaling, even though their characteristic relaxation times [56] differ by a factor of 1.4. This collapse is not extended to the data for the 8.0% polymer concentration whose estimated relaxation time [56] is roughly twice the one for the 5.0% solution.

Just as we did when we studied the threshold for the instability of the viscous fingering regime, and defined a Deborah number to rescale the onset of this instability, it is of interest here to consider an alternate rheological time for the polymeric fluids, namely, the inverse of ω_T, the frequency at which the storage and loss moduli of the polymer solution take on the same value. As we explained above, the Deborah number obtained with this time, $De' = Q/(Wb^2\omega_T)$, is a less reliable prediction of the fracture onset. In Figure 24, right, we have rescaled the X axis using this alternate Deborah number. While the attempt to scale the data with this alternate Deborah number is not a total failure, it collapses the date less effectively that the analysis using De.

It would be interesting to learn whether the characteristic frequency we have detected mixed with noise in the meandering regime has an analog in the fracture regime. However, the spectra in the fracturelike regime are limited by our 1/30-s frame-to-frame time interval in the small number of observing frames measured during the rather short time for propagation of the crack tip through the cell. If we were able to measure for a longer time (longer cells) we would improve our frequency resolution, and we would be more sensitive in the low frequency region. If we were able to monitor the evolution at a faster frame rate, we would be more sensitive in the high frequency region. Unfortunately, we are also limited by the spatial resolution of the CCD device: using a longer cell (longer flow times) reduces the spatial resolution which increases the amount of experimental noise in the velocity measurements. We would need to obtain the images at a faster frame rate, and with a better spatial resolution to try to improve the sensitivity of our current measurements.

6.3 Summary and Unresolved Issues

We have described experiments where we measure crack-tip velocities for the injection of water into associative polymer solutions in rectangular Hele-Shaw cells. We were able to characterize the onset of fracturelike behavior and define a Deborah number which uses the shear-thinning shear rate of the polymer solution to rescale the threshold injection rate beyond which a steady-state Saffman-Taylor finger becomes unstable. This Deborah number scaling works across changes in cell dimension and across changes in polymer concentration in solution. It gives also consistent re-

sults across changes in polymer molecular weight, but it cannot rescale the onset of the fracturelike instability across changes of molecular geometry. The success in the linear endcapped associative polymers is not carried into the comb associative polymers. In the latter case, however, the results are consistent with what we observed with the linear endcapped polymers, namely, the threshold injection rate is consistent with a power law dependence on polymer concentration, which suggests a relationship with some rheological property of the material. However, the available rheology data indicates that the shear thinning shear rate cannot be directly used to rescale that data.

Both in the low molecular weight comb and in the high molecular weight linear endcapped associative polymer experiments, we observe a regime where the crack tip meanders from side to side and fluctuates in both overall speed and velocity along the channel with a characteristic frequency which depends linearly on fluid injection rate.

The linear relation we observe between the characteristic meandering frequency and the fluid injection rate (see Figure 24) is reminiscent of a very similar linear relation between the stick-slip frequency and the imposed crack velocity in the peeling of adhesive tape [64]. In those experiments, the frequency is attributed to a Hopf bifurcation, which can be analyzed in terms of measured stress-strain relations of the adhesive material. Stick-slip oscillatory behavior also disappears at higher tape peeling velocity and this is not inconsistent with our observations of fracturelike flows. In fact, we observe a fast fracture regime, where no oscillation frequency is observed. This regime, which is clearly observed for the low molecular weight linear endcapped associative polymers (where no meandering regime is observed) and at later stages of the patterns in comb associative polymers, is very reminiscent of the brittle-solid fracture results of Fineberg *et al.* [54, 55], specially when we consider the velocity profile. The literature also describes oscillatory solutions [67–69] as rather general features of quasistatic crack propagation, always in a restricted range of driving velocity, reminiscent of the results in our experiment.

We have seen that our simple way to rescale the onset of the fracturelike instability, namely, constructing a Deborah number by using a single rheological parameter ($\dot{\gamma}_0$) is not enough to rescale the results across large changes in rheology. A model to describe the dynamics of the network has been suggested by de Gennes [70]. In this

model, the lifetime of the associative bonds depends on the stress imposed on the network, and this lifetime decreases very fast with that stress. A typical dependence would be

$$\tau = \tau_1 \exp\left(-\frac{\sigma^2}{\sigma_1^2}\right), \tag{6.6}$$

where τ_1 and σ_1 are a characteristic time and a characteristic stress in the network. De Gennes suggests that σ_1 can be related to $\dot{\gamma}_0$ by $\dot{\gamma}_0 = \mu_0/\sigma_1$. This model would need two rheological parameters to describe the associative network, a time (τ_1) and a stress (σ_1). It could certainly accommodate a larger variety of phenomena that the simpler model we have used. However, it requires knowledge of a shear stress in the system, which we have not considered up to this point.

On the other hand, we would like to understand the origin of the oscillations that we can so clearly observe in the evolution of the meandering regime. We have already, in a qualitative way, associated those oscillations with some stick-slip dynamics that may be dominating our system. Kurtze and Hong [71] have explicitly considered fracturelike behavior in soft condensed matter and have predicted an oscillatory velocity for the advancing crack tip as long as the injection rate is such that the system evolution is dominated by stick-slip dynamics. They speculated that the frequency of these oscillations should increase with invading fluid injection rate. Our results are consistent with their expectations. However, the expression they present for the frequency of the characteristic oscillations requires knowledge of the shear stress in the system in order to yield quantitative results.

We see, then, that in order to advance in both the understanding of the fracturelike instability of the fingering regime and in the nature of the oscillations we observe in the meandering regime, we need to measure the shear stress in the system. The following chapter presents the analysis of the experiments with comb associative polymers where, as explained above, we monitored the pressure at the injection point as a first approximation to the stress in the system.

CHAPTER 7

Stress in the Fracturelike Patterns

As we saw in the previous chapters, we have obtained partial understanding of the instability of the fingering regime, and of the dependence of the threshold injection rate for the onset of these instabilities on the dynamics of the network.
A plausible model, presented by de Gennes [70], explores the lifetime of the associative network bonds as the relevant parameter to control the onset of the instabilities, and explores the possibility that this lifetime depends on the surrounding stress, in order to account for the complex behavior we observe (see section 6.3). On the other hand, Kurtze and Hong [71] present the only model available to us for the oscillating dynamics we have observed. In order for the system to enter an oscillating regime, they argue, a certain shear stress-shear rate response in the system is required. We will present their analysis and our attempts at extracting from there relevant information for our system. Having these models, we realized that we needed a measurement of the shear stress in the system.

Stress in viscoelastic materials can be visualized taking advantage of the change in birefringence that the medium exhibits depending on that stress [72]. We tried this approach by illuminating our channel, from below, with linearly polarized light, and observing the transmitted light with a crosspolarizer. We were unable to see the different bands of uniform stress observed in many plastic materials. Either the birefringence of our polymeric fluids is too small or the stress dissipation takes place in a very small (maybe microscopic) region around the crack tip. Since we did not have a way to directly monitor stress inside the Hele-Shaw channel, we opted for measuring the pressure of the invading fluid at the injection point, and tried to see there some signature of the stress inside the system.

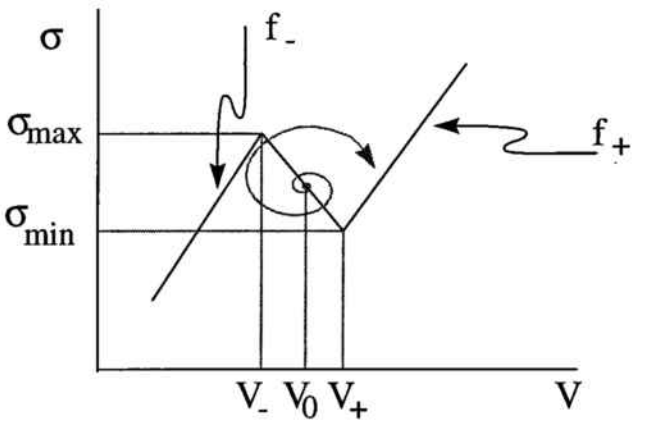

Figure 25: Expected shear stress - velocity response for the onset of stick-slip dynamics in our fracturelike experiments. An initial condition with V_0 in the unstable region will eventually generate periodic behavior.

7.1 Kurze and Hong's model for the oscillating regime

Kurtze and Hong consider the growth of an axisymmetric crack in a viscoelastic medium, confined in a Hele-Shaw channel. Their description is in terms of a *fracture zone*, or region that extends a certain length behind the tip of the crack, and where most of the stress is dissipated. The length of this fracture zone depends on the speed of the crack. This length is related to the stress and it decreases when the stress increases. Their analysis is based on the flow at constant injection rate in the viscoelastic material and on considering a characteristic rheological time of the medium. Their description, similar to what is observed in stick-slip dynamics experiments, such as the peeling of an adhesive material [64], is based on the stress-velocity response of the material.

They model a system with two dynamically stable branches (see figure 25). If the injection has a constant flow rate Q, we consider a fingering pattern developing, with cross section Σ_0 (away from the tip), and with a tip velocity $V_0 = Q/\Sigma_0$. When the injection is slow, with a tip velocity $V_0 < V_-$, where $\sigma(V_-) = \sigma_{max}$ (see figure 25), there is a slow stable flow, which we may associate with the Saffman-Taylor fingering regime. When the injection is faster, with $V_0 > V_+$, where $\sigma(V_+) = \sigma_{min}$, there is a fast stable flow, that we may associate with the fast fracture regime we observe in our experiments. There is, however, an intermediate, unstable regime, for $V_- < V_0 < V_+$.

If the flow has a steady state velocity in this region, it is unstable, and they show it will converge toward a limit cycle due to a Hopf bifurcation.

The cycle is typical of systems dominated by stick-slip dynamics: when $\sigma = \sigma_{min}$, and the system is at the bottom of the slow branch (see Figure 25), the tip velocity starts increasing, and so does the stress. When $\sigma = \sigma_{max}$, the stress is too high, and flow with a tip velocity V_- is not enough to dissipate the energy being introduced externally. There is a sudden velocity jump into the fast fracture branch. Then, both shear stress and tip velocity start decreasing until the bottom of the fast fracture branch, where the tip velocity is too high for the stress σ_{min}, and the system falls back to the slow flow branch.

Kurtze and Hong performed a linear analysis of this dynamical system, and found an expression for the frequency of the oscillations,

$$\frac{1}{f} = \int_{\Delta_-}^{\Delta_+} \left[\frac{1}{f_+(x) - V_0} + \frac{1}{V_0 - f_-(x)} \right] A(x) dx, \tag{7.1}$$

where $A(x)$ is the cross-sectional area of the fracture front, a distance x behind the tip (see D.7). Δ_+ and Δ_- are the characteristic lengths of the fracture zone, and they are related to the characteristic stresses σ_- and σ_+, respectively.

In order to compare these results with our experiments, we have performed a lowest order expansion of expression 7.1 in terms of $V_0/f_+(\sigma)$ for the fast branch and $f_-(\sigma)/V_0$ for the slow branch. using the constitutive relations from elastic solid theory in order to relate the different parameters (see appendix D). The approximation we obtain is

$$f \sim \frac{128}{729} \frac{1}{\alpha^3} \sigma_{min}^4 \frac{Q}{\mu \dot{\gamma}_0}, \tag{7.2}$$

with σ_{min} being the minimum stress in the stick-slip loop of Kurze and Hong's model; α is the surface tension at the fractured interface; μ is the zero-shear viscosity of the viscoelastic fluid; and $\dot{\gamma}_0$ is the shear thinning shear rate of the polymer solution.

This expression is interesting when we compare it with our measurements (see section 6.2). We found the oscillation frequency in the meandering regime of our fracturelike patterns to grow linearly with the injection rate. It was also linear in the Deborah number (5.1), so $f \sim Q/\dot{\gamma}_0$. Clearly, equation 7.2 shows a linear dependence of f on Q, with the slope being a combination of rheological properties of the material.

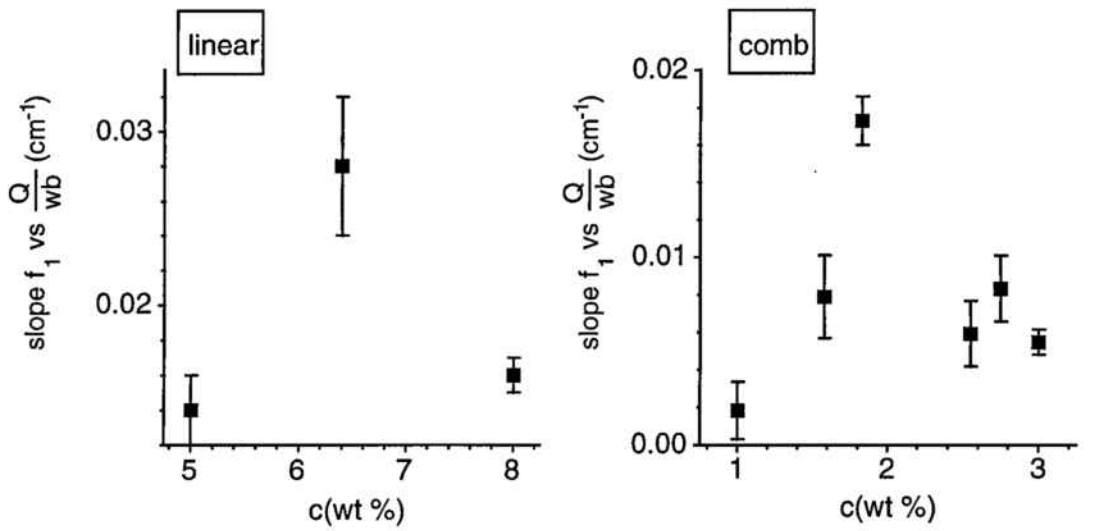

Figure 26: Effect of polymer concentration on the slope of the increase in meandering frequency with driving force.

It particularly depends very dramatically on a characteristic stress in the system.

We have measured the slope of f_1 vs. Q in these experiments (see section 6.2), and we have studied how this slope changes with concentration of the polymer in solution. We can see the results in Figure 26. In fact, in order to rescale any dependence on channel geometry, we have rescaled Q by dividing it over $b\,w$, with b being the cell gap and w the with of the pattern in the early fingering regime. This is the same scaling used in our definition of a Deborah number which successfully rescaled the geometry of the channel both for the threshold injection rate (see section 5.1) and for the oscillating frequency measurements (see section 6.2). According to the analysis above, the vertical axes in Figure 26 are, in fact, displaying the effective change of a combination of rheological parameters with concentration, namely

$$\frac{\sigma_{min}^4}{\alpha^3 \mu \dot{\gamma}_0}. \tag{7.3}$$

The systematic analysis we performed with the lowest molecular weight comb associative polymer, where we changed the rheology by changing the polymer concentration, keeping the channel dimensions constant, gives us a more complete set of data. The same analysis for the experiments with the high molecular weight linear endcapped associative polymer is presented in the same figure. In this case, however, we explored fewer different concentrations, since we were also changing the molecular

weight and the channel dimensions.

It is interesting to note that, in both polymer geometries, we observe a similar trend in the dependence of the slope on concentration. In order to do a more quantitative comparison, the axes should be rescaled by some suitable combination of rheology parameters in each case.

We lack a good enough characterization of the materials in order to compare (7.3) with the data in Figure 26. No inconsistency is found, and the unknown dependency of the different parameters on the concentration makes it difficult to give even a qualitative comparison. The fact that the slopes in Figure 26 are not monotonically changing with c, however, suggests that, at least, one of the parameters in 7.3 should depend other than as a power law on the concentration.

7.2 Evolution of the Injection Pressure

In the fracture experiments we performed using comb associative polymers, we monitored the pressure of the invading fluid at the injection point, for each run. We have studied the dependence of this pressure on injection rate and on rheology performing a series of experiments with solutions of the low molecular weight comb associative polymer, a gap of 0.16 cm and a channel width of 1.0 cm. For each run, we have obtained an average pressure, P_{ave}, which is the average of the pressure in the meandering regime (see Figure 27).

Typically (see Figure 27), the profile of a run is as follows: at early times, there is a viscous fingering regime setting up, and the pressure builds up from zero up to a maximum value. After that, the pressure starts to decay as the growing pattern approaches the open end of the channel. In a classical Saffman-Taylor flow, constant tip velocity translates into constant pressure gradient, according to Darcy's law (A.8), so if $\nabla P \sim (P_{in} - P_{out})/d$, where d is the distance from the tip of the growing pattern to the open end, P_{in} is the pressure at the tip, and P_{out} is the outside pressure at the end of the channel (constant), when d decreases, P_{in} must decrease as well to keep the gradient constant.

When, in our fracture experiments, the viscous finger becomes unstable, a mean-

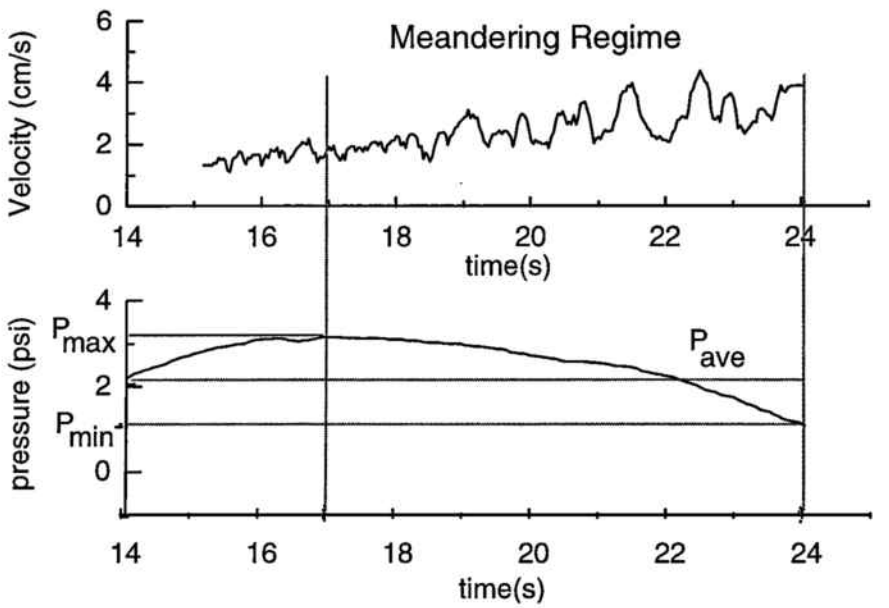

Figure 27: Typical evolution of the pressure profile in a fracturelike flow. The limits of the meandering regime are marked both in the tip-velocity evolution and in the pressure evolution.

dering regime may set up. We do not see a clear correlation between the onset of the meandering regime and any feature in the evolution of the pressure. We were expecting to see the tip velocity oscillations reflected in the pressure measurements. However, we do not seem to be sensitive to these stress oscillations (thinking in terms of Kurze and Hong's model, we can describe the system as oscillating in a stress-velocity parameter space). This is illustrated in Figure 27, where the large amplitude oscillations in the tip velocity are not present in the pressure evolution. We are confident that our pressure sensors have a fast enough response that makes them sensitive to the typical frequencies of these oscillations (the nominal response time is of the order of milliseconds). However, the fact that we monitor the pressure away from the tip of the fracturelike pattern may cause those oscillations to be dampened in the bulk of the invading fluid.

In order to analyze the meaningful features of that pressure evolution, we have extracted an average pressure for the meandering regime in each run, P_{ave} (see Figure 27), defined as

$$P_{ave} = \frac{P_{max} + P_{min}}{2}. \tag{7.4}$$

Note in that figure that the limits of the meandering regime are marked. We have plotted P_{ave} vs. Q for each run (see Figure 28). The error bars associated with

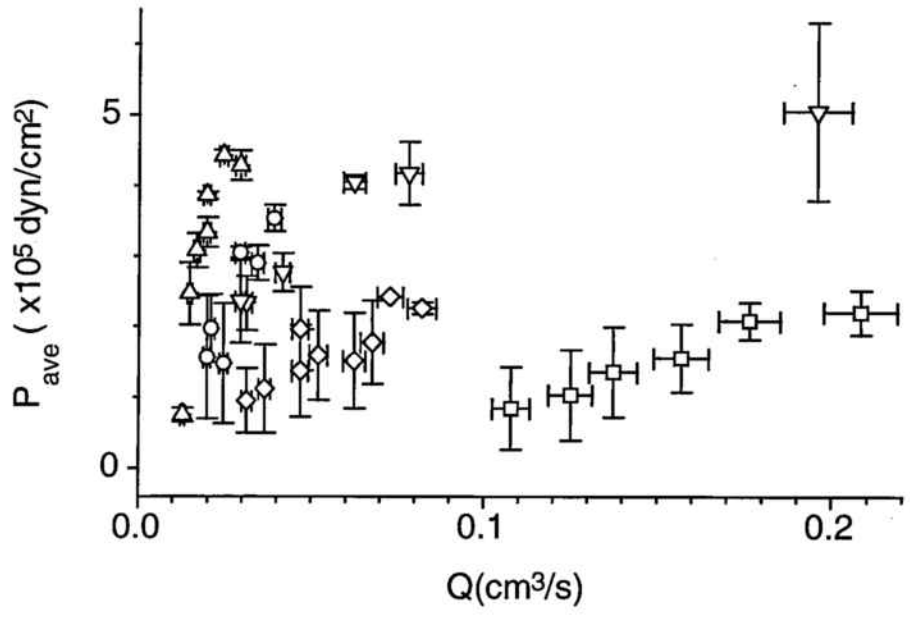

Figure 28: P_{ave} (meandering regime) vs. Q for different concentrations of comb associative polymer. □ $c = 1.58\%$, ◇ $c = 1.83\%$, ○ $c = 2.53\%$, ▽ $c = 2.75\%$, △ $c = 3.0\%$.

each data point are actually the range of pressure in the meandering regime. We see a consistent trend which is meaningful, since there are differences larger than the overlaps between pressure ranges in different flow realizations. Each different symbol corresponds to a series of runs with a given concentration of low molecular weight comb associative polymer: □ $c = 1.58\%$, ◇ $c = 1.83\%$, ○ $c = 2.53\%$, ▽ $c = 2.75\%$, △ $c = 3.0\%$.

We do not have, a priori, any expectations on how the relationship P_{ave} vs. Q could be. We have noticed that comparing the data on Figure 28 with a straight line is a good approximation. We have also tried to adjust a power law to that data, and we have found in this latter case how, consistently, the exponent of the best fit power law was, within error bars, compatible with one. Then, it seems that the linear approximation is the best and the simplest we can use. Before we try to extract more information from our data, however, we need some theoretical support in order to understand the meaning of the trend we observe. We do this in the following section, where we obtain an expression for P_{ave} vs. Q after a series of approximations are made.

7.3 Extending Darcy's law to flow of viscoelastic fluids

We saw in section 4.3 that the shape of the steady state fingers we obtained in viscoelastic flow conformed with the expected relation for Saffman-Taylor fingers, even though that relation was derived for Newtonian fluids. We will now argue, based upon a very non-rigorous set of approximations, that, under certain circumstances, it is expected that Hele-Shaw flow of viscoelastic fluids can be described with Darcy's law. In order to find the appropriate approximation for a non-Newtonian fluid, one should start with the constitutive relation for the material and do the suitable approximations from there. A discussion on the generalization of Darcy's law for non-Newtonian fluids is given by Rajagopal [73] and references therein. Since we lack a good rheological description of our materials, we will make use of much more simplistic approximations, which yield interesting results.

Since flow of a Newtonian fluid in a Hele-Shaw channel can be well described by Darcy's law (see 1.1), incompressibility implies that the pressure field will be Laplacian. The starting point to derive Darcy's law for a Newtonian fluid is the Navier-Stokes equation (eq. A.2) which has the implicit assumption that $\mu = constant$. However, in the presence of a viscoelastic material (where $\mu = \mu(\vec{v})$), the second term on the r.h.s. of eq. A.2 should read, in its X-component:

$$\frac{\partial}{\partial z}\mu\left(\frac{\partial v_x}{\partial z}\right) = \mu\frac{\partial^2 v_x}{\partial z^2} + \frac{\partial \mu}{\partial z}\frac{\partial v_x}{\partial z}. \tag{7.5}$$

A hypothesis that will allow us to recover Darcy's law is proposed by Bonn *et al.* [74], and reads

$$\frac{z}{\mu}\left(\frac{\partial \mu}{\partial z}\right) << 1, \tag{7.6}$$

which should be easily satisfied for shear rate regimes where μ has a slow variation. The flow velocity changes across the cell gap (z-direction), so the local fluid viscosity must change as well, even though this change may be negligibly small for certain shear rate regimes. With this, eq. 7.5 drops the second term on the r.h.s. and eq. A.2 remains unchanged. This way, we can extend Darcy's law to the viscoelastic

case, obtaining the averaged two-dimensional velocity field

$$\vec{v} = -\frac{b^2}{12\mu(\vec{v})}\,\vec{\nabla}P. \tag{7.7}$$

Bonn *et al.* also explain that μ can be considered as a function of the magnitude of the velocity alone, $\mu = \mu(v)$ and that $\triangle P = 0$ still holds for slow flows.

7.3.1 Effective viscosity in the meandering regime

Saffman-Taylor flow with Newtonian fluids is well described by Darcy's law (7.7), with all parameters being constant, and characterized by a constant pressure gradient and a constant velocity. In this case, we can relate V and P_{ave}, defined above, in a simple and exact way as

$$V = \frac{b^2}{6\mu L}P_{ave} + constant. \tag{7.8}$$

We can express V in terms of Q, b and w and get

$$P_{ave} = \frac{6L\mu}{b^3 w}Q + constant, \tag{7.9}$$

where we have introduced the flow rate defined as $Q = Vwb$, with w being the finger width. So, for Newtonian Saffman-Taylor flow, P_{ave} can be easily related to the fluid viscosity, and it is linear in Q.

As explained above, in our experiments with comb associative polymers, we observed that the relationship P_{ave} vs. Q (in the meandering regime) could be reasonably matched with a linear dependence (see Figure 28). Even though eq. 7.9 was derived for Newtonian fluids, let us study its usefulness in our non-Newtonian flows.

We have seen in the previous section that Darcy's law can still describe the non-Newtonian flow under certain circunstances. Even though in our case V, μ and ∇P are not a constant anymore, we may assume that we can still use eq. 7.9 as an approximation to the relationship P_{ave} vs. Q.

We have fitted a straight line in the P_{ave} vs. Q data (obtained in the meandering regime) and we have extracted the slope for each line. If we assume this slope corresponds to the relation in eq. 7.9, then it must be related to a certain averaged effective viscosity of the material over the meandering regime (where oscillations take

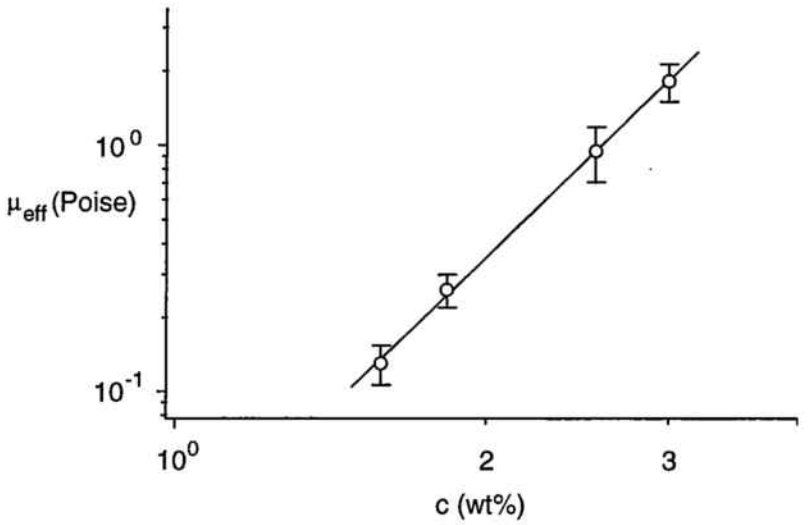

Figure 29: Effective viscosity extracted from P_{ave} in the meandering regime. The line is a power law fit to the data, giving $\mu_{eff} \sim c^{4.1}$.

place). If we put

$$P_{ave} = mQ + n, \tag{7.10}$$

we will extract

$$\mu_{eff} = m\frac{b^3 w}{6L}, \tag{7.11}$$

where b is the effective thickness across the gap filled by the growing pattern, which we have measured to be $b \sim 0.1$ cm; L is the typical spatial length of the meandering regime, which is $L \sim 15$ cm; and w is the typical width of the growing pattern, taken in the viscous fingering regime that precedes the meandering regime, where it is clearly defined, and we observe $w \sim 0.5$ cm.

This analysis yields a very interesting *effective viscosity*. As we can see in Figure 29, μ_{eff} changes very consistently with a power law with the polymer concentration (although in our limited range of concentrations). This suggests that μ_{eff} is directly related to some rheological property of the material. We find a best fit power law with $\mu_{eff} \sim c^{4.1}$.

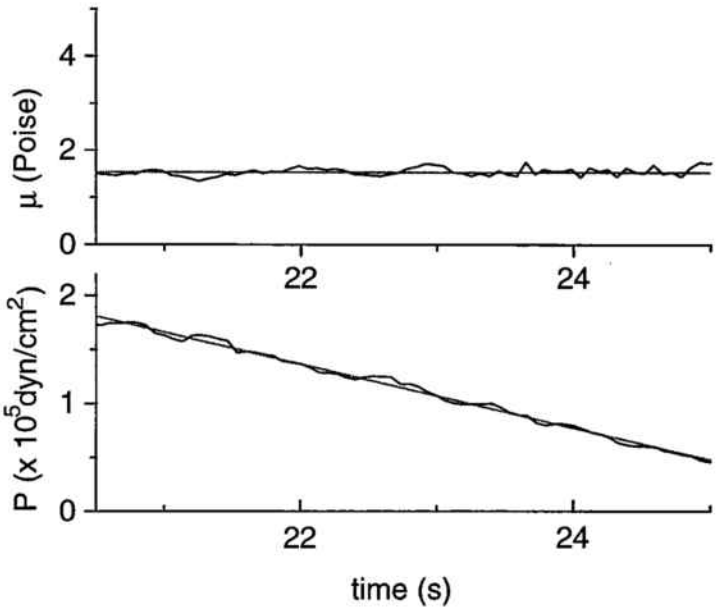

Figure 30: Monitoring the shear viscosity for glycerine. A steady-state Saffman-Taylor fingering regime is observed. The solid lines are guides to the eye.

7.3.2 Observation of the effective viscosity vs. shear rate characteristics

Monitoring $\mu(v)$ in the fracturelike flow could give interesting information about the dynamics. If we assume, based upon the same arguments given above, that Darcy's law is a valid approximation to describe the flow of our non-Newtonian fluids, we can extract μ from Darcy's law as

$$\mu(v) = -\frac{b^2}{12 v_x} \frac{\partial P}{\partial x}. \tag{7.12}$$

In our systematic experiments of flow in comb associative polymers, where we have monitored the pressure of the invading fluid at the injection point, we can obtain the time evolution of the tip velocity, and we can monitor the effective thickness across the gap of our flow (see section 6.1). Thus, all the parameters required to obtain $\mu(v)$ in eq. 7.12 are available.

Before trying to extract information from our non-Newtonian fluid data, we have tested our ability to measure the viscosity $\mu(v)$ in such a way by doing a series of experiments with glycerine, a Newtonian fluid. The glycerine we have used has a viscosity (as measured with a Brookfield Rheometer [75]) $\mu \sim$10 Poise. We have

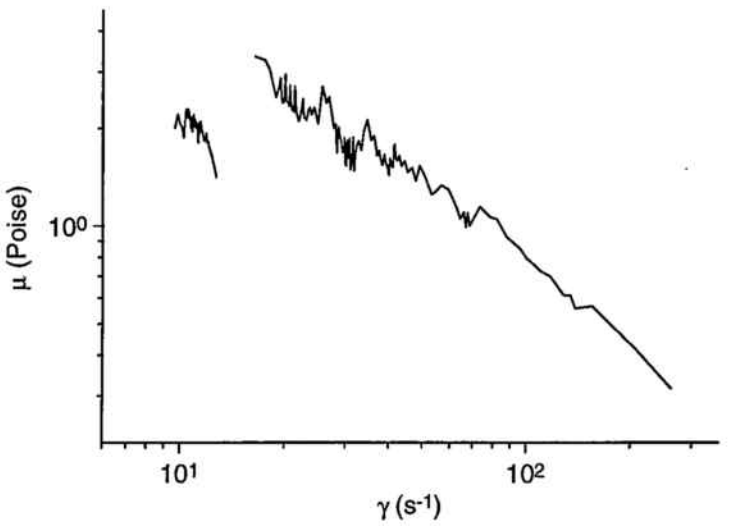

Figure 31: Effective viscosity averaged over several runs for a $c = 1.58\%$ solution of low molecular weight comb associative polymer. μ has been estimated from Darcy's law.

injected dyed water into glycerine, using the same experimental setup and analysis techniques that we used with the comb associative polymers, including monitoring of the pressure of the invading fluid at the injection point. We have used three different injection rates, and the results for the largest one ($Q = 13$ ml/min) are shown in Figure 30.

The plots are the value of the pressure (bottom) as we monitor its evolution with time, and the calculated effective shear viscosity (top) as calculated using the value of the different magnitudes at each instant of time, according to eq. 7.12. The X component of the tip velocity is measured for this Saffman-Taylor finger to be $V_x = 4.0$ cm/s. We can immediately measure the value of the (constant) pressure gradient to be $\Delta P/\Delta x = 8 \times 10^3$ dyn/cm^3. Since we measure the effective gap to be $b_{eff} = 0.1$ cm, we get, using eq. 7.12, $\mu \sim 1.6$ Poise consistently. We do not know why this value, which we reproduce with different injection rates, is a factor of around 6 times lower than the expected value $\mu = 10$ Poise (which we measure with the rheometer), but we could expect some artificial numerical factor when we do the same measurements with non-Newtonian fluids.

With the method described above, we can monitor now the effective shear viscosity of the viscoelastic medium, and we can define the shear rate at the tip of the fracturelike pattern as $\dot{\gamma} \sim V/b$, and map the evolution of a given flow realization on a shear-viscosity / shear-rate, or in a shear-stress / shear-rate map (defining the shear

stress as $\sigma(\dot{\gamma}) \sim \dot{\gamma}\mu(\dot{\gamma})$). For a given flow realization, the result is a very complex trajectory in the parameter space, from where it is not clear how to extract meaningful properties. A first attempt has been obtaining average shear-viscosity vs. shear-rate and shear-stress vs. shear-rate curves (averaging different flow realizations in order to obtain single-valued functions) and comparing the resulting curves with the available rheological data. In Figure 31 we present the result of this analysis for the flow realizations with $c = 1.58\%$ of low molecular weight comb associative polymer. Note that the value for $\dot{\gamma}_0 \sim 10^2\ \mathrm{s}^{-1}$ expected for this polymer concentration (as extracted from the data in Figure 16) is compatible with the observations plotted on Figure 31. As for the effective shear-viscosities vs. shear-rates we see here, they are roughly one order of magnitude lower that the available rheological data [61], which is consistent with some systematic experimental factor since the same problem was observed in our calibration with a Newtonian fluid (see above).

CHAPTER 8

Summary and Conclusions

Viscous flow in Hele-Shaw cells offers an interesting framework allowing for very good control on the relevant experimental parameters. The variety of challenging pattern formation situations that one can encounter is greatly increased when perturbations are added to the flow, either by using complex (non-Newtonian) fluids or by altering the geometrical properties of the cell. In this work, we have presented two sets of experiments, where both kinds of perturbations have been considered.

The first set of experiments (chapters 2 and 3) describe radial Hele-Shaw flow with Newtonian fluids where anisotropy has been added by etching a regular array of grooves on the bottom plate of the cell. This creates anisotropic modulations of the cell gap that are responsible for the appearance of a rich variety of morphologies (faceted growth, surface tension and kinetic dendrites, and tip splitting regime). In particular, the two dendritic morphologies may offer an equivalent in fluid systems for the dendrites found in crystal growth, and any understanding we may obtain from the dynamics in our relatively simpler experimental situation may be used in the field of crystal growth. We have presented a quantitative study of the growing patterns based on a theoretical model that predicts a characteristic asymptotic growth in the presence of the anisotropy. We have observed that this kind of growth has very consistent features and we have considered two parameters, experimentally measured, that can be used to quantitatively characterize the morphologies, namely, the exponent and the prefactor of the asymptotic power law growth. We have discussed the validity and the limitations of this model to describe our experiments in an attempt at going beyond the qualitative studies that characterized earlier studies of similar systems. The conclusion of our experiments is that, even though we have been able to observe experimentally the features in the dynamics of liquid dendrites only predicted in the presence of anisotropy, we have only had partial success in quantitatively char-

acterizing a given morphology. In particular, the scaling exponent in the power law behavior (eq. 3.2) seems very affected by experimental noise, which prevents from a meaningful study of the transition between different fingering morphologies.

Future work in this system involves studying the effect of static noise on the anisotropic viscous fingering, by means of the analysis tools we have developed here. The noise is superimposed to the geometrical anisotropy by a random destruction of a given fraction of the lattice of grooves. This has a strong effect on the dendritic patterns that we could try to study quantitatively.

The second set of experiments (chapters 4, 5, 6, and 7) present our work with associative polymer solutions. On top of having great technological interest, these viscoelastic fluids present very intriguing properties, from a statistical mechanics point of view. Performing Saffman-Taylor experiments with these materials, we have seen that, under certain dynamical conditions, they undergo a transition from fluidlike into fracturelike behavior. Further analysis of the dynamics shows more similarities to the fracture in brittle materials and we have observed regimes characterized by oscillations with a typical frequency that has been conjectured to be related to stick-slip dynamics in the system. A clear understanding on the dependence of the transition and the subsequent dynamic regime on the material properties may be carried into the study of fracture in brittle materials, where the shorter time scales involved impose a severe limitation in the data available [54, 55]. We have addressed these issues and we have studied the relevant features of both the transition into a fracturelike regime (where a simple Deborah number scaling successfully rescales geometrical changes and some rheological changes) and the oscillating regime. We have explained how the available models to further understand the dynamics of these complex fluids require a good knowledge of the stress in the system, and we have addressed this in a first order approximation, obtaining consistent results.

Further work in these systems is required to completely understand the nature of the transition and the nature of the dynamics governing the fracturelike regime. Systematic measurements on a larger number of model associative polymers can give some more insight in those aspects. Also, a better model for the viscoelastic flow is needed and it could very well suggest relevant magnitudes to measure.

APPENDIX

APPENDIX A

Flow in a Hele-Shaw cell. Darcy's law

A.1 Bulk equations of motion

Consider an incompressible Newtonian fluid between two parallel rigid boundaries (Hele-Shaw cell) that are wetted by the fluid, which is driven by a pressure gradient. The bulk equations for the flow are given by the incompressibility condition and by the Navier-Stokes equation [76]:

$$\vec{\nabla} \cdot \vec{v} = 0, \tag{A.1}$$

$$\rho\left(\frac{\partial \vec{v}}{\partial t} + \vec{v} \cdot \vec{\nabla}\vec{v}\right) = -\vec{\nabla}P + \mu\nabla^2\vec{v}. \tag{A.2}$$

In a steady state $\partial\vec{v}/\partial t = 0$, so equation (A.2) becomes

$$\rho\left(\vec{v} \cdot \vec{\nabla}\vec{v}\right) = -\vec{\nabla}P + \mu\nabla^2\vec{v}. \tag{A.3}$$

The boundary condition at the rigid walls ($z = \pm b/2$, see Figure 32) is no-slip:

$$\vec{v}\left(z = \pm\frac{b}{2}\right) = 0 \tag{A.4}$$

A.1.1 Channel Geometry

The pressure gradient will be along the channel, say

$$\vec{\nabla}P = \nabla P\hat{\imath}, \tag{A.5}$$

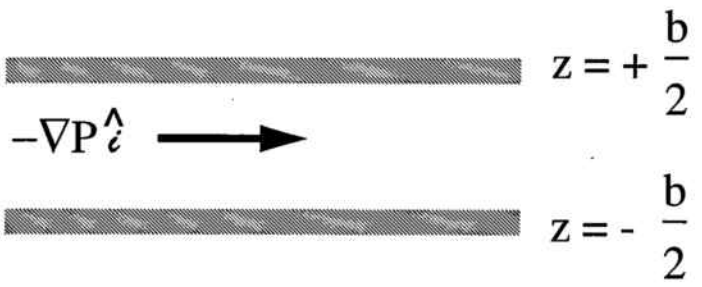

Figure 32: Poiseuille flow along a negative pressure gradient.

with ∇P constant (see Figure 1). For simplicity, let's consider a channel infinitely wide (sidewalls are at $y = \pm\infty$). This neglects sidewall effects in the flow. Then, $\vec{v} = v(z)\hat{\imath}$ and the steady state Navier-Stokes equation is

$$0 = \nabla P\hat{\imath} + \mu\frac{d^2v}{dz^2}\hat{\imath}. \tag{A.6}$$

The solution (with $v(z = \pm b/2) = 0$) is

$$v = -\frac{\nabla P}{2\mu}\left(z^2 - \frac{b^2}{4}\right). \tag{A.7}$$

A very useful quantity is the average velocity across the gap:

$$u = \frac{1}{b}\int_{-b/2}^{b/2} v(z)dz = \frac{b^2}{12\mu}\nabla P. \tag{A.8}$$

Another interesting quantity is the flow across the channel:

$$Q = b\ W\ u = \frac{b^3}{12\mu}W\nabla P, \tag{A.9}$$

where W is the channel width.

A.1.2 Radial Geometry

The pressure gradient will now be radial:

$$\vec{\nabla}P = \nabla P(r)\hat{r} = \frac{dP}{dr}\hat{r}. \tag{A.10}$$

That is, now ∇P may depend only on the distance to the injection point. The velocity field will also be radial, $\vec{v} = v(r,z)\hat{r}$.
Now, incompressibility is expressed in cylindrical coordinates as

$$\vec{\nabla} \cdot \vec{v} = 0 \quad \rightarrow \quad \frac{\partial (rv)}{\partial r} = 0 \tag{A.11}$$

For slow and slowly varying flows, v will change slowly with r. Then, we may neglect $v\partial v/\partial r$ in (A.2). We are left with (see [76])

$$0 = -\frac{dP}{dr} + \mu \left(\frac{1}{r}\frac{\partial}{\partial r}\left(r\frac{\partial v}{\partial r} \right) - \frac{v}{r^2} + \frac{\partial^2 v}{\partial z^2} \right). \tag{A.12}$$

Using (A.11):

$$\frac{1}{r}\frac{\partial}{\partial r}\left(r\frac{\partial v}{\partial r} \right) = -\frac{1}{r}\frac{\partial v}{\partial r} = \frac{1}{r^2} v, \tag{A.13}$$

which removes the terms explicit in r from (A.12). Then, (A.12) becomes

$$0 = -\frac{dP}{dr} + \mu \frac{\partial^2 v}{\partial z^2}, \tag{A.14}$$

whose solution is

$$v = -\frac{1}{2\mu}\frac{dP}{dr}\left(z^2 - \frac{b^2}{4} \right), \tag{A.15}$$

or, written in a more familiar fashion

$$v = -\frac{1}{2\mu}\nabla P \left(z^2 - \frac{b^2}{4} \right). \tag{A.16}$$

Note that, in the radial geometry, ∇P can depend on r.
We can compute the average (radial) velocity field across the gap, and obtain

$$u = \bar{v} = \frac{1}{b}\int_{-b/2}^{b/2} v(r,z)dz = \frac{b^2}{12\mu}\nabla P. \tag{A.17}$$

Another interesting quantity is the radial flow rate through a circle of radius r in the cell:

$$Q = \int_{-b/2}^{b/2} 2\pi r \, v(r,z) \, dz = \frac{\pi r b^3}{6\mu}\nabla P. \tag{A.18}$$

APPENDIX B

Dispersion relation for Radial Viscous Fingering

Consider a circular Hele-Shaw cell filled with a viscous fluid, of viscosity μ and a second, less viscous fluid, of viscosity μ', being injected through a hole at the center of the top plate. We will consider a large viscosity contast, so that we neglect the viscous dissipation inside the growing bubble ($\mu >> \mu'$). Let's assume a uniform flow rate, so that

$$\frac{dV}{dt} = Qb, \tag{B.1}$$

where V is the volume of injected fluid.

The average flow will be $\vec{v}$, governed by Darcy's law (A.17). If the flow is incompressible, the velocity potential, ϕ ($\vec{v} = -\vec{\nabla}\phi$), satisfies Laplace's equation, expressed in cylindrical coordinates as

$$\nabla^2\phi(r,\theta) = \frac{1}{r}\frac{\partial}{\partial r}\left(r\frac{\partial}{\partial r}\right)\phi(r,\theta) + \frac{1}{r^2}\frac{\partial^2\phi(r,\theta)}{\partial\theta^2} = 0. \tag{B.2}$$

Because of Darcy's law, ϕ is proportional to the pressure gradient, $\phi = b^2/(12\mu)\vec{\nabla}P$. Consider an initial steady state consisting of a circular bubble, whose radius grows with time as

$$R(t) = R_0 + \sqrt{\frac{Q}{\pi}(t - t_0)}. \tag{B.3}$$

The radial velocity of a point at the interface will be

$$\left.\frac{dr}{dt}\right|_{r=R} = \frac{1}{R}\frac{Q}{2\pi}. \tag{B.4}$$

Consider a perturbation of the velocity potential outside the bubble (in the more viscous medium, where we assume all the viscous dissipation takes place). Any such

perturbation can be expressed as a superposition of functions of the form

$$\phi(r,\theta,t) = \phi^{(0)} + \alpha(t)e^{\pm in\theta}\left(\frac{R}{r}\right)^n, \tag{B.5}$$

where $\phi^{(0)}$ is the unperturbed potential. If the circular interface is perturbed so that

$$r(\theta,t) = R(t) + Af(t)e^{\pm in\theta}, \tag{B.6}$$

we obtain, by use of the pressure boundary condition, an expression for the growth rate of the perturbation [10],

$$\frac{1}{f}\frac{df}{dt} = \frac{n-1}{R^2}\left[\frac{Q}{2\pi} - \frac{n(n+1)}{R}\frac{\sigma b^2}{12\mu}\right]. \tag{B.7}$$

If $f \sim \exp(\omega t)$, then eq. (B.7) gives a dispersion relation $\omega(n)$ between the rate of growth and the wave-number. We can see that $\omega(n)$ is positive (thus, the perturbation grows, and the radial bubble is unstable) for $n < n_c$, where

$$n_c = -\frac{1}{2} + \left[\frac{1}{4} + \frac{6\mu RQ}{\pi\sigma b^2}\right]^{1/2}. \tag{B.8}$$

This is a broad band instability, since usually several unstable modes can contribute to the growth of the perturbation. However, after a transient, the fastest growing mode, i.e., the one that maximizes $\omega(n)$ will dominate the dynamics. We can find this mode easily by maximizing B.7,

$$n_m = \sqrt{\frac{1}{3}\left(\frac{QR\mu}{6\pi\sigma b^2} + 1\right)}. \tag{B.9}$$

Equation (B.9) can be conveniently made dimensionless by a suitable election of a length,

$$n_m = \sqrt{\frac{1}{3}(R' + 1)}, \tag{B.10}$$

with

$$R' = \frac{RQ\mu}{6\pi\sigma b^2}. \tag{B.11}$$

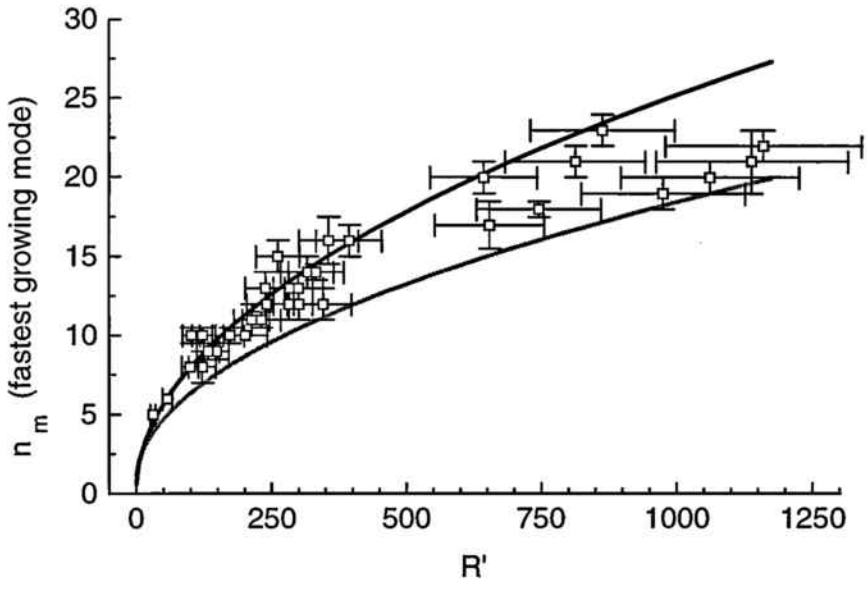

Figure 33: Dispersion relation for radial viscous fingering. The dark solid line corresponds to the theoretical dispersion relation. The light solid line corresponds to a wetting-corrected theoretical dispersion relation.

B.1 Experimental Verification of the Radial Dispersion Relation

Using a radial Hele-Shaw cell, with dry nitrogen displacing light paraffin oil (see section 2.1) we were able to experimentally obtain the dispersion relation for radial viscous fingering [53]. We used a gap of $b = 0.16$ cm, set with Teflon spacers. We prepared different circular initial conditions, in order to fix the value R_0 at which the circular interface will become unstable. The actual value for R at which the instability sets in is more accurately measured from the images, and is the one used in B.9. We explored several possible ways of measuring n_m. Since we have a broad band instability, several modes coexist. A Fourier analysis was always very noisy. Even when we studied the time evolution of the power spectrum, it was not always possible to pick a clear fastest growing mode. We found that the best results were obtained by directly counting the number of fingers at the onset of the instability, refining this number with the help of Fourier analysis, when required. Our control parameters were R and Q. All the flow realizations could be combined into the same graph by means of the dimensionless radius R' (eq. B.11). This way we could explore a much wider range of wave numbers that a single value of R could make available.

The results of our experiments are presented in Figure 33. The thick solid line corresponds to the dispersion relation B.10. We see a good agreement with the experimental data in the low R' regime. As R' increases, we see a tendency toward saturation, that we may attribute to the wetting effects becoming increasingly important in the high velocity regime. In fact, we have recalculated the expected dispersion relation including the effect of the wetting layer left behind by the displaced fluid (light line in Figure 33). This correction is based on the calculations of Yeung and Jasnow [11] and includes an average empirical wetting correction. We can see how all the data fall between the standard dispersion relation (B.10) and the one with the effective wetting correction.

APPENDIX C

Monitoring the thickness of the Fracturelike Pattern

With our experimental setup, we are able to monitor the area of a growing fracturelike pattern. However, sometimes it would be of interest monitoring the thickness across the cell gap filled by the invading fluid. We have observed that the growth of the pattern is restricted to a small region around the tip (see Figure 18). Then, it is a good approximation to consider that the change in volume, between times t and $t + dt$ is given by

$$\frac{d\,V}{dt} = \Delta y[x(t)]\; b[x(t)]\; \frac{dx}{dt}, \tag{C.1}$$

where the tip is located at $x(t)$, and the pattern has a width $\Delta y(x)$ and a thickness $b(x)$ in the tip region.

Since we have a constant and controlled injection rate (Q), $dV/dt = Q$. On the other hand, the fact that the growth is restricted, to a good approximation, to the tip region, allows us to express the area as

$$A(t) = \int_0^{x(t)} dx\; \Delta y(x), \tag{C.2}$$

that is, no explicit time dependence in the width of the pattern is needed. Then, equation C.2 gives

$$\frac{dA}{dt} = \Delta y[x(t)]\; \frac{dx}{dt}. \tag{C.3}$$

Combining this equation and C.1 we get

$$b[x(t)] = \frac{Q}{dA/dt}. \tag{C.4}$$

APPENDIX D

Lowest Order Approximation for the Oscillation Frequency in Fracturelike Patterns

A growing crack can be modeled as having regions with different dynamics [77]: the region close to the tip is the plastic zone, where high stresses are dissipated; the plastic region may be followed by a solidlike region which, in turn, may be followed by a fluidlike region. Let us consider an axisymmetric fracture profile (Figure 34), and let us model its elastic properties using those found in elastic solid theory.
Kurtze and Hong [71] have proposed an expression for the frequency of the oscillations in the fracturelike patterns in viscoelastic flow, namely

$$\frac{1}{f} = \int_{\Delta_-}^{\Delta_+} \left[\frac{1}{f_+(x) - V_0} + \frac{1}{V_0 - f_-(x)} \right] A(x) dx. \tag{D.1}$$

As explained in section 7.1, f_- and f_+ are the two stable dynamic branches in the stress-velocity response in the viscoelastic medium (see Figure 25). Since, in Kurtze and Hong's model, only the *Z-shape* of that curve is relevant, let us consider both branches to be modeled by a power law,

$$f_-(v) = \sigma_{max} \left(\frac{v}{v_-} \right)^{\beta}, \tag{D.2}$$

$$f_+(v) = \sigma_{min} \left(\frac{v}{v_+} \right)^{\beta}. \tag{D.3}$$

From elastic solid theory [78], we get an expression for the opening of the crack,

$$u(x) \sim \frac{K_0}{2G} x^{1/2}, \tag{D.4}$$

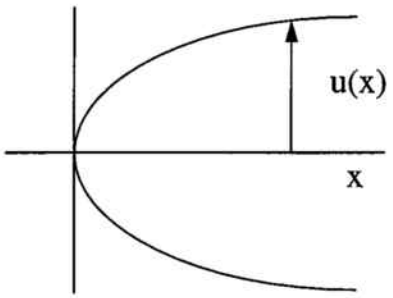

Figure 34: Axisymmetric fracture profile.

and the stress in the fracture zone, a distance x from the crack tip

$$\sigma(x) \sim K_0 x^{-1/2}, \quad K_0 = \frac{3}{2}\sqrt{\frac{\alpha G}{\pi}}, \tag{D.5}$$

where G is the shear modulus and α is the surface tension. This way we can express the two limits of the length of the fracture zone, Δ_+ and Δ_- in terms of the stress,

$$\sigma_{max} \sim K_0 \Delta_-^{-1/2}, \ \sigma_{min} \sim K_0 \Delta_+^{-1/2}, \tag{D.6}$$

and the cross sectional area $A(x)$ in terms of the opening of the crack,

$$A(x) = \pi u(x)^2 \sim \pi \left(\frac{K_0}{2G}\right)^2 x. \tag{D.7}$$

Next, we replace all these expressions in D.1, in order to get an expression under the integral sign that depends on σ. We make one more simplification considering that most of the period of one oscillation is spent in the slow branch, so we neglect the contribution of the fast branch. We perform a lowest order expansion of expression D.1 in terms of $V_0/f_+(\sigma)$ for the fast branch and $f_-(\sigma)/V_0$ for the slow branch. We obtain the expression

$$f \sim \frac{128}{729} \frac{\Sigma_\infty}{\alpha^3 G} \frac{\sigma_{min}^4 \sigma_{max}^4}{\sigma_{max}^4 - \sigma_{min}^4} V_0. \tag{D.8}$$

Finally, we take into account that $\mu \sim \tau G$, where μ is the shear viscosity and τ is a characteristic rheological time which, in our experiments, we have taken to be $\tau \sim 1/\dot{\gamma}_0$; and $Q = V_0 \Sigma_\infty$, where Σ_∞ is the cross section of the crack away from the tip. If we also assume $\sigma_{min} << \sigma_{max}$, the final expression for f is

$$f \sim \frac{128}{729} \frac{1}{\alpha^3} \sigma_{min}^4 \frac{Q}{\mu \dot{\gamma}_0}. \tag{D.9}$$

RESUM EN CATALÀ

I Introducció

La formació d'escructures en matèria condensada tova ha estat objecte d'un extensiu estudi durant gran part de les dues dècades passades [1–5]. La configuració utilitzada en els nostres experiments (cel·la de Hele-Shaw) és prou senzilla com per poder ser descrita de forma simple analíticament. Malgrat això, la natura no-linial i no local de les equacions fa que puguin generar una fenomenologia prou rica. El problema bàsic, on una cel·la de Hele-Shaw llisa (sense rugositats) i fluids newtonians són utilitzats, pot ésser extés mitjançant la introducció de diferents tipus de perturbacions, bé modificant la cel·la, bé utilitzant fluids complexos [6].

Les estructures i la fenomenologia observades en els nostres experiments amb dendrites líquides (vegeu secció II) presenten fortes similituds, qualitativament parlant, amb les dendrites observades en el creixement de cristalls. De fet, les equacions utilitzades per modelar ambdós sistemes són tan similars que es raonable pensar que els resultats que trobem en els nostres senzills sistemes poden ser aplicats al creixement de cristalls. A més, els experiments en creixement de cristalls tenen, típicament unes escales de longitud i de temps molt més petites, la qual cosa fa que l'anàlisi quantitativa sigui força més dificultosa. D'altra banda, els nostres experiments amb fluids complexos exhibeixen una transició cap a estructures l'evolució de les quals presenta, qualitativament, una forta ressemblança amb la que s'observa en la fractura de sòlids fràgils. En la fractura de sòlids, interessa relacionar l'inici del procés de fractura i la dinàmica que segueix amb les propietats del material. En els nostres experiments de fractura en medis fluids, tenim informació sobre les propietats reològiques del nostres fluids polimèrics, i intentem relacionar aquestes propietats amb la dinàmica que observem. A més, en seguir una dinàmica més lenta, els nostres experiments ofereixen un marc on és possible fer mesures més completes i amb més facilitat del que és obtenible amb sòlids fràgils.

Una cel·la de Hele-Shaw (HS) és un sistema format per dues plaques rígides (habitualment fetes de vidre o Plexiglas), col·locades paral·lelament, amb un petit espai o *gap* entre elles. El gap s'omple d'un fluid viscós i un segon fluid, menys viscós, s'injecta desplaçant el primer fluid. El cas més comú és aquell en el qual la viscositat del fluid invasor és negligible comparada amb la del més viscós. Els nostres experiments utilitzen dues geometries diferents: geometria en canal o rectangular, en la qual les plaques tenen forma rectangular, amb un gradent de pressió aplicat al llarg

del canal; i geometria radial, on les plaques són circulars, i el gradent de pressió és aplicat pel fluid menys viscós en ésser injectat per un orifici en el centre d'una de les plaques. La formació d'estructures interessant es produeix quan la interfície entre els dos fluids esdevé inestable. El fet que el gap de la cel·la sigui petit imposa una gran impedància al flux, de forma que la dinàmica dels fluids es pot cosiderar confinada a dues dimensions. Es pot demostrar que la velocitat promitjada a través del gap, i el gradent de pressió satisfan la relació

$$\vec{v} = \frac{b^2}{12\mu}\vec{\nabla}P, \tag{1}$$

on $\vec{v}$ és la velocitat de flux en el fluid, μ és la viscositat dinàmica del fluid, b és el gap de la cel·la i P és la pressió en el volum del fluid. Aquesta relació rep el nom de llei de Darcy, i és la mateixa relació que descriu el flux d'un fluid viscós a través d'un medi porós. L'ús de la llei de Darcy suposa una descripció bidimensional del flux en la cel·la de HS, i serà un model vàlid sempre que els efectes tridimensionals siguin negligibles. Exemple d'efectes tridimensionals són la consideració d'un *menisc* tridimensional en la interfície, o la descripció d'una cel·la de HS on el gap b varia localment, $b = b(x, y)$. Considerarem, a més, que els nostres fluids són incompressibles, de forma que

$$\vec{\nabla} \cdot \vec{v} = 0. \tag{2}$$

Combinant (1) i (2) arribem a

$$0 = \vec{\nabla} \cdot \vec{v} = \vec{\nabla} \cdot \frac{b^2}{12\mu}\vec{\nabla}P = \vec{\nabla}\left(\frac{b^2}{12\mu}\right) \cdot \vec{\nabla}P + \nabla^2 P = 0. \tag{3}$$

En cas que el terme $b^2/12\mu$ sigui uniforme en l'espai, obenim l'equació de Laplace per la pressió,

$$\nabla^2 P = 0. \tag{4}$$

La situació relevant en els nostres experiments és aquella on hi ha dos fluids, l'un desplaçant l'altre, amb una interfície mòbil entre ells. A més, considerem un contrast infinit de viscositats, és a dir, negligim la viscositat d'un dels fluids en front de la de l'altre (simplificació perfectament vàlida en els nostres experiments). A més, ignorem efectes gravitacionals.

Les equacions d'evolució en el volum s'han de complementar amb condicions en

la interfície. Particularment, hi haurà un salt en la pressió entre ambdós costats de la interfície, donat per l'equació de Gibbs-Thomson [3],

$$P|_S = \sigma\left(\frac{2}{b} + \kappa\right) + P_0, \tag{5}$$

on σ és la tensió superficial i κ és la curvatura local en la interfície. En la literatura trobem correccions cinètiques a aquesta relació [9, 11, 12]. A més, els nostres experiments es duen a terme a ritme d'injecció constant, de forma que

$$\int \hat{n} \cdot \vec{v} ds = Q. \tag{6}$$

En geometria radial o circular, la injecció es duu a terme forçant el fluid menys viscós a través d'un orifici en el centre de la cel·la, desplaçant el fluid més viscós que omple l'espai del gap. La bombolla circular que creix pot esdevenir inestable respecte de deformacions ondulatòries. Si això passa, ben aviat obtenim un estructura on *dits* viscosos creixen, sense arribar a un estat estacionari. Fins i tot, la possibilitat d'observar un estat assimptòtic no està clarament establerta.

En geometria rectangular es pot arribar a obtenir un estat estacionari, en el qual un únic dit viscós avança, centrat en el canal, ocupant aproximadament la meitat de l'amplada [3, 7, 14]. La forma del dit és ben aproximada per la relació de Saffman-Taylor[14]

$$x = \frac{W(\lambda - 1)}{\pi} \ln\left[\cos\left(\frac{\pi y}{\lambda W}\right)\right], \tag{7}$$

on λ és la raó entre l'amplada del dit i la del canal.

És habitual estudiar la dependència entre λ i el paràmetre de tensió superficial [18]

$$\frac{1}{B} = \frac{12\mu V W^2}{\sigma b^2}, \tag{8}$$

on μ és la viscositat del fluit desplaçat, V és la velocitat del cap del dit, W és l'amplada del canal i σ és la tensió superficial.

La introducció d'efectes de mullat [17, 19] aporta una millora en l'acord entre prediccions teòriques i resultats experimentals per λ en funció de $1/B$.

I.A Pertorbacions a fluxos de Hele-Shaw radials

La presència d'anisotropia en el flux de Hele-Shaw radial i isotròpic canvia la natura del problema per tal com noves morfologies (per exemple, dendrites) són possibles. Ben Jacob i col·laboradors [21] van proposar un model fenomenològic local (*Boundary Layer Model*) per descriure la dinàmica de la interfície mòbil, el qual és igualment aplicable en solidificació, flux de Hele-Shaw, etc. Van mostrar com l'aparició de dendrites és una prova clara de la presència d'anisotropia, tot i que diferents morfologies poden ser trobades, canviant les condicions dinàmiques, en presència d'anisotropia.

Hi ha diferents formes d'introduir, experimentalment, anisotropia en el sistema. En la literatura trobem l'ús d'una petita bombolla en el cap que avança d'un dit viscós [22, 23] i l'ús de cristalls líquids [5, 24, 25] com a mecanismes que permeten observar fases dendrítiques. Trobem tambe experiments on s'introdueixen escletxes gravades en les plaques [21, 26, 27] per tal d'introduir anisotropia en el sistema. En aquests treballs trobem un estudi de l'efecte qualitatiu que diferents paràmetres de control, com el gradent de pressió o la profunditat relativa de les escletxes, tenen en les morfologies observades. Nogensmenys, no trobem cap estudi quantitatiu de les observacions experimentals, i no és gens clar com arribar a relacionar, d'una forma quantitativa, els paràmetres controlables experimentalment amb el paràmetre que introdueix l'anisotropia en l'anàlisi teòrica. L'ús d'una xarxa d'escletxes grabades en una de les plaques presenta el millor control sobre els paràmetres experimentals, i ofereix resultats ben reproduibles. En la secció II presentem experiments amb fluids newtonians en geometria radial on introduïm pertorbacions en forma d'una modulació periòdica del gap. Presentem a l'hora una anàlisi qualitativa i també una anàlisi quantitativa, basada en un model teòric que prediu unes relacions d'escala en presència d'anisotropia. Malgrat que verifiquem experimentalment les prediccions del model teòric, no hem trobat una resposta definitiva a com caracteritzar de forma quantitativa una morfologia determinada.

I.B Flux de Hele-Shaw amb fluids viscoelàstics

És previsible que l'ús de fluids viscoelàstics en fluxos de Hele-Shaw tingui efectes relevants quan el règim dinàmic posi en joc les propietats no-newtonianes del fluid (esforços normals, variació de la viscositat amb els esforços de cisalla, relaxació dels

esforços, etc.). Tal i com expliquem en la secció següent, les pertorbacions al flux de fluids newtonians té l'efecte més notable en la zona interficial. En contrast, en l'ús de fluids no newtonians, amb una viscositat que depèn de la velociat del flux, les pertorbacions seran relevants, no només en la zona interficial, sino també en el volum. L'efecte de fluids viscoelàstics en flux de Hele-Shaw va ser inicialment explorat per Nittman, Daccord i Stanley [28, 29], i per van Damme i col·laboradors [30–33]. De Gennes també ha estudiat l'efecte de fluids viscoeàstics en flux de Hele-Shaw. Recentment, s'han analitzat els efectes viscoelàstics en estructures que creixen en fluids miscibles [35, 36], mostrant canvis dràstics en les morfologies que es poden obtenir. Té un interés particular el fet que, en certes condicions de flux intens, els fluids viscoeàstics poder ser induits a generar estructures de quasi-fractura, més similars a la fractura en materials fràgils que al flux de fluids newtonians. Tals observacions s'han fet en suspensions de fang [31–33, 37] i en solucions de polímers associatius [38]. En la segona part d'aquesta tesi, mostrem els nostres experiments amb solucions de polímers associatius, els quals exhibeixen una transició entre un comportament fluid i un comportament de quasi-fractura. En la secció III descrivim els nostres experiments i el nostre fructuós (si bé limitat) intent per trobar una relació d'escala pel llindar de la transició a quasi-fractura, i també les tendències trobades en l'estudi de l'evolució de la freqüència característica en règims oscil·latoris. També descrivim els nostres intents per obtenir un major enteniment de la relació entre els fenòmens observats i les propietats reològiques dels materials.

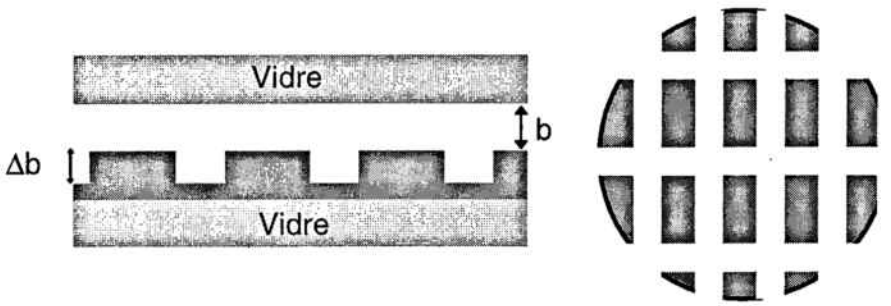

Figura 1: Esquerra: Perfil de la placa grabada dins del gap. Dreta: vista superior de les escletxes grabades.

II Introducció de pertorbacions regulars en la cel·la radial de Hele-Shaw

Hem dissenyat experiments en els quals introduïm anisotopia en el flux de fluids newtonians en una cel·la de H-S radial [39]. En condicions normals, el gap és uniforme en tota la cel·la i, atès que els fluids són newtonians, no hi ha cap direcció afavorida en el flux. Per tal d'introduir l'anisotropia, hem modificat la cel·la de H-S de forma que la cara interior de la placa inferior conté un grabat regular en forma d'escletxes constituint una xarxa rectangular amb una distància entre els centres de les excletxes de 0.4 mm en una direcció i 0.8 mm en l'altra. Les escletxes tenen una amplada de 0.2 mm i una profunditat de 0.07 mm (vegeu Figura 1). Les plaques són de vidre rígid, per evitar deformacions i tenen un diàmetre de 40 cm. L'espai del gap està ple d'oli de parafina ($\mu = 1.6$ Poise, $\sigma = 3.5$ dyn cm^{-1} a 22°C) el qual actua com a fluid més viscós. A través d'un forat en el centre de la placa superior, injectem Nitrogen amb un ritme d'injecció constant Q. Les estructures que creixen són enregistrades i analitzades digitalment mitjançant un programa de tractament d'imatges.

II.A Anisotropia i creixement dendrític. Diferents morfologies

És ben conegut [20, 45] que la presència d'anisotropia és una condició necessària per obtenir estructures dendrítiques, tant en solidificació direccional com en creixement viscós. L'efecte de l'anisotropia en un experiment determinat, però, depén de diversos

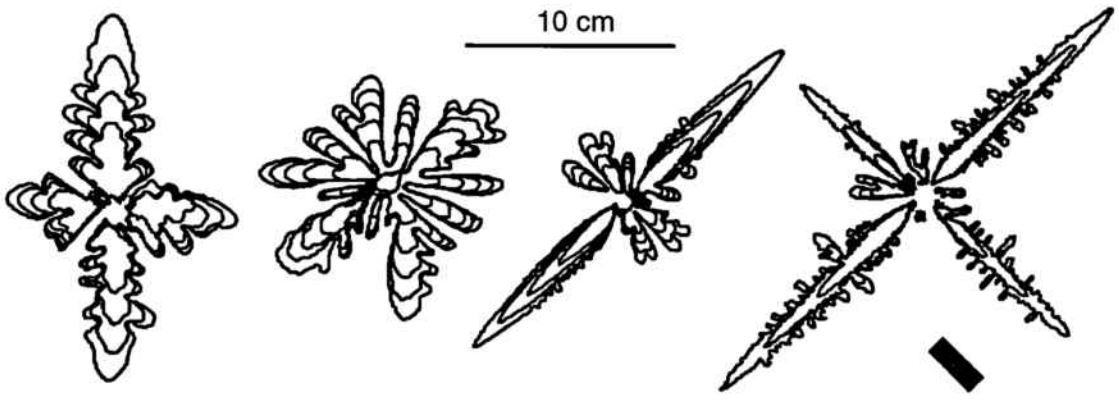

Figura 2: Morfologies en creixement viscós anisotròpic amb $b = 0.11$ mm. El rectangle indica l'orientació del grabat. D'esquerra a dreta: $Q = 1.3$ cm^2/s, $Q = 1.8$ cm^2/s, $Q = 5.5$ cm^2/s i $Q = 48$ cm^2/s.

paràmetres de control, com el valor del gap, el ritme d'injecció, etc., podent obtenir diferents morfologies [46]. En la Figura 2 donem un exemple de les diferents morfologies que podem observar variant el ritme d'injecció Q. En els nostres experiments, ens hem centrat en l'estudi de les dues morfologies dendrítiques:

- a *velocitats petites* observem dendrites que creixen allunyant-se de les escletxes, presumiblement degut als efectes de tensió superficial que afavoreixen el creixement minimitzant la secció transversal de l'estructura (és el cas de l'estructura per $Q = 1.3$ cm^2/s en la Figura 2). Les anomenem *dendrites de tensió superficial*;

- a *velocitats altes* observem dendrites que creixen seguint les escletxes, presumiblement degut a efectes cinètics, els quals afavoreixen el creixement en la direcció que minimitzi la impedància al flux (és el cas de l'estructura per $Q = 5.5$ cm^2/s ó $Q = 48$ cm^2/s en la Figura 2). Les anomenem *dendrites cinètiques.*

L'objectiu dels nostres experiments és analitzar, de forma quantitativa, l'efecte de l'anisotropia introduïda en el sistema, tot relacionant-la amb les estructures que en resulten, és a dir, relacionant els paràmetres experimentals amb aquestes estructures. Per això necessitem també una forma de caracteritzar, quantitativament, la morfologia de les estructures que creixen en la nostra cel·la.

II.B Paràmetres controlables experimentalment

En els nostres experiments hem observat com la morfologia en les estructures de creixement viscós pot ser alterada mitjançant tres paràmetres controlables experimentalment:

- $a = \Delta b/b$, la raó entre la profunditat de les escletxes i el gap promig de la cel·la. Hem observat com un increment en a augmenta dramàticament l'efecte de l'anisotropia en les estructures.
- Q, el ritme d'injecció (més precisament, el canvi d'àrea de la bombolla per unitat de temps). Veiem com, per a fixat, canviant Q podem canviar la morfologia tal i com s'observa en la Figura 2.
- l'escala de longitut característica de la modulació del gap. Per exemple, en els nostres experiments, on tenim una xarxa rectangular, observem comportaments diferents segons la direcció de creixement sigui paral·lela al costat curt o al costat llarg dels rectangles.

Tot i que no tenim una forma precisa d'expressar el paràmetre d'anisotropia utilitzat en les expressions teòriques en termes d'aquests paràmetres de control, creiem que serà una combinació d'ells, recullint les variacions observades experimentalment en l'efecte de l'anisotropia sobre les estructures.

II.C Caracterització quantitativa de les estructures

Malgrat que l'anisotropia actua com una pertorbació singular quan la introduïm en aquests experiments[4], els seus efectes depenen de la *intensitat* de l'anisotropia. Si la intensitat és baixa, els efectes anisotròpics esdevenen negligibles i creixement basat en *tip splitting* domina [47].

En una anàlisi teòrica, l'efecte de l'anisotropia apareix en la condició de contorn per la pressió, avaluada en la interfície,

$$P|_S = \sigma f(\theta)\kappa + \beta g(\theta) v_n^\gamma, \tag{9}$$

on σ és la tensió superficial, β és un coeficient cinètic, θ és l'angle local entre la normal a la interfície i la xarxa, v_n és la velocitat normal local i κ és la curvatura local. A altes velocitats, el terme proporcional a v_n dominarà, i a velocitats petites, serà negligible. Atès que $f(\theta)$ i $g(\theta)$ han d'introduir els efectes de simetria de la xarxa, és habitual trobar expressions del tipus

$$f(\theta) = 1 - \epsilon\cos(m\theta), \tag{10}$$

$$g(\theta) = 1 - \chi\cos(m\theta + \delta), \tag{11}$$

on ϵ i χ són paràmetres d'anisotropia, els quals quantifiquen els efectes de l'anisotropia en les estructures. A més, m dóna la simetria de l'anisotropia i δ aporta la competició entre efectes de tensió superficial i efectes cinètics per triar la direcció afavorida de creixement.

Almgren i col·laboradors [49] han estudiat el creixement viscós en presència d'anisotropia mitjançant la introducció del terme

$$P|_S \sim \kappa(1 - \epsilon\cos(m\theta)), \tag{12}$$

en la condició de contorn per la pressió. Cal notar que aquesta descripció negligeix completament els efectes cinètics. La seva anàlisi presenta resultats assimptòtics que només són assolibles en presència d'anisotropia. En els seus càlculs, Almgren i col·laboradors prediuen que, en presència d'anisotropia en la tensió superficial, la distància des del cap d'una dendrita que creix fins al seu punt d'injecció escalarà amb el temps com

$$x_{tip} = At^{\alpha}. \tag{13}$$

En simulacions, troben una evolució en la forma d'una dendrita creixent que pot ser escalada amb el temps com

$$x \sim t^{\alpha}, \tag{14}$$

$$y \sim t^{1-\alpha}, \tag{15}$$

expressions que satisfan la condició imposada de flux constant ($xy \sim t$). Mitjançant les seves anàlisis, troben un valor esperat $\alpha = 3/5$ ($= 0.6$), independent dels detalls i de la intensitat de l'anisotropia imposada. Només el prefactor A seria sensible a aquests detalls. També troben l'expressió que descriu la forma a la qual tendeixen,

assimptòticament, les dendrites:

$$y(x,t) = \frac{Q}{2\pi}\frac{1}{\alpha A}t^{2/5}Y_m\left(\frac{x}{At^\alpha}\right), \tag{16}$$

on

$$Y_m(\rho) = \rho^{2/3}\int_\rho^1 \frac{ds}{s^\gamma\sqrt{1-s^m}}, \quad \gamma = \frac{5}{2} - \left(\frac{m}{2} - 1\right). \tag{17}$$

En aquestes expressions es considera que l'anisotropia té una periodicitat angular $2\pi/\mathrm{m}$.

Una conseqüència de les equacions que descriuen el flux de H-S, un cop assumim el comportament $x \sim At^\alpha$, és la relació [51]

$$x \sim A'Q^{3\alpha-1}b^{2(1-2\alpha)}t^\alpha, \tag{18}$$

on A' és independent de Q i de b. Així, si $\alpha \sim 0.6$, és d'esperar

$$A \sim A'\left(\frac{Q}{\sqrt{b}}\right)^{0.8}. \tag{19}$$

II.D Procediment experimental i resultats

En cada assaig experimental obtenim una bombolla de nitrogen que creix desplaçant l'oli mineral que omplia el *gap*. L'estructura que es desenvolupa és enregistrada i analitzada digitalment. Directament, obtenim l'evolució de l'àrea i de la posició del cap de cada branca de l'assaig. A continuació, verifiquem la validesa de $x_{tip} \sim At^\alpha$ i, en cas favorable, obtenim A i α ajustant aquesta expressió als resultats experimentals. Aquest procediment el repetim amb tota una gamma de valors per b i per $\tilde{Q}$ ($\tilde{Q}$ és el ritme de creixement de la branca estudiada). D'aquesta forma, obtenim una sèrie de parelles (α, A) en funció dels nostres paràmetres ajustables experimentalment, $(b, \tilde{Q})$. A més, tot i que l'estudi teòric del qual disposem només considera anisotropia en la tensió superficial, hem observat que la relació d'escala $x_{tip} \sim At^\alpha$ es satisfà també en el cas de dendrites cinètiques amb, potser, un valor diferent per α.

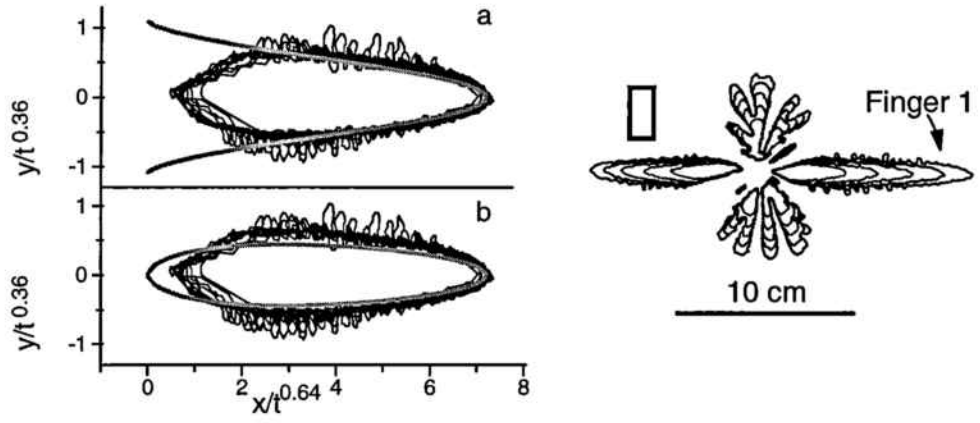

Figura 3: Observació de la forma assimptòtica predita per dendrites cinètiques: (a) simetria a dues bandes, (b) simetria a quatre bandes. La forma amb simetria a dues bandes s'ajusta millor a les nostres dades. La dendrita cinètica que evoluciona (dreta) ha estat reescalada utilitzant $\alpha = 0.64$. El rectangle mostra l'orientació del grabat.

Verificació de la llei d'escala

La primera pregunta que ens fem és: quina és la relació entre α i la morfologia de l'estructura considerada? Tenint en compte que l'aparició de la relació d'escala $x_{tip} \sim At^{\alpha}$ només es verifica en presència d'anisotropia, és raonable esperar que, quan aquesta anisotropia canvii d'intensitat, α reflexi, d'alguna forma, aquest canvi ($\alpha = 0.5$ s'observa en absència total d'anisotropia), amb potser algun comportament de α que sigui una prova d'una transició de fase morfològica.

Els resultats, però, mostren una gran dispersió en els valors obtinguts per α. Així, per branques dendrítiques que, visualment i considerant la seva estructura, són clarament classificables, bé com a dendrites de tensió superficial, bé com a dendrites cinètiques, podem obtenir valors de α bastant diferents, de forma que és difícil utilitzar el valor de α per caracteritzar una morfologia donada. L'únic efecte que notem en α quan l'anisotropia disminueix d'intensitat és una major dispersió, acompanyada d'un empitjorament en la validesa de la relació d'escala ($x_{tip} \sim At^{\alpha}$). Així, en l'anàlisi de 45 branques en el règim controlat per la tensió superficial, obtenim $\alpha = 0.64 \pm 0.098$. D'altra banda, analitzant 29 branques corresponents al règim cinètic, obtenim $\alpha = 0.66 \pm 0.096$. Clarament, la dispersió en els valors per α no permet fer cap distinció entre ells. En els casos on la relació d'escala es satisfà, hem pogut també comprobar com la forma de la dendrita líquida pot ser ben descrita per la relació assimptòtica (16), tal i com es pot veure en la Figura 3.

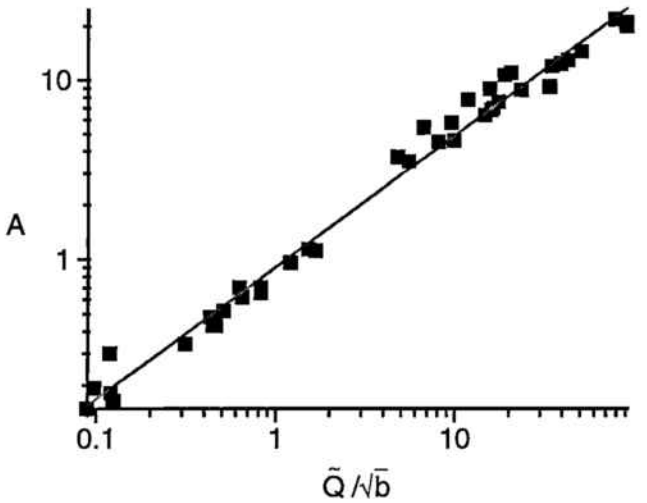

Figura 4: Creixement viscós anisotròpic. A vs $\tilde{Q}/\sqrt{b}$ per $b = 0.11$ mm, $b = 0.22$ mm i $b = 0.37$ mm combinats.

Regularitat en A respecte $\tilde{Q}$

Tot i que en el cas de simetria quadrada ($m = 4$) la relació entre A i ϵ ha estat calculada analíticament, en el cas de simetria rectangular no tenim cap expressió analítica per la relació entre aquests paràmetres. En els nostres experiments, ens hem concentrat en l'anàlisi de dendrites per les quals $\alpha \sim 0.6$. Si representem gràficament les nostres mesures de A respecte $\tilde{Q}$, trobem que les dades segueixen una tendència que pot ser modelada com $A \sim \left(\tilde{Q}/\sqrt{b}\right)^{\beta}$ (Figura 4). En l'esmentada figura, hem inclós tant experiments amb dendrites de tensió superficial com amb dendrites cinètiques. En aquesta anàlisi que inclou experiments amb gaps $b = 0.11$ mm, $b = 0.22$ mm i $b = 0.37$ mm, obtenim, ajustant una llei de potències, $\beta = 0.71 \pm 0.01$ (comparable al valor $\beta = 0.8$ produit per l'anàlisi teòrica (19) .

II.E Sumari i questions per resoldre

Hem presentat experiments de creixement viscós on, mitjançant la introducció d'anisotropia, hem extés la gamma de morfologies que es poden observar. La intenció del nostre estudi ha estat fer una anàlisi quantitativa de les fases dendrítiques, la qual cosa hem abordat mitjançant el model introduit per Almgren i col·laboradors. Hem pogut comprobar, experimentalment, la validesa i consistència d'una relació dinàmica entre

la forma i el ritme de creixement d'una branca dendrítica. De la relació d'escala en forma de llei de potències, el prefactor es mostra com una eina útil per relacionar, quantitativament, l'anisotropia present a petites escales amb les estructures dendrítiques observables a escales molt més grans. Tot i la consitència de les nostres anàlisis, no hem trobat una forma clara de caracteritzar, quantitativament, una morfologia determinada, o d'observar quantitativament la desaparició dels efectes de l'anisotropia a mida que en disminuïm la intensitat.

III Fractura en matèria condensada tova

L'ús de fluids no-newtonians en experiments de formació d'estructures genera una àmplia varietat de morfologies que no es troben en el cas de flux de fluids newtonians. En particular, les propietats reològiques d'alguns materials duen a un règim dinàmic on podem observar com el fluid es comporta d'una forma ben similar a com ho fa un sòlid fràgil. Hem estudiat el comportament d'aquests fluids mitjançant experiments de creixement viscós en un canal de Hele-Shaw, on les escales de temps típiques (de l'ordre de dècimes de segon) presenten unes condicions experimentals més simples que en l'estudi de fractura en sòlids.

En un estudi previ de creixement d'estructures de dits viscosos en cel·les de Hele-Shaw radials [38], es van utilitzar dissolucions de polímers associatius, la qual cosa va conduir a l'observació de transicions entre creixement viscós i l'aparició de quasi-fractura. El nom quasi-fractura ve donat tant per la morfologia com per la dinàmica de les estructures. S'observen branques que creixen a velocitats elevades, amb un cap estable, i desenvolupant branques laterals que creixen darrera del cap principal que avança. Aquestes branques laterals creixen formant angles pròxims a 90° amb la branca principal, un comportament típic de fractura en medis fràgils.

El fet que el creixement radial és mancat d'un estat estacionari, ens ha suggerit realitzar experiments amb els mateixos materials en geometria rectangular. En el cas d'un canal de Hele-Shaw, l'ús de fluids newtonians genera un estat estacionari força simple: un dit viscós, avançant amb velocitat constant. Estudiant les desviacions d'aquest comportament, podem observar l'aportació dels fluids no-newtonians al sistema.

Els materials que hem utilitzat com a fluids viscosos han estat solucions aquoses de polímers associatius. El model per aquests polímers consisteix en una base estructural lineal hidròfila, basada en òxid de polietilé, amb grups hidrofòbics situats, bé als extrems de la base (cas lineal) o bé situats a intèrvals regulars en la base (cas de polímers en forma de pinta). En solució aquosa, els grups hidrofòbics de diferents molècules tendeixen a associar-se, format una xarxa. Aquestes disolucions són clarament uns fluids no-newtonians. Particularment, les mesures de viscositat demostren que aquesta depèn del ritme de cisalla aplicat. A ritmes lents, el fluid es comporta com a newtonià, amb una viscositat, però, molt més elevada que en homopolímers de

pes molecular similar. A partir d'un ritme de cisalla $\dot{\gamma}_0$, que depèn de l'arquitectura del polímer i de la seva concentració, la viscositat entra en un règim decreixent.

III.A Procediment experimental i resultats qualitatius

El sistema estudiat consisteix en una cel·la de Hele-Shaw rectangular, formada per dues plaques de vidre rectangulars, col·locades paral·leles, formant un canal de 22 cm x 1.0 cm. Les dues plaques tenen un espai o gap entre elles. L'espai del gap s'omple amb la solució polimèrica, i el creixement es düu a terme injectant aigua colorejada amb un ritme d'injecció constant i control·lat, Q. Les estructures que creixen són enregistrades i analitzades digitalment. En una de les sèries d'experiments, hem mesurat i enregistrat també l'evolució de la pressió del líquid invasor en la zona d'injecció.

En tots els casos, si la injecció és prou lenta, obtenim un estat estacionari consistent en un dit de Saffman-Taylor (de fet, hem comprobat que la forma d'aquest dit satisfà la relació (7)). En la Figura 5 podem veure un exemple de les tres situacions típiques amb les quals ens trobem [40].

La sèrie superior és un exemple típic d'experiments amb els dos pesos moleculars més petits dels polímers associatius linials, amb $Q > Q_{th}$, on Q_{th} és el valor llindar pel ritme d'injecció, més enllà del qual observem l'aparició d'estructures de quasi-fractura. Observem com, en temps curts, es forma una estructura estacionària en forma de dit de Saffman-Taylor (a). El cap d'aquest dit, però esdevé inestable i la dinàmica de creixement canvia abruptament (més de pressa que 1/30 s), amb un sobtat increment en la velocitat seguit d'un increment més suau i continuat. La morfologia de l'estructura canvia també, amb una secció transversal molt més reduida que abans (a2). En el segon cas, presentem un exemple típic de flux en el pes molecular més gran de polímer associatiu linial, amb $Q > Q_{th}$. També tenim un estat estacionari a temps curts, en forma de dit de Saffman-Taylor (b1). Aquest estat, però, és inestable, i es tranforma en un altre amb una morfologia ramificada (b2), amb una velocitat d'avanç que oscil·la amb una freqüència característica (vegeu més endavant). La morfologia ramificada desemboca en un estat sense ramificacions i amb un increment continuat de la velocitat (b3). El tercer exemple, en la part inferior de la figura, correspon a flux amb polímers en forma de pinta del pes molecular més petit

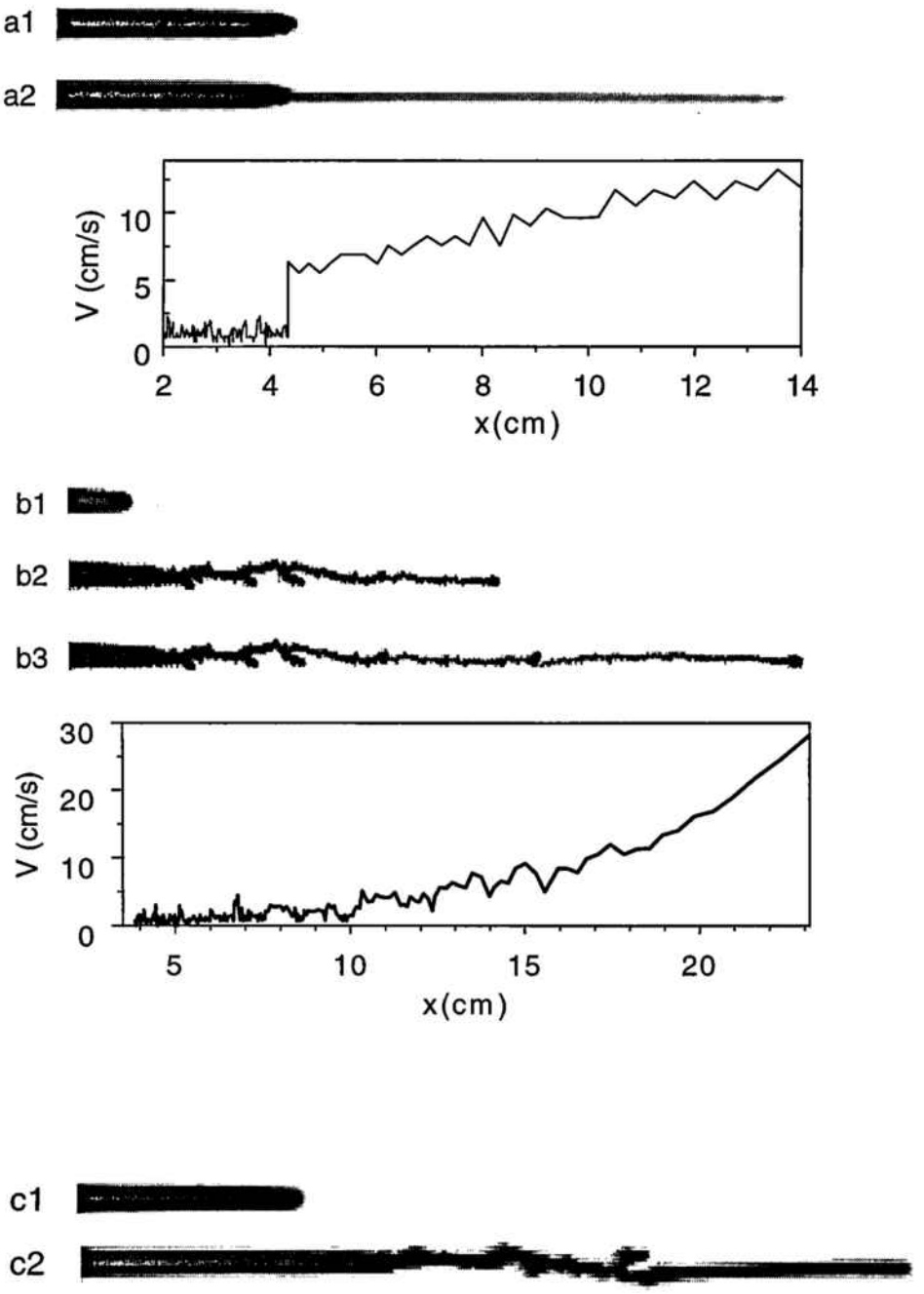

Figura 5: Diferents morfologies en el flux en polímers associatius. Sèrie superior: flux en els polímers linials de pes molecular més petit; sèrie mitja: flux en els polímers linials de pes molecular més gran; sèrie inferior: flux en els polímers en forma de pinta de pes molecular més petit.

i que mostra una evolució dinàmica amb semblances amb els dos exemples anteriors.

III.B Inestabilitat de quasi-fractura del règim viscós

Tal i com hem descrit en la secció anterior, observem com el règim de dits viscosos pot esdevenir inestable mitjançant la injecció més enllà d'un llindar Q_{th}. L'estructura que s'origina té fortes ressemblances amb la fractura en materials fràgils. Un primer intent d'explicar aquest fenomen implica la introducció d'una escala de temps intrínseca dels líquids polimèrics. Quan injectem aigua en el fluid a ritme lent, l'energia introduida externament és eficientment dissipada pel flux viscós. Nogensmenys, a ritmes d'injecció més elevats, la dissipació viscosa no és suficient i un altre mecanisme sembla ser més favorable: la fractura de medi. Per tal de caracteritzar aquesta transició, definim un número adimensional, el número de Débora, *De* [63], de forma anàloga a experiments anteriors [38].

Dels experiments en canals de HS podem extreure, com a temps característic, l'invers del ritme de cisalla:

$$\tau_f \sim \frac{Wb^2}{Q}, \tag{20}$$

on, si la velocitat característica és $U = Q/bW$, aleshores el ritme de cisalla és $\dot{\gamma} = (dU)/(dt) \sim U/b$. També definim un temps característic de la disolució polimèrica com

$$\tau_r \sim \frac{1}{\dot{\gamma}_0}. \tag{21}$$

Aleshores, obtenim un número de Débora

$$De = \frac{\tau_r}{\tau_f} = \frac{Q}{\dot{\gamma}_0 W b^2}. \tag{22}$$

L'ús del número de Débora permet rescalar el valor del llindar de transició, Q_{th}, incloent canvis en la geometria de la cel·la o en les propietats reològiques del material. Hem observat com aquesta senzilla descripció permet rescalar, satisfactòriament, els canvis en la geometria de la cel·la i els canvis en propietats reològiques derivats de canvis en la concentració de polímer en disolució. No pot, però, rescalar els canvis reològics derivats de canvis en el pes molecular o en l'arquitectura dels polímers. Hem experimentat també l'ús d'una escala de temps alternativa, la derivada de la freqüència d'excitació per la qual els mòduls elàstics del material tenen la mateixa

magnitut, però l'ús de $\dot{\gamma}_0$ dóna els millors resultats.

En el cas dels polímers en forma de pinta, l'ús del número de Débora no permet rescalar satisfactoriament ni tan sols canvis en la concentracio de polímer. Observem, però, que els valors mesurats per Q_{th} segueixen una evolució respecte la concentració que pot ser ben aproximada per una llei de potències, comportament típic dels paràmetres reològics d'aquests materials.

Un model per descriure la dinàmica de la xarxa associativa ha estat proposat per de Gennes [70]. En aquest model, el temps de relaxació dels enllaços associatius depén de l'esforç aplicat amb una relació del tipus

$$\tau = \tau_1 \exp\left(-\frac{\sigma^2}{\sigma_1^2}\right), \qquad (23)$$

on τ_1 i σ_1 són un temps i un esforç característics de la xarxa. De Gennes suggereix, a partir d'aquí, obtenir $\dot{\gamma}_0 = \mu_1/\sigma_1$. Si bé aquest model permet acomodar una fenomenologia més complexa, és precís el coneixement dels esforços en el medi.

III.C Dinàmica després de la inestabilitat del règim de dit viscós

Tal i com hem descrit en les seccions precedents, hem observat un règim dinàmic interessant que apareix després de la inestabilitat d'un dit de Saffman-Taylor. En alguns casos, la dinàmica d'aquest règim presenta una evolució no monotònica de la velocitat, amb oscil·lacions que suggereixen la comparació amb fractura de materials fràgils [54, 55] i amb experiments de desenganxament d'una cinta adhesiva [64], on *stick-slip* juga un paper primordial. Anàlogament amb com s'ha fet en aquests treballs citats, hem mesurat i analitzat l'evolució de la velocitat del cap de l'estructura que creix, per tal de trobar els trets principals de la dinàmica.

En els nostres experiments, hem procedit enregistrant l'evolució d'una estructura determinada, amb un ritme d'injecció fixat per un mecanisme d'injecció precís, i analitzant digitalment les imatges, per tal d'obtenir l'evolució de la posició del cap de l'estructura, de la seva àrea i, en una de les sèries d'experiments, de l'evolució de la pressió d'injecció. L'ús d'una càmera amb un temps d'exposició de 1/1000 s

(controlable electrònicament) ha permés unes imatges perfectament nítides. Per tal d'extreure una freqüència característica en l'evolució del règim oscil·latori hem procedit a calcular l'espectre de freqüències corresponent. En l'anàlisi de Fourier hem utilitzat un filtre numèric (*hanning window*) que elimina l'efecte del component no oscil·lant en la velocitat.

Tal i com es pot observar en la Figura 5, hi ha règims dinàmics qualitativament diferents. L'estudi que segueix analitza aquestes diferències.

En el cas corresponent a l'experiment mostrat en la Figura 5.a, l'evolució de la velocitat en el régim de dit viscós no té cap tret significatiu, fora d'una velocitat d'avanç constant (amb soroll experimental que no conté cap freqüència característica). En el moment de la inestabilitat d'aquest règim, hi ha un canvi sobtat en la magnitut de la velocitat, seguit per un increment moderat i continuat on, un cop més, no trobem cap comportament periòdic. El segon tipus d'experiments, corresponents a l'exemple mostrat en la Figura 5.b, es donen en fluxos en disolucions de polímers associatius linials del pes molecular més elevat. L'evolució temporal i l'espectre de freqüències es poden observar en la Figura 6. Observem clarament (sobretot en la gràfica insertada en la Figura 6.a que és l'evolució temporal a la qual s'ha aplicat un filtre passa-baixos) l'aparició d'un règim oscil·latori, que s'inicia un cop el règim de dit viscós es fa inestable. En aquest règim podem mesurar una freqüència característica f_1 (Figura 6.b), de forma reproduïble i que depèn de les propietats reològiques del material, del ritme d'injecció i de la geometria del canal. Podem observar en la Figura 7 com f_1 mostra una dependència aproximadament linial amb el número de Débora [o amb el ritme d'injecció, atès que hem construit $De = Q/(Wb^2\dot{\gamma}_0)$]. Podem veure com aquesta definició del número de Débora pot rescalar dos experiments amb la mateixa concentració de polímer (5%) però dimensions del canal diferents. No és capaç, però, de rescalar els canvis en concentració, indicant que aquest simple rescalat no és suficient per descriure la dinàmica. L'ús del número de Débora alternatiu, $De' = Q/(Wb^2\omega_T)$, dóna un resultat similar, peró el descartem en favor del primer per tal com aquell funciona molt millor en la predicció del llindar de inestabilitat del règim viscós.

Kurtze i Hong [71] han estudiat analíticament el comportament de quasi-fractura en matèria condensada tova i han predit l'aparició d'una freqüència d'oscil·lació basant-se en la suposició que el sistema és dominat per dinàmica de *stick-slip*. Pos-

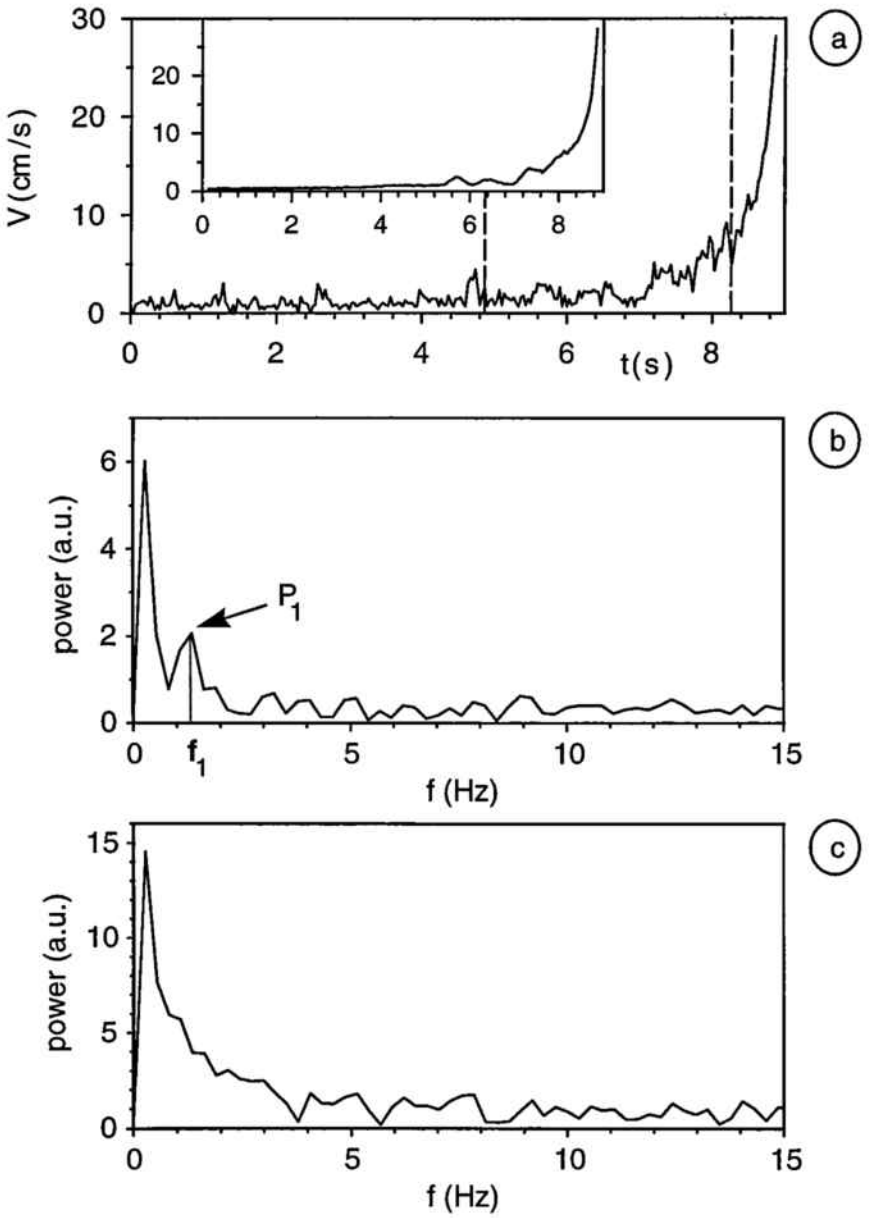

Figura 6: Evolució temporal i expectre de freqüències del perfil de velocitats en fluxes amb polímers associatius linials del pes molecular més elevat: (a) Evolució de la velocitat d'avanç, amb l'inici del règim oscil·latori i del règim de fractura ràpida marcats. (b) Espectre de freqüències del règim oscil·latori, obtingut amb un filtre *hanning window*. El pic pronunciat en els primers tres canals de freqüència és un artefacte numèric. (c) Les particularitats interessants de l'espectre de freqüències no són visibles sense el filtre numèric.

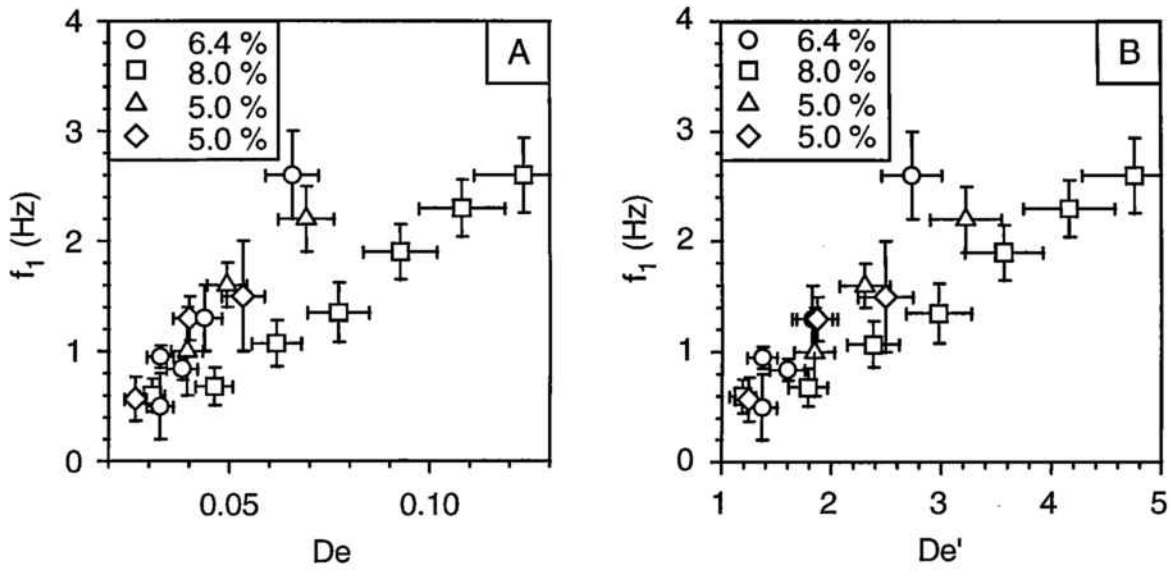

Figura 7: Dependència de la freqüència característica d'oscil·lació amb el número de Débora, mostrant un increment aproximadament linial de f_1 respecte de la força aplicada. En (B) hem considerat l'ús d'un número de Débora alternatiu, tal i com es discuteix en el text.

tulant la presència d'una relació esforços-velocitat d'avanç peculiar han demostrat l'aparició d'una bifurcació de Hopf amb una freqüència característica que es pot extreure del coneixement dels esforços viscosos dins del sistema. Hem desenvolupat a ordre més baix la seva expressió i hem arribat a l'aproximació:

$$f \sim \frac{128}{729}\frac{1}{\alpha^3}\sigma_{min}^4\frac{Q}{\mu\dot{\gamma}_0}, \tag{24}$$

on σ_{min} és l'esforç mínim en el cicle de *stick-slip* del model de Kurze i Hong; α és la tensió superficial i μ es el límit de la viscositat pel ritme de cisalla tendint a zero. En els nostres experiments, hem observat com $f \sim Q$ (vegeu Figura 7), per la qual cosa podem extreure un pendent de l'aproximació linial de les nostres dades experimentals. El resultat es pot veure en la Figura 8, on l'eix d'ordenades hauria de correspondre, segons (24) a

$$\frac{\sigma_{min}^4}{\alpha^3\mu\dot{\gamma}_0}. \tag{25}$$

Qualsevol intent de comparar els nostres resultats experimentals amb aquesta predicció teòrica passa per un coneixement adequat dels esforços viscoelàstics en el medi.

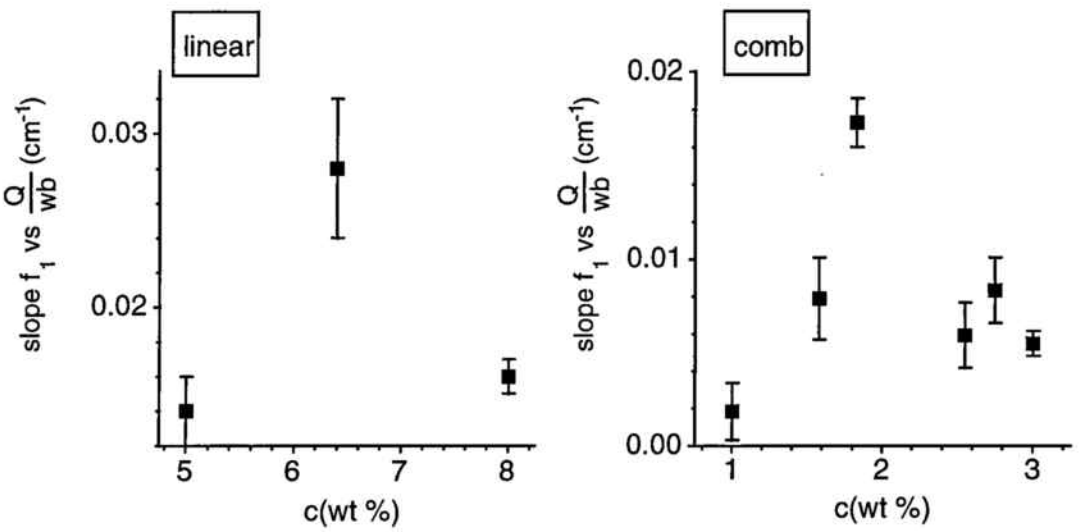

Figura 8: Efecte de la concentració de polímer en el pendent de l'increment de la freqüència oscil·latòria amb el ritme d'injecció. Les ordenades haurien de correspondre a $\sigma^4_{min}/\alpha^3\mu\dot{\gamma}_0$, segons s'explica en el text.

III.D Esforços en les estructures de quasi-fractura

Hem vist com la nostra descripció simple de la inestabilitat de quasi-fractura del règim de dits viscosos i de la freqüència característica en aquest nou règim, basada en el número de Débora (el qual construïm amb un únic paràmetre característic, $\dot{\gamma}_0$) no és suficient per descriure el que observem quan canviem de forma important les propietats reològiques dels nostres materials. També hem vist que models que intenten millorar la nostra comprensió tant de la trasició de quasi-fractura com del règim oscil·latori observat necessiten de bones mesures o estimacions dels esforços en el sistema.

Tot i que no tenim cap mètode directe per mesurar els esforços viscoelàstics en el sistema, hem intentat estimar algun valor característic a través de la mesura de la pressió del fluid invasor en el punt d'injecció. Per fer-ho, hem utilitzat expressions que ens permeten obtenir informació sobre la reologia del material que han estat derivades per fluids newtonians, peró que utilitzem com a primera aproximació en el nostre estudi de fluids no-newtonians. En primer lloc, hem obtingut una viscositat característica del règim oscil·latori, la qual hem representat en funció de la concentració en la Figura 9. Tot i que el valor absolut d'aquesta viscositat és quelcom més baix que les mesures de reologia típiques, el seu canvi sistemàtic amb la concentració de la mostra suggereix que pot ser una magnitut força significativa.

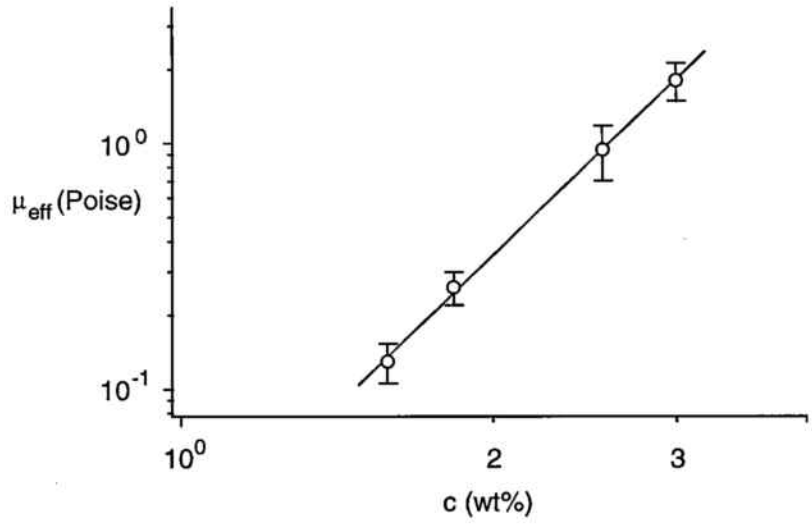

Figura 9: Viscositat efectiva extreta del valor promig de P en el règim oscil·latori. La línia és un ajust en llei de potències, el qual dóna $\mu_{eff} \sim c^{4.1}$.

D'altra banda, tenim els resultats presentats en la Figura 10, on la relació reològica viscositat/ritme de cisalla ha estat estimada experimentalment a partir de les mesures fetes en un experiment de quasi fractura. En aquest cas, si bé el comportament qualitatiu és prou similar al mesurat en reologia, els valors absoluts tant de la viscositat com de $\dot{\gamma}_0$ són lleugerament inferiors als mesurats en reologia.

IV Conclusions

Hem descrit una sèrie d'experiments, basats en la formació d'estructures durant la invasió d'un fluid poc viscós dins d'un fluid molt més viscós, en cel·les de Hele-Shaw. El sistema és prou senzill i estudiat com per permetre afegir modificacions que donen resultats nous força interessants. En un primer grup d'experiments, hem afegit externament anisotropia en el flux de fluids newtonians mitjançant un gravat d'escletxes regular. Aquesta pertorbació permet l'observació de fases dendrítiques les quals hem estudiat quantitativament mitjançant uns resultats teòrics recents. Els nostres estudis han permés elaborar uns criteris per estudiar quantitativament els efectes de l'anisotropia en les fases dendrítiques, basats en la regularitat observada en paràmetres ajustables a l'evolució del sistema. Si bé no hem trobat una forma clara de caracteritzar la morfologia d'una fase determinada, aquest mètode pot servir d'eina en el futur a l'hora d'estudiar com els efectes anisotròpics desapareixen a mida

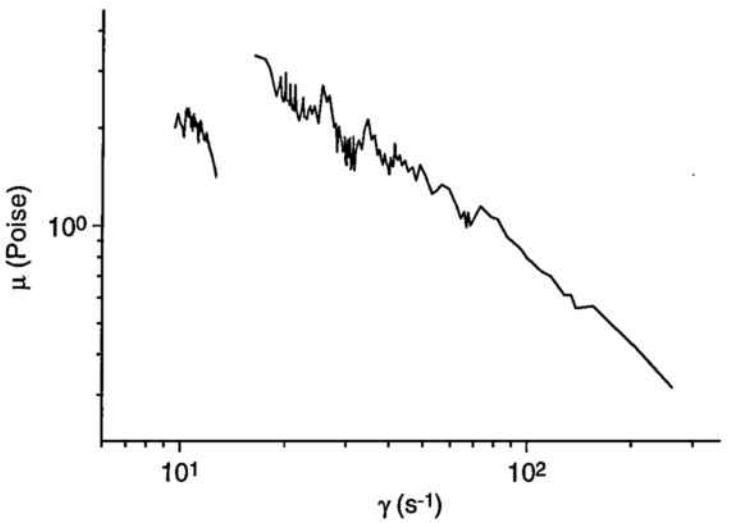

Figura 10: Viscositat efectiva promitjada sobre diverses realitzacions de flux en una disolució amb $c = 1.58\%$ de polímer associatiu en forma de pinta del pes molecular més petit. μ ha estat estimada mitjançant la llei de Darcy.

que introduïm soroll de major intensitat en el sistema.

En un segon grup d'experiments, hem estudiat l'ús de fluids polimèrics amb els quals observem una transició cap a un règim amb propietats morfològiques i dinàmiques similars a la fractura en sòlids fràgils. Hem estudiat el llidar de la transició i les freqüències característiques que apareixen, i els hem relacionat amb paràmetres característics del material. Hem vist com la simple comparació de dues escales de temps, una imposada per les pertorbacions externes, l'altra pròpia del material, permet entendre parcialment l'origen de la transició. Nogensmenys, el nostres intents per fer un estudi que inclogui una àmplia varietat de condicions reològiques passen per l'obtenció de mesures addients dels esforços viscoelàstics en el medi.

BIBLIOGRAPHY

[1] D. Bensimon, L. P. Kadanoff, S. Liang, B. I. Shraiman, and C. Tang, Rev. Mod. Phys. **58**, 977 (1986).

[2] G. M. Homsy, Ann.Rev.Fluid Mech. **19**, 271 (1987).

[3] P. Pelce, Academic Press,Boston -, (1988).

[4] D. A. Kessler, J. Koplik, and H. Levine, Adv. Phys. **37**, 255 (1988).

[5] A. A. Sonin, Riv. Nouvo Cim. **14**, 1 (1991).

[6] K. V. McCloud and J. Maher, Phys. Rep. **260**, 139 (1995).

[7] R. L. Chuoke, P. van Meurs, and C. van der Poel, Trans. AIME **216**, 189 (1959).

[8] J. V. Maher, Phys. Rev. Lett. **54**, 1498 (1985).

[9] C. W. Park and G. M. Homsy, J. Fluid. Mech. **139**, 291 (1984).

[10] L. Paterson, J. Fluid Mech. **113**, 513 (1981).

[11] C. Yeung and D. Jasnow, Phys. Rev. A **41**, 891 (1990).

[12] S. N. Rauseo, P. D. Barnes Jr., and J. V. Maher, Phys. Rev. A **35**, 1245 (1987).

[13] J. D. Chen, Exp. in Fluids **5**, 363 (1987).

[14] P. G. Saffman and G. Taylor, Proc. R. Soc. London A **245**, 312 (1958).

[15] J. Pitts, J. Fluid Mech. **97**, 53 (1980).

[16] J. W. McLean and P. G. Saffman, J. Fluid Mech. **102**, 455 (1981).

[17] P. Tabeling and A. Libchaber, Phys.Rev.A **33**, 794 (1986).

[18] H. Thome, M. Rabaud, V. Hakim, and Y. Couder, Phys. Fluids A **1**, 224 (1989).

[19] S. Sarkar and D. Jasnow, Phys. Rev. A **35**, 4900 (1987).

[20] E. Ben-Jacob, N. Goldenfeld, J. S. Langer, and G. Schon, Phys. Rev. Lett. **51**, 1930 (1983).

[21] E. Ben-Jacob et al., Phys. Rev. Lett. **55**, 1315 (1985).

[22] Y. Couder, O. Cardoso, D. Dupuy, P. Tavernier, and W. Thom, Europhys. Lett. **2**, 437 (1986).

[23] Y. Couder, N. Gerard, and M. Rabaud, Phys. Rev. A **34**, 5175 (1986).

[24] A. Buka and P. Palffy-Muhoray, Phys. Rev. A **36**, 1527 (1987).

[25] L. Lam et al., Liquid Crystals **5**, 1813 (1989).

[26] M. Matsushita and H. Yamada, J. Crystal Growth **99**, 161 (1990).

[27] V. Horvath, T. Vicsek, and J. Kertesz, Phys. Rev. A **35**, 2353 (1987).

[28] J. Nittman, G. Daccord, and H. E. Stanley, Nature **314**, 141 (1985).

[29] G. Daccord, J. Nittman, and H. E. Stanley, Phys. Rev. Lett. **56**, 336 (1986).

[30] H. Van Damme, F. Obrecht, P. Levitz, L. Gatineau, and C. Laroche, Nature **320**, 731 (1986).

[31] H. Van Damme, C. Laroche, and L. Gatineau, Revue Phys. Appl. **22**, 241 (1987).

[32] H. Van Damme, C. Laroche, L. Gatineau, and P. Levitz, J. Physique **48**, 1121 (1987).

[33] H. Van Damme, E. Alsac, C. Laroche, and L. Gatineau, Europhys. Lett. **5**, 25 (1988).

[34] P. G. de Gennes, Europhys. Lett. **3**, 195 (1987).

[35] H. Zhao and J. V. Maher, Phys. Rev. A **45**, 8328 (1992).

[36] K. Makino, K. Masami, K. Aoyama, and T. Kato, Phys. Fluids **7(3)**, 455 (1995).

[37] E. Lemaire, P. Levitz, G. Daccord, and H. Van Damme, Phys. Rev. Lett. **67**, 2009 (1991).

[38] H. Zhao and J. V. Maher, Phys. Rev. E **47**, 4278 (1993).

[39] J. Ignés-Mullol and J. V. Maher, Phys. Rev. E **53**, 3788 (1996).

[40] J. Ignés-Mullol, H. Zhao, and J. V. Maher, Phys. Rev. E **51**, 1338 (1995).

[41] Dage-MTI, Michigan City, IN, *CCD-72 video camera.*

[42] All Tronics Medical Systems, *HRV-3000E Enhanced Super VHS Recorder.*

[43] BioScan Inc,Edmons, WA, OPTIMAS *v. 3.01.*

[44] Autodesk, AUTOCAD, *release 12.*

[45] E. Ben-Jacob and P. Garik, Nature **343**, 523 (1990).

[46] E. Ben-Jacob, P. Garik, T. Mueller, and D. Grier, Phys. Rev. A **38**, 1370 (1988).

[47] S. K. Sarkar and D. Jasnow, Phys. Rev. A **39**, 5299 (1989).

[48] R. Almgren, private communication.

[49] R. Almgren, W.-S. Dai, and V. Hakim, Phys. Rev. Lett. **71**, 3461 (1993).

[50] M. Ben Amar, Phys. Rev. A **44**, 3673 (1991).

[51] A. Karma, private communication.

[52] M. Ben Amar and Y. Pomeau, Europhys. Lett. **2**, 307 (1986).

[53] J. Ortín and J. Ignés-Mullol, unpublished data.

[54] J. Fineberg, S. P. Gross, M. Marder, and H. L. Swinney, Phys. Rev. Lett. **67**, 457 (1991).

[55] J. Fineberg, S. P. Gross, M. Marder, and H. L. Swinney, Phys. Rev. B **45**, 5146 (1992).

[56] R. D. Jenkins, *The Fundamental Thickening Mechanism of Associative Polymers in Latex Systems: A Rheological Study*, PhD thesis, 1990.

[57] R. D. Jenkins, C. A. Silebi, and M. S. El-Aasser, Am. Chem. Soc. Symposium Series **462**, 223 (1991).

[58] ORION Research Incorporated, Boston, MA, *Sage Model 355 Syringe pump.*

[59] NEC Co., *TI-324A CCD camera.*

[60] OMEGA Technologies, Stanford, CT, *PX26 pressure transducer.*

[61] R. D. Jenkins, unpublished data.

[62] P. Tabeling, G. Zocchi, and A. Libchaber, J. Fluid Mech. **177**, 67 (1987).

[63] R. I. Reiner, Physics Today **62**, (1964).

[64] D. Maugis and M. Barquins, 'Adhesion 12', edited by K. W. Allen (Elsevier Applied Science) **1**, 205 (1987).

[65] BCD Associates, Inc., Oklahoma City, OK, *BCD-5000 Video Controller.*

[66] E. O. Brigham, *The Fast Fourier Transform*, Prentice Hall Inc., Englewood Cliffs, NJ, 1st edition, 1974.

[67] R. C. Ball and R. Blumenfeld, Phys. Rev. Lett. **65**, 1784 (1990).

[68] Y. Hayakawa, Phys. Rev. E **49**, 1804 (1994).

[69] A. Yuse and M. Sano, Nature **362**, 329 (1993).

[70] P. G. de Gennes, private communication.

[71] D. Kurtze and D. C. Hong, Phys. Rev. Lett. **71**, 847 (1993).

[72] M. A. Rubio and J. Galeano, Phys. Rev. E **50**, 1000 (1994).

[73] K. R. Rajagopal, *Mechanics of mixtures*, appendix B, World Scientific, Singapore, 1995.

[74] D. Bonn, H. Kellay, M. Braunlich, M. Ben Amar, and J. Meunier, Physica A **220**, 60 (1995).

[75] Brookfield Engineering Laboratories, Inc., Stroughton, MA, *Model DV-III Programable Rheometer.*

[76] L. Landau and E. Lifshitz, *Fluid Dynamics*, Pergamon Press, New York, 2nd edition, 1987.

[77] P.-G. de Gennes, C. R. Acad. Sci. Paris **t. 307,Serie II**, 1949 (1988).

[78] L. Landau and E. Lifshitz, *Theory of elasticity*, Pergamon Press, New York, 3rd edition, 1986.